First Determination of the Proton Electric Form Factor at Very Small Momentum Transfer Using Initial State Radiation

Dissertation
zur Erlangung des Grades
„Doktor
der Naturwissenschaften“
am Fachbereich Physik, Mathematik und Informatik
der Johannes Gutenberg-Universität
in Mainz

Adrian Bartholomäus Weber
geb. in Königstein im Taunus

Mainz, den 20. Dezember 2016

Erster Berichterstatter:
Zweiter Berichterstatter:

Datum der mündlichen Prüfung: 2. Mai 2017

ABSTRACT

The charge radius is a fundamental parameter of the proton and being investigated for more than 60 years [1]. When in 2010 results of the spectroscopy of muonic hydrogen were published, the proton radius puzzle arose [2]. These results differ for about 6 standard deviations from the CODATA value, determined from elastic electron-proton scattering experiments and hydrogen spectroscopy [3, 4]. To understand this discrepancy more precise measurements are necessary. For this purpose measurements of the proton electric form factor at $Q^2 < 4 \cdot 10^{-3}\,(\mathrm{GeV/c})^2$ are essential. Unfortunately, this cannot be done by measuring elastic electron-proton scattering processes at the existing experimental facilities. To reach the form factor at even lower values of Q^2 a method based on initial state radiation (ISR) was developed and realised. By measuring the scattered electrons in the radiative tail at the Mainz Microtron (MAMI), information about the electric form factor as low as $Q^2 \approx 1 \cdot 10^{-4}\,(\mathrm{GeV/c})^2$ can be obtained.

The experiment was performed at MAMI in the A1 spectrometer hall using two high resolution spectrometers. One was employed to measure the scattered electrons and the other one as a relative luminosity monitor. To minimise systematic uncertainties only the momentum acceptance of the spectrometer recording the electrons in the radiative tail was changed during the experiment. All other parameters were kept untouched. To compare the results of the ISR experiment with former results of the electric form factor, the measurements were performed at three different beam energies .

During the analysis the data were compared with a simulation. The simulation exactly calculated the Bethe-Heitler and Born Feynman diagrams and used effective corrections to consider also higher order Feynman diagrams. When applying the form factor of Bernauer et al. [5], the simulation matched the new data within 1%. This justified the usage of the ISR method.

Finally, under the assumption that the scattering processes were described perfectly by the simulation, the form factor was adjusted to the new data. As a result the form factor was determined as low as $Q^2 = 1.3 \cdot 10^{-3}\,(\mathrm{GeV/c})^2$. With these results the following value of the charge radius of the proton was determined:

$$r_E = \left(0.810 \pm 0.035_{\mathrm{stat.}} \pm 0.074_{\mathrm{syst.}} \pm 0.003_{\mathrm{mod.}}\right)\ \mathrm{fm}\,.$$

This result has large uncertainties and cannot distinguish between the CODATA value [3] and the result of the spectroscopy of muonic hydrogen [2]. In a succeeding experiment the ISR method will be used to determine the form factor with smaller uncertainties as low as $Q^2 \approx 1 \cdot 10^{-4}\,(\mathrm{GeV/c})^2$ [6].

ZUSAMMENFASSUNG

Der Ladungsradius ist eine fundamentale Größe des Protons und wird seit über 60 Jahren untersucht [1]. Als 2010 Ergebnisse der Spektroskopie von myonischem Wasserstoff veröffentlicht wurden, führte dies auf das Protonradiuspuzzle [2]. Die Ergebnisse weichen um ca. 6 Standardabweichungen von dem CODATA Wert ab, welcher mit elastischer Streuung von Elektronen an Protonen und der Spektroskopie von Wasserstoff bestimmt wurde [3, 4]. Um den Unterschied zu verstehen, sind präzisere Messungen notwendig. Dazu sind Messungen des elektrischen Formfaktors des Protons mit $Q^2 < 4 \cdot 10^{-3}\,(\mathrm{GeV}/c)^2$ unerlässlich. Mit elastischer Elektronenstreuung an Protonen kann dies mit den vorhandenen Experimentieranlagen leider nicht erreicht werden. Um noch kleinere Werte von Q^2 zu erreichen, wurde eine Messmethode auf Grundlage der Abstrahlung eines Photons im Anfangszustand entwickelt und realisiert. Am Mainzer Mikrotron (MAMI) können durch die Messung der gestreuten Elektronen im Strahlenschwanz Informationen über den elektrischen Formfaktor bis zu $Q^2 \approx 1 \cdot 10^{-4}\,(\mathrm{GeV}/c)^2$ erhalten werden.
Das Experiment wurde an MAMI in der A1 Spektrometerhalle mit zwei hochauflösenden Spektrometern durchgeführt. Eins wurde benutzt, um die gestreuten Elektronen zu messen, das andere, um die relative Luminosität zu bestimmen. Um systematische Unsicherheiten zu minimieren, wurde lediglich die Impulsakzeptanz des Spektrometers geändert, welches die Elektronen im Strahlenschwanz detektierte. Alle anderen Parameter blieben unverändert. Um die Ergebnisse des Experiments mit früheren Resultaten des elektrischen Formfaktors vergleichen zu können, wurde die Messung bei drei verschiedenen Strahlenergien durchgeführt.
Während der Analyse wurden die Daten mit einer Simulation verglichen. Diese berechnete die Bethe-Heitler und Born Feynman-Diagramme exakt und benutzte effektive Korrekturen, um höhrere Ordnungen von Feynman-Diagrammen zu berücksichtigen. Beim Verwenden des Formfaktors von Bernauer et al. [5] in der Simulation wurde gezeigt, dass sie mit den neuen Daten innerhalb von 1% übereinstimmte. Dies rechtfertigte die Benutzung der Methode auf Grundlage der Abstrahlung eines Photons im Anfangszustand.
Unter der Annahme, dass die Streuprozesse von der Simulation einwandfrei beschrieben wurden, wurde der Formfaktor an die neuen Daten angepasst. Als Ergebnis wurde der Formfaktor bis zu $Q^2 = 1,3 \cdot 10^{-3}\,(\mathrm{GeV}/c)^2$ bestimmt. Mit diesen Ergebnissen konnte der Ladungsradius des Protons zu:

$$r_E = \left(0,810 \pm 0,035_{\mathrm{stat.}} \pm 0,074_{\mathrm{syst.}} \pm 0,003_{\mathrm{mod.}}\right)\ \mathrm{fm}$$

bestimmt werden. Dieser Wert ist mit großen Unsicherheiten behaftet und kann nicht zwischen dem CODATA [3] Wert und dem Ergebnis der Spektroskopie von myonischem Wasserstoff [2] unterscheiden. In einem Nachfolgeexperiment

soll die Methode auf Grundlage der Abstrahlung eines Photons im Anfangszustand dazu benutzt werden, um den Formfaktor mit kleineren Unsicherheiten bis zu $Q^2 \approx 1 \cdot 10^{-4}\,(\mathrm{GeV/c})^2$ zu bestimmen [6].

CONTENTS

1

MOTIVATION

The proton is a basic constiuent of matter [7]. It was identified by Wien (1898) and Thomson (1919) and named by Rutherford (1920). Its mass is $938.2796(27)\,\mathrm{MeV}/c^2$ and it has a positive charge of $1.602 \cdot 10^{-19}\mathrm{C}$ [7]. It has a spin of $\frac{1}{2}\hbar$. If the proton would be a point-like particle, its magnetic moment would be given by [8]:

$$\mu = \frac{g}{2} \cdot \frac{Ze}{M} \cdot \frac{\hbar}{2}, \tag{1}$$

where $g = 2$ is the g-factor, Ze is its charge, M is its mass and $\hbar$ is Planck's constant divided by 2π. The measurements described in Ref. [9] and [10] determined that the magnetic moment of the proton was 2.5 times bigger than expected. Later measurements determined the more precise value of $2.792847351(9)$ proton magnetons [3]. This deviation from the expected value of 1 cannot be explained, like it can be for the electron, where considering higher order corrections in quantum elctrodynamics (QED), the weak interaction and quantum chromodynamics measurements result in a value of $1.00115965213073(28)$ [11] in accordance with theory. This directly indicates that the proton has an inner structure and is not a point-like particle. As it is understood today, the proton is not an elementary particle, but actually consists of three quarks, two up quarks having $\frac{2}{3}$ times the elementary charge and one down quark having $-\frac{1}{3}$ times the elementary charge. Since it consists of three quarks it is called a baryon and has a baryon quantum number of 1 [12]. The three quarks are bound by the strong force [7]. Although it is kinematically possible that a proton decays into a pion and a positron for example [13], no such events have been observed. The proton therefore is called a stable particle and has a life time greater than $6.6 \cdot 10^{33}$ years [13].
To describe the cross section in the scattering theory, for example when an electron scatters off a proton, some modifications to a hypothetical point-like proton have to be applied, see chapter 2. For over 60 years experiments, see for example Ref. [1], [5] or [14], have been performed to study the structure of the proton. One important value which can be determined in such experiments is the charge radius of the proton. This radius is given by [8], see also chapter 2:

$$r_E{}^2 \equiv -6\hbar^2 \left.\frac{dG_E\left(Q^2\right)}{dQ^2}\right|_{Q^2=0}. \tag{2}$$

This radius can be determined by electron proton scattering experiments or atomic spectroscopy. The results of both kinds of experiments are consistent and in average yield $0.8751(61)$ fm [3]. But there is a puzzle about the charge radius of the proton, because the result of the spectroscopy of muonic hydrogen, this is a proton surrounded by a muon rather than an electron, yields a quite different result of $0.84087(39)$ fm [2]. This is a deviation of about 6 standard deviations and the reason for this is yet an open question. One answer could simply be, that the determination of the radius has not been done properly, leading to the discrepancy. It is also possible that the interactions of electrons and muons are not universal, breaking lepton universality in the Standard Model, which would indicate that new theoretical models would be needed to describe the phenomenon [4].
In this work a new method using electron proton scattering will be presented to determine the charge radius of the proton more accurately. This method enables to measure at lower values of Q^2 than before. This is very important for determining the charge radius of the proton, as can be seen from equation 2. When determining the charge radius of the proton by scattering experiments, usually just the cross section of elastically scattered electrons (elastic peak) is measured. Hence, using the available experimental facilities, there is a limit for the lowest accessible value of Q^2. To avoid these limitations the method used for this experiment did not only include the elastic peak but also electrons which radiated a photon before being detected (radiative tail), thus enabling a more accurate determination of the charge radius of the proton, see chapter 3.

2

THEORETICAL FOUNDATIONS

The basic concepts necessary for dealing with scattering experiments will be explained here. During an experiment the kinematics of the scattering process define the observables of the studied particles. For this experiment only the four-vectors of the particles are needed, see Fig. 1. In this plot two particles with initial four-vectors k_i and p_i scatter and two particles with four-vectors k_f and p_f emerge. The time evolution is always from the left side to the right side.

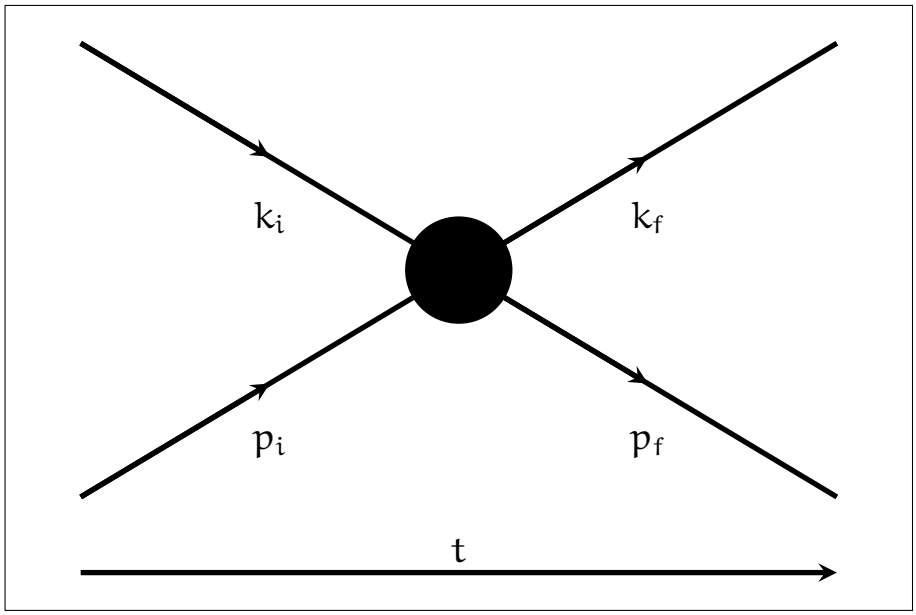

Figure 1: Kinematics for a scattering process. Two particles with four-vectors k_i and p_i scatter and after the scattering process, black blob, two particles with four-vectors k_f and p_f emerge. The time evolution is from the left side to the right side.

The probabilty that a reaction between two particles, here given for one incident particle and a particle at rest, takes place is described by the cross section σ which is given by [8]:

$$\sigma = \frac{\text{numbers of particles scattered per time unit}}{\text{incident particles per time unit} \cdot \text{target particles per area unit}} . \quad (3)$$

For convenience often the differential cross section, depending on the solid angle, is given, because many detectors only cover a fraction of the full solid angle:

$$\frac{d\sigma}{d\Omega} = \frac{\text{numbers of particles scattered in solid angle per time unit}}{\text{incident particles per time unit} \cdot \text{target particles per area unit}} . \quad (4)$$

Another important variable is the luminosity $\mathfrak{L}$:

$$\mathfrak{L} = \text{incident particles per time unit} \cdot \text{target particles per area unit} . \quad (5)$$

In an experiment the quantity which can be measured is the number of particles, N, in a certain fraction of the full solid angle in a certain amount of time. It is connected with the cross section and the luminosity by:

$$N = \int_t \mathfrak{L} \cdot \frac{d\sigma}{d\Omega} \cdot \Delta\Omega \cdot dt . \quad (6)$$

$\Delta\Omega$ is the fraction of the full solid angle covered by the detector. In this work elastic scattering of electrons off protons will be investigated. Assuming a point-like proton the cross section for such scattering processes would be given by the Mott formula [8]:

$$\left(\frac{d\sigma}{d\Omega}\right)_{\text{Mott}} = \frac{4 \cdot \left(Z\alpha\hbar c E'\right)^2}{|qc|^4} \cdot \left(1 - \beta^2 \sin^2\left(\frac{\theta}{2}\right)\right) . \quad (7)$$

Here Z is the charge number of the proton, c is the velocity of light, E' is the energy of the scattered electron, θ is the scattering angle of the electron, q is the four-vector of the virtual photon exchanged between the eletron and the proton and β is the velocity of the particle divided by c. q^2 is needed often, but as for scattering processes its value is always negative, the variable Q^2, which is $-q^2$, is used instead for convenience. For a visualisation of this process, see Fig. 2.
Before the reaction the proton is at rest. The scattering process is mediated by a virtual photon, a carrier of electromagnetic interaction in the space-like region. The electron is scattered in a random direction and in accordance with energy and momentum conservation the proton is also scattered. The angle between the incoming and outgoing electron is the scattering angle θ. The following approximation can be used to calculate E' from E and θ [8]:

$$E' = \frac{E}{1 + \frac{E}{Mc^2}(1 - \cos(\theta))} . \quad (8)$$

When measuring electrons scattering off protons, a deviation from the Mott cross section was detected, see Fig. 3. Since protons are not point-like, form factors need to be introduced to the Mott cross section to correctly describe the scattering process of an electron from a proton. These form factors describe the inner structure, the spread in space, of the proton, analogous to these used to describe the cross sections for heavy nuclei [15].

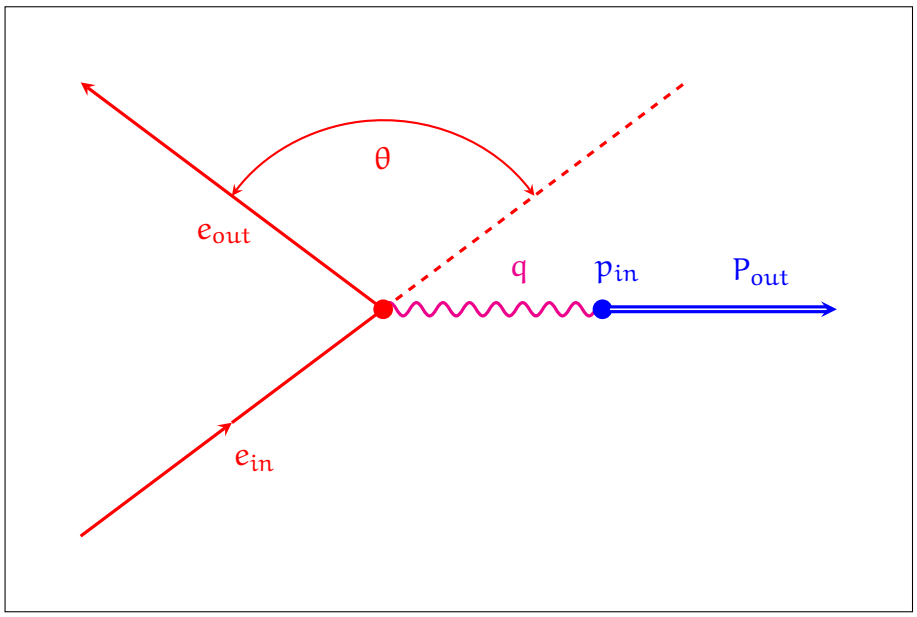

Figure 2: Kinematics for elastic scattering of an electron from a proton being at rest.

To describe scattering of a relativistic electron from a proton first the Dirac spinors, the gamma matrices and the Pauli matrices need to be introduced (here in Dirac representation) [16]:

$$u(l,\uparrow) = \sqrt{\frac{E+mc^2}{c}} \begin{pmatrix} 1 \\ 0 \\ \frac{c\cdot p_z}{E+mc^2} \\ \frac{c(p_x+ip_y)}{E+mc^2} \end{pmatrix}, \qquad u(l,\downarrow) = \sqrt{\frac{E+mc^2}{c}} \begin{pmatrix} 0 \\ 1 \\ \frac{c(p_x-ip_y)}{E+mc^2} \\ \frac{-c\cdot p_z}{E+mc^2} \end{pmatrix},$$

$$\gamma^0 = \begin{pmatrix} \mathbb{1} & 0 \\ 0 & -\mathbb{1} \end{pmatrix}, \qquad \gamma^i = \begin{pmatrix} 0 & \sigma^i \\ -\sigma^i & 0 \end{pmatrix}, \tag{9}$$

$$\sigma^1 = \begin{pmatrix} 0 & 1 \\ 1 & 0 \end{pmatrix}, \qquad \sigma^2 = \begin{pmatrix} 0 & -i \\ i & 0 \end{pmatrix}, \qquad \sigma^3 = \begin{pmatrix} 1 & 0 \\ 0 & -1 \end{pmatrix},$$

$u(l,\uparrow)$ is a spin 1/2 particle spinor with a spin of $+1/2$, $u(l,\downarrow)$ is a spin 1/2 particle spinor with a spin of $-1/2$, where the direction of the spin is with respect to the z-axis. m is the mass of the respective particle, E is its energy and p_x, p_y, p_z are its momentum components, $l = (E, p_x, p_y, p_z)$ and $\overline{u}(l) = u(l)^\dagger \gamma_0$. The dagger symbol is the conjugate transpose operator [17].
The scattering processes can be visualized with so called Feynman diagrams, see Fig. 4. The first step in determining the cross section is to calculate the transition amplitude using Feynman rules [16]:

$$\mathfrak{M} = j^\mu \frac{1}{q^2} J_\mu \,. \tag{10}$$

The current density j^μ for the point-like electron is given by [18]:

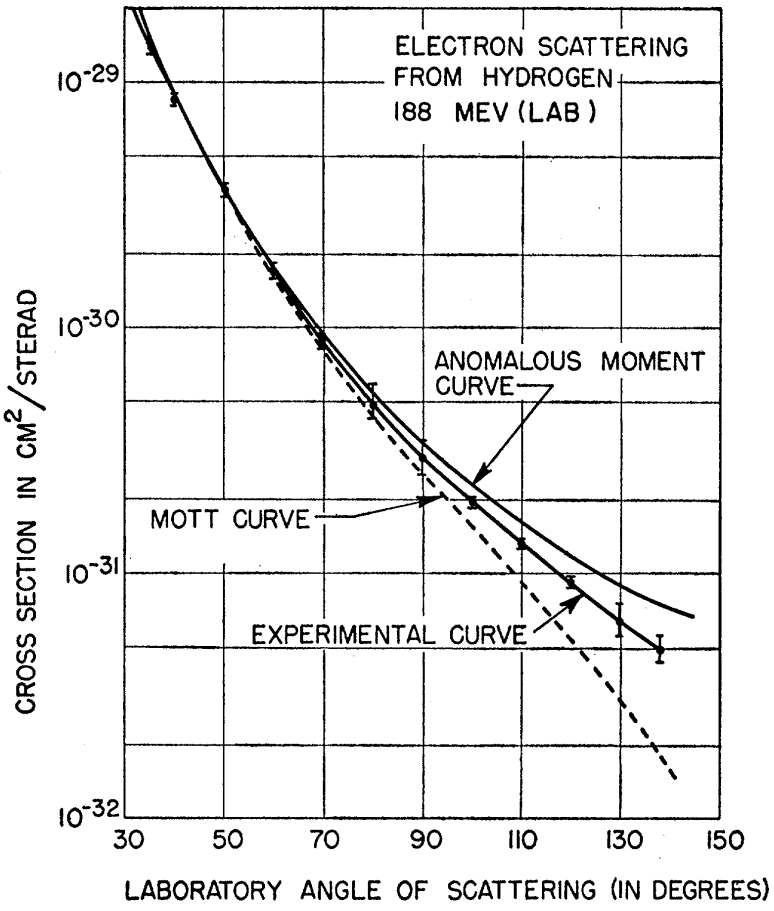

Figure 3: Cross section for elastic scattering of electrons from hydrogen. The experimental data show a distinct deviation from the Mott cross section. (source: [1])

$$j^{\mu} = -e\left(\overline{u}\left(l_{out}\right)\gamma^{\mu}u\left(l_{in}\right)\right) . \tag{11}$$

$\overline{u}\left(l_{out}\right)$ and $u\left(l_{in}\right)$ are Dirac spinors. γ^{μ} is a Dirac γ-matrix.
On the other hand, the proton is no point-like particle and needs a different four-vector current density than the Dirac one used for the electron. The most general ansatz for the proton current density is [18]:

$$J_{\mu} = e\left(\overline{u}\left(p_{out}\right)\Gamma_{\mu}\left(p_{out}, p_{in}\right)u\left(p_{in}\right)\right) = e\left(\overline{u}\left(p_{out}\right)\left(A\left(q^2\right)\gamma_{\mu} + B\left(q^2\right)\left(p_{out}\right)_{\mu}\right.\right.$$
$$\left.\left. + C\left(q^2\right)\left(p_{in}\right)_{\mu} + iD\left(q^2\right)\left(p_{out}\right)_{\mu}\sigma_{\mu\nu} + iE\left(q^2\right)\left(p_{in}\right)_{\mu}\sigma_{\mu\nu}\right)u\left(p_{in}\right)\right) ;$$

$$\sigma_{\mu\nu} = \frac{i}{2}\left(\gamma_{\mu}\gamma_{\nu} - \gamma_{\nu}\gamma_{\mu}\right) . \tag{12}$$

The new current density has of course to fulfill gauge invariance [18]:

$$q^{\mu}\overline{u}\left(p_{out}\right)\Gamma_{\mu}\left(p_{out}, p_{in}\right)u\left(p_{in}\right) = 0 . \tag{13}$$

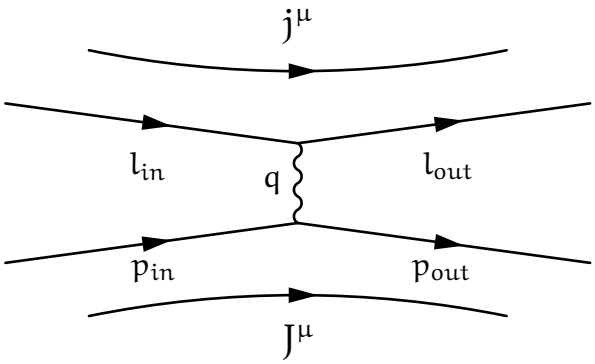

Figure 4: Feynman diagram for elastic scattering of an electron from a proton in the Born approximation. l_{in}, l_{out}, p_{in}, p_{out} and q are the four-vectors of the respective particles.

Applying this restriction and the Gordon decomposition [18], the most general expression for a transition current fulfilling the condition of Lorentz covariance, Hermiticity and gauge invariance is:

$$\begin{aligned} J_\mu &= e\left(\overline{u}\left(p_{out}\right)\left(\gamma_\mu F_1\left(q^2\right)+\frac{i}{2M}F_2\left(q^2\right)q^\nu\sigma_{\mu\nu}\right)u\left(p_{in}\right)\right), \\ \Gamma_\mu &= \gamma_\mu F_1\left(q^2\right)+\frac{i}{2M}F_2\left(q^2\right)q^\nu\sigma_{\mu\nu}. \end{aligned} \tag{14}$$

F_1 and F_2 are functions of q^2 only and are known as Dirac form factors. For this work the spin of the particles was randomly distributed, therefore only a squared spin averaged transition amplitude is necessary [16]:

$$\left\langle|\mathfrak{M}|^2\right\rangle = \frac{1}{(2s_A+1)(2s_B+1)}\sum_{\text{all spin states}}|\mathfrak{M}|^2. \tag{15}$$

Here s_A and s_B are the spins of the incoming particles. The cross section for the scattering of two spin-$\frac{1}{2}$-particles in the labatory frame, where the target particle is at rest, is [17]:

$$\left(\frac{d\sigma}{d\Omega}\right) = \left(\frac{\hbar}{8\pi Mc}\right)^2\cdot\left\langle|\mathfrak{M}|^2\right\rangle. \tag{16}$$

Here M is the mass of the target particle. Using this current density for the proton, the cross section for scattering an electron from an initially resting proton yields [16], [19], [20]:

$$\begin{aligned} \left(\frac{d\sigma}{d\Omega}\right) = &\frac{4\cdot\left(Z\alpha\hbar cE'\right)^2}{|qc|^4}\cdot\left(1-\beta^2\sin^2\left(\frac{\theta}{2}\right)\right) \\ &\cdot\left[F_1^2\left(q^2\right)+\tau\left(\kappa F_2^2\left(q^2\right)\right)+2\tau\left(F_1\left(q^2\right)+\kappa F_2\left(q^2\right)\right)^2\cdot\tan^2\left(\frac{\theta}{2}\right)\right], \end{aligned} \tag{17}$$

$$\kappa = (2.792847350(9) - 1) \cdot \mu_N = (\mu_p - 1) \cdot \frac{e\hbar}{2M} \text{ [21]},$$
$$\tau = \frac{Q^2}{4M},$$
$$Q^2 = -q^2 = 4EE' \sin^2\left(\frac{\theta}{2}\right). \tag{18}$$

κ is the anomalous magnetic moment of the proton. To give these form factors a more meaningful interpretation linear combinations of F_1 and F_2 can be used [19], [22]:

$$G_E\left(Q^2\right) = F_1\left(Q^2\right) - \tau\kappa F_2\left(Q^2\right),$$
$$G_M\left(Q^2\right) = F_1\left(Q^2\right) + \kappa F_2\left(Q^2\right). \tag{19}$$

G_E and G_M are the so called Sachs form factors. G_E measures the charge distribution of the proton and G_M the distribution of magnetization [19]. With these form factors the cross section for elastic electron-proton scattering becomes:

$$\left(\frac{d\sigma}{d\Omega}\right) = \left(\frac{d\sigma}{d\Omega}\right)_{\text{Mott}} \cdot \left(\frac{{G_E}^2\left(Q^2\right) + \tau {G_M}^2\left(Q^2\right)}{1+\tau} + 2\tau {G_M}^2\left(Q^2\right)\tan^2\left(\frac{\theta}{2}\right)\right)$$
$$= \left(\frac{d\sigma}{d\Omega}\right)_{\text{Mott}} \frac{\epsilon\, {G_E}^2\left(Q^2\right) + \tau {G_M}^2\left(Q^2\right)}{\epsilon \cdot (1+\tau)}, \tag{20}$$

$$\epsilon = \left(1 + 2\,(1+\tau)\tan^2\left(\frac{\theta}{2}\right)\right)^{-1}. \tag{21}$$

ϵ is the level of longitudinal polarization of the photon exchanged in the scattering process.

Proton radius

To extract G_E and G_M from the measurements of cross section data the Rosenbluth separation can be used. It exploits the fact, that for constant Q^2 but different values of ϵ in equation 20 the experimental cross section devided by the Mott cross section and multiplied only with kinematic variables is a linear function of ${G_E}^2$ and ${G_M}^2$ with slope ${G_E}^2/\tau$ and intercept ${G_M}^2$:

$$\left(\frac{d\sigma}{d\Omega}\right)_{\text{Exp.}} \Big/ \left(\frac{d\sigma}{d\Omega}\right)_{\text{Mott}} \frac{\epsilon\,(1+\tau)}{\tau} = \frac{\epsilon}{\tau}{G_E}^2 + {G_M}^2. \tag{22}$$

To obtain measurements at different values of Q^2 and ϵ the detectors need to be set to different angles and accepted momenta to measure the scattered electrons. But these experimental parameters have a certain uncertainty leading to a systematic uncertainty in the analysis, which is the main disadvantage of the method.

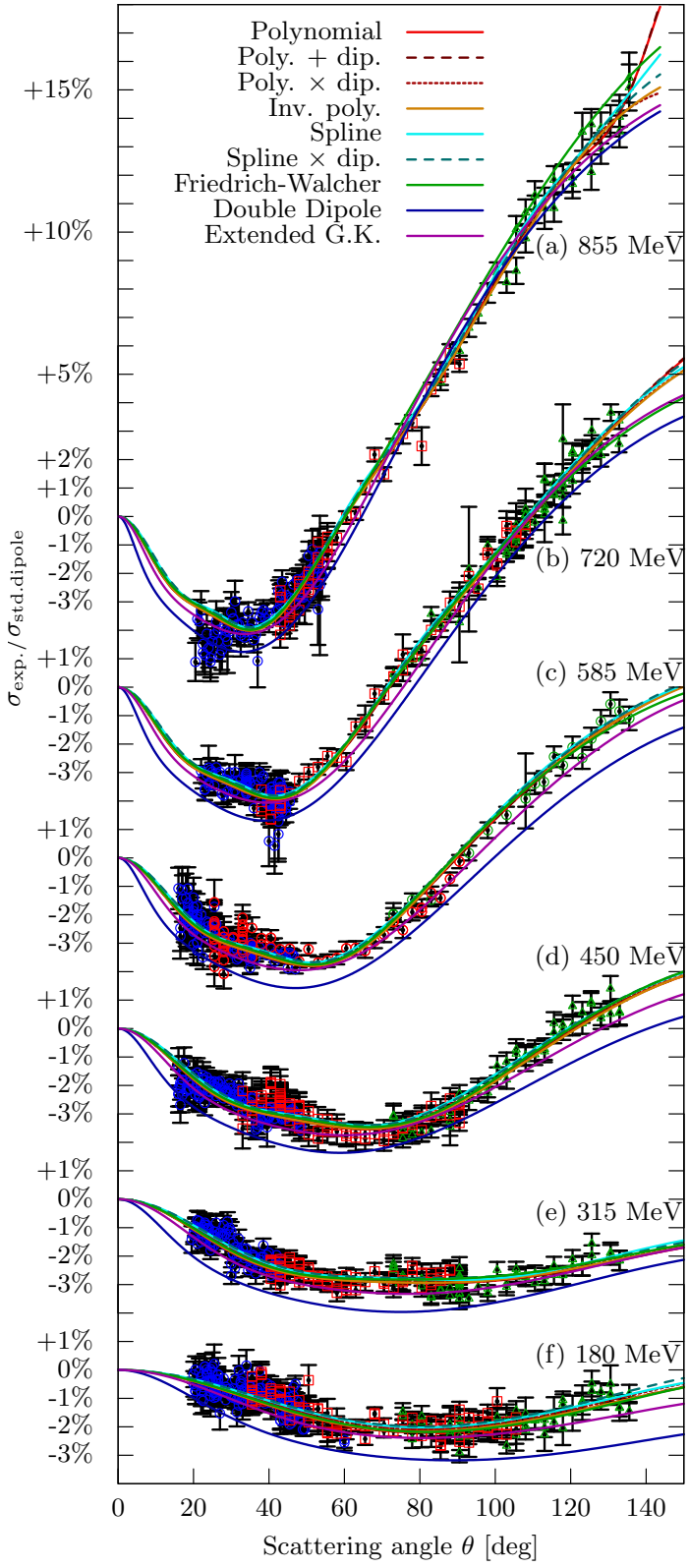

Figure 5: Depiction of the elastic cross section data of the experiment from 2010 and the different fits to the data. The different coloring of the data (red, blue, green) displays the different spectrometers taking the data. On the ordinate the relative difference between the determined form factor and the standard dipole function is shown. An apparent deviation from the standard dipole function in the data is visible. (source: [5])

To describe the proton form factors the dipole function has been used for a long time and only in recent years deviations from the so called standard dipole function in the experimental data were found. The standard dipole function is the following [8]:

$$G_E\left(Q^2\right) = \left(1 - \frac{Q^2}{0.71 \cdot (\mathrm{GeV/c})^2}\right)^{-2}. \tag{23}$$

In Fig. 5 the data for over 1400 elastic cross section measurements are plotted. An apparent deviation from the standard dipole function is clearly visible.
For a static target, indicating that the proton gains no recoil energy, the form factors G_E and G_M are the Fourier transforms of the charge and magnetic density distribution of the proton respectively. If the proton gains recoil energy, the assumption $\vec{q}^2 \approx -q^2$ is no longer valid, hence the form factors are no longer directly related to the Fourier transforms of the density distributions [23]. In the Breit frame, where the initial momentum of the proton is equal to its negative momentum after the scattering process: $\vec{p} = -\vec{p}'$, the form factors are still related to the Fourier transform [24, 25] of the charge or magnetic distributions. Unfortunately the Breit frame is without physical reality because for every value of Q^2 there is a different Breit frame. But there exist model dependent methods to transform these distribution from the Breit frame to the laboratory frame [26]. Nevertheless at low momentum transfer the form factors are approximately related to the density distribution by a Fourier transformation [8]:

$$\begin{aligned} G_{E/M}(\vec{q}) &= \int_{-\infty}^{\infty} \rho_{E/M}(\vec{x}) \cdot \exp\left(\frac{i\vec{q}\cdot\vec{x}}{\hbar}\right) d^3x\,, \\ \int_{-\infty}^{\infty} \rho(\vec{x})_E d^3x &= 1\,, \\ \int_{-\infty}^{\infty} \rho(\vec{x})_M d^3x &= \mu_p\,. \end{aligned} \tag{24}$$

G is one of the form factors and ρ is the respective charge distribution. By the virtue of the normalisation condition it follows [16]:

$$\begin{aligned} G_E(0) &= 1\,, \\ G_M(0) &= \mu_p\,. \end{aligned} \tag{25}$$

By expanding the exponential function in equation 24 it is possible to determine the charge and magnetic mean square radii of the proton assuming that $\rho(x)_{E/M}$ is spherically symmetric [8]:

$$
\begin{aligned}
G_{E/M}\left(Q^2\right) &= \int_{-\infty}^{\infty} \rho\left(x\right)_{E/M} \sum_{n=0}^{\infty} \frac{1}{n!} \left(\frac{i\left|q\right|\left|x\right|\cos\left(\vartheta\right)}{\hbar}\right)^n d^3x \\
&= \int_{0}^{\infty}\int_{-1}^{+1}\int_{0}^{2\pi} \rho_{E/M}\left(r\right)\left(1-\frac{1}{2}\left(\frac{\left|q\right|\left|x\right|}{\hbar}\right)^2\cos^2\left(\vartheta\right)+\ldots\right) d\phi\, d\cos\left(\vartheta\right) r^2 dr \\
&= 4\pi\int_{0}^{\infty} \rho_{E/M}\left(r\right) r^2 dr - \frac{4\pi\left|q\right|^2}{6\hbar^2}\int_{0}^{\infty} \rho_{E/M}\left(r\right) r^4 dr + \ldots . \qquad (26)
\end{aligned}
$$

The mean square charge radius is given by [8]:

$$
\left\langle {r_{E/M}}^2 \right\rangle = 4\pi\int_{0}^{\infty} r^2 \cdot \rho_{E/M}\left(r\right) r^2 dr\,. \qquad (27)
$$

Using this definition in equation 26, the following is obtained:

$$
\begin{aligned}
G_E\left(Q^2\right) &= 1 - \frac{Q^2\left\langle r_E^2\right\rangle}{6\hbar^2} + \ldots\,, \\
\left\langle {r_E}^2\right\rangle &= -6\hbar^2\left.\frac{d\,G_E\left(Q^2\right)}{dQ^2}\right|_{Q^2=0}\,. \qquad (28)
\end{aligned}
$$

In the last expression the mean square charge radius is given by the derivation of the form factor where Q^2 equals zero. If there is any energy transfer to the proton during the scattering process then the charge density distribution and the form factor are not connected via a Fourier transform any more. In this case equation 28 does not describe the mean square charge radius which would be derived from the charge density distribution. But to be consistent with the formalism for heavy nuclei, where the energy transfer to a nuclus during a scattering process is negligible, the radius is still calculated in the same way:

$$
{r_E}^2 \equiv -6\hbar^2\left.\frac{d\,G_E\left(Q^2\right)}{dQ^2}\right|_{Q^2=0}\,. \qquad (29)
$$

To experimentally obtain this radius, measurements at the lowest possible values of Q^2 have to be performed. Applying these formulas to the standard dipole function yields a charge radius of:

$$
r_E \approx 0.81\,\text{fm}\,.
$$

2.1 *Radiative corrections to elastic scattering*

The cross section given by equation 20 cannot be measured. It is the lowest order of Feynman diagrams, the Born approximation (graph (Born) in Fig. 6),

where the scattering of the electron off the proton is mediated by just one exchanged virtual photon. When the cross section for electron-proton scattering is measured, also other Feynman diagrams contribute to the cross section and need to be included in the cross section calculation. However, since the fine structure constant α is much smaller than 1 and every additional vertex in a Feynman diagram contributes a factor α to the cross section calculation, these higher order diagrams become less and less important the more vertices they contain. Therefore only few corrections have to be included in the cross section calculation to obtain the needed level of precision. For elastic scattering there exist corrections to the cross section given in equation 20, which correct for higher order contributions, shown in Fig. 6.
The radiative corrections contribute up to 30% of the total cross section [28] and can be added as correction factors to the cross section [29]:

$$\left(\frac{d\sigma}{d\Omega}\right)_{\text{Corr.}} = \left(\frac{d\sigma}{d\Omega}\right)_{\text{Born}} (1+\delta) \; . \tag{30}$$

The factor δ is divided into different parts correcting for different Feynman diagrams. The first factor corrects for the vacuum polarization (diagram (v1) in Fig.6) [29]:

$$\delta_{\text{vac}} = \frac{2\alpha}{3\pi}\left(\left(\nu^2 - \frac{8}{3}\right) + \nu\frac{3-\nu^2}{2}\ln\left(\frac{\nu+1}{\nu-1}\right)\right) \overset{Q^2 \gg m^2}{\longrightarrow} \frac{2\alpha}{3\pi}\left(-\frac{5}{3} + \ln\left(\frac{Q^2}{m^2}\right)\right) ,$$

$$\nu = 1 + \frac{4m^2}{Q^2} , \tag{31}$$

where m is the mass of the electron. The next factor is the vertex correction (diagram (v2) in Fig. 6) [29]:

$$\begin{aligned}\delta_{\text{vertex}} = \frac{\alpha}{\pi}\Bigg(&\frac{\nu^2+1}{4\nu}\ln\left(\frac{\nu+1}{\nu-1}\right)\ln\left(\frac{\nu^2-1}{4\nu^2}\right) + \frac{2\nu^2+1}{2\nu}\ln\left(\frac{\nu+1}{\nu-1}\right) - 2 + \frac{\nu^2+1}{2\nu} \\ &\times \left(\text{Sp}\left(\frac{\nu+1}{2\nu}\right) - \text{Sp}\left(\frac{\nu-1}{2\nu}\right)\right)\Bigg) \\ \overset{Q^2 \gg m^2}{\longrightarrow}\; &\frac{\alpha}{\pi}\left(\frac{3}{2}\ln\left(\frac{Q^2}{m^2}\right) - 2 - \frac{1}{2}\ln^2\left(\frac{Q^2}{m^2}\right) + \frac{\pi^2}{6}\right) ,\end{aligned}$$

$$\text{Sp}(x) \equiv -\int_0^x dt \frac{\ln(1-t)}{t} . \tag{32}$$

Following is the correction for the emission of a real photon (diagrams (r1) and (r2) in Fig. 6) [29]:

$$\begin{aligned}\delta_R = \frac{\alpha}{\pi}\Bigg(&\ln\left(\frac{(\Delta E_S)^2}{EE'}\right)\left(\ln\left(\frac{Q^2}{m^2}\right) - 1\right) - \frac{1}{2}\ln^2\left(\frac{E}{E'}\right) \\ &+ \frac{1}{2}\ln^2\left(\frac{Q^2}{m^2}\right) - \frac{\pi^2}{3} + \text{Sp}\left(\cos^2\left(\frac{\theta}{2}\right)\right)\Bigg) ,\end{aligned}$$

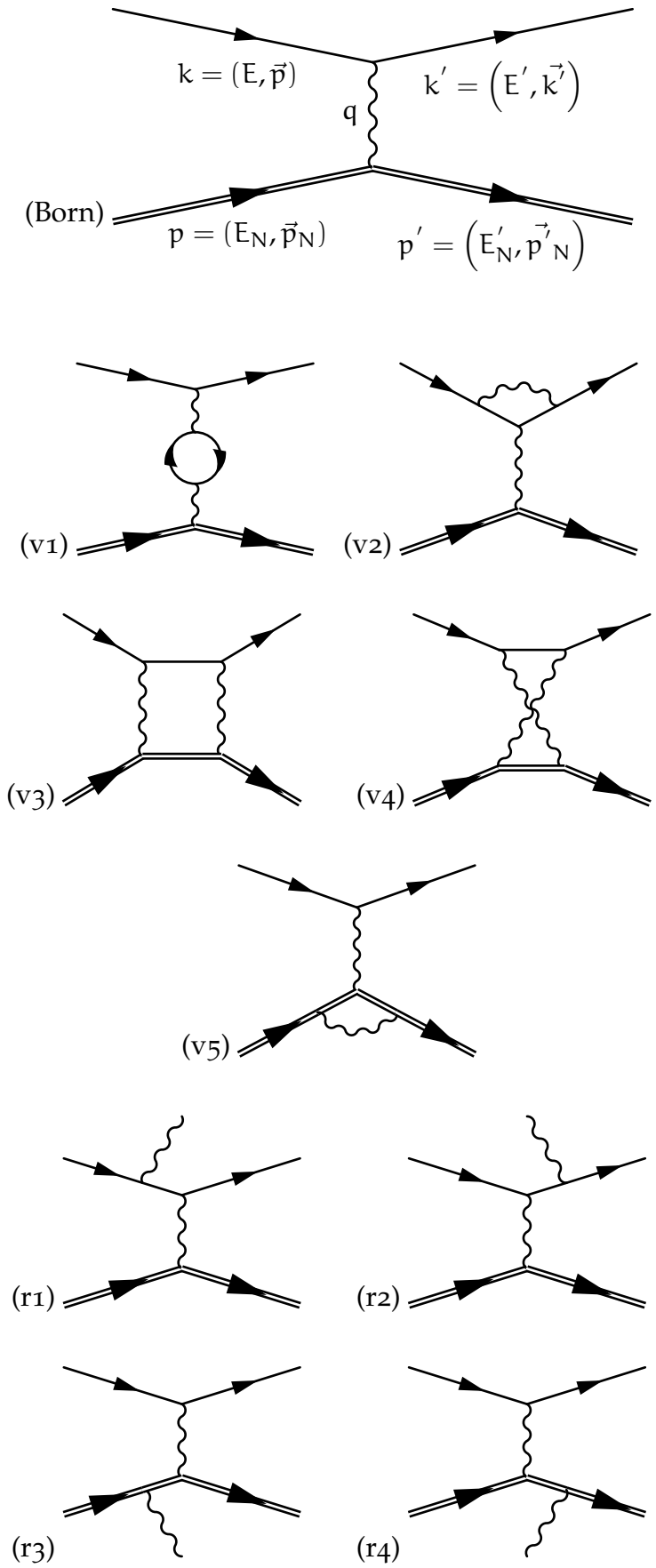

Figure 6: Feynman diagrams considered in the interpretation of elastic scattering data. (source: [27])

$$\Delta E_S = \eta \left(E'_{el} - E' \right) = \frac{E}{E'_{el}} \left(E'_{el} - E' \right) . \tag{33}$$

E is the energy of the incoming electron, E' is the energy of the detected scattered electron and E'_{el} is the energy of an assumed elastically scattered electron at angle θ, i.e. no photon was emitted. Less important are corrections on the proton side (graphs (v3), (v4), (v5), (r3) and (r4) in Fig. 6), because they are suppressed by the mass of the proton [28]:

$$\begin{aligned}
\delta_1 &= \frac{2\alpha}{\pi} \left(\ln \left(\frac{4 (\Delta E_S)^2}{Q^2 x} \right) \ln (\eta) + Sp \left(1 - \frac{\eta}{x} \right) - Sp \left(1 - \frac{1}{\eta x} \right) \right) , \\
\delta_2 &= \frac{2\alpha}{\pi} \left(\ln \left(\frac{4 (\Delta E_S)^2}{M^2} \right) \left(\frac{E'_N}{|\vec{p}'_N|} \ln (x) - 1 \right) + 1 + \frac{E'_N}{|\vec{p}'_N|} \left(-\frac{1}{2} \ln^2 (x) \right. \right. \\
&\quad \left. \left. - \ln (x) \ln \left(\frac{\rho^2}{M^2} \right) + \ln (x) - Sp \left(1 - \frac{1}{x^2} \right) + 2Sp \left(-\frac{1}{x} \right) + \frac{\pi^2}{6} \right) \right) ,
\end{aligned}$$

$$x = \frac{\left(Q^2 + \rho \right)^2}{4M^2}; \ \rho^2 = Q^2 + 4M^2 . \tag{34}$$

M is the mass of the proton, E'_N is the energy of the scattered proton and $\vec{p}'_N$ is the momentum vector of the scattered proton.
The last correction is the Coulomb correction which is due to the interaction of the electron with the Coulomb field of the target [30, 31, 32]:

$$\delta_C = \alpha\pi \frac{\sin (\theta/2) - \sin^2 (\theta/2)}{\cos^2 (\theta/2)} \tag{35}$$

This correction is in the order of 1% and depends only on the angle of the scattered electron. Now these corrections need to be combined in the following way to correct the Born approximation and acquire a more realistic description of the cross section [29]:

$$\left(\frac{d\sigma}{d\Omega} \right)_{corr.} = \left(\frac{d\sigma}{d\Omega} \right)_{Born} \frac{\exp (\delta_{vertex} + \delta_R) + \delta_1 + \delta_2 + \delta_C}{(1 - \delta_{vac}/2)^2} \tag{36}$$

2.2 *Proton radius measurements*

There are different kinds of experiments which can determine information about the proton form factors and consequently about the charge radius of the proton. Following some of these types of experiments are being introduced.

Elastic cross section measurements

The first measurements to determine the proton form factors took place in the 1950s [1], [14]. To determine the form factors, electrons of different energies (100 MeV, 188 MeV and 236 MeV) were scattered from protons. At different

angles ranging from 35° to 138° elastically scattered electrons were measured using magnetic spectrometers. The obtained cross sections were analysed using the Rosenbluth formalism [20]. Deviations from the Mott cross section were already detected in that experiment, see Fig. 3. The proton charge and magnetic radii were both determined to be $(0.77 \pm 0.10) \cdot 10^{-13}$ cm [14].
There have been further experiments [33] [34] of this kind and getting more and more precise in their results. Also more sophisticated radiative corrections were applied to the data as time advanced. In 2010 an experiment took place at the Mainz Microtron (MAMI) where over 1400 different elastic cross section measurements were performed using electron energies ranging from 180 MeV to 855 MeV and a wide range of scattering angles covering a Q^2 range from 0.004 $(\mathrm{GeV}/c)^2$ to 1 $(\mathrm{GeV}/c)^2$ [35], [5]. There the charge radius of the proton was determined to be $0.879(5)_{\mathrm{stat}}(4)_{\mathrm{sys}}(2)_{\mathrm{model}}(4)_{\mathrm{group}}$ fm. This value was in accordance with other measurements of that kind in the recent time. For the analysis of these data the Rosenbluth separation was not applied. Instead a direct fit of models for G_E was applied to the cross section data and this way the most suitable form factor parametrisation was determined. Different fit models were tested and in the final analysis a spline fit was used [5]. Other models which were tested were dipoles, dipoles multiplied by polynomials, double dipoles, simple polynomials and some others, all described in detail in Ref. [5]. In Fig. 5 the data for all elastic cross section measurements are plotted. The different functions tested to fit the data are shown as well as the spline model which was used for that experiment to extract the charge radius of the proton.
It is also possible to extract the proton form factors from muon-proton scattering. Since it is rather elaborate to produce muons, not so many and rather unprecise elastic cross section measurements have been accomplished, for example see Ref. [36]. To improve the situation a new experiment at PSI (Paul Scherrer Institute) is being prepared to measure both muon-proton and electron-proton and also antimuon-proton and positron-proton elastic scattering cross sections [37]. The designation is to determine the charge radius of the proton at a level of precision of about 0.01 fm. As this experiment will measure both particle and antiparticle scattering cross sections, it is possible to determine also the two-photon scattering amplitudes which are needed as corrections to the elastic cross section especially for the muon-proton scattering data [37]. This renewed interest is due to results from atomic spectroscopy as described below.

Polarization measurements

Another method to obtain knowledge about the proton form factors are polarization measurements [25, 38]. When scattering longitunally polarized elec-

trons off unpolarized protons, the polarization transferred to the proton contains information about the ratio of the proton form factors [39]:

$$\frac{G_E}{G_M} = -\frac{E_e + E_e'}{2M} \tan\left(\frac{\theta}{2}\right) \frac{P_t}{P_l}. \tag{37}$$

Here P_t are the transverse and P_l the longitudinal polarization transferred to the proton, respectively. With these kinds of measurements the extracted ratio of the form factors does significantly differ from unity down to the lowest values of Q^2 of the measurement in Ref. [39], which is in contradiction with the cross section experiments where the ratio is almost unity. One possible explanation for this discrepancy are uncertainties in the two-photon exchange processes on which the elastic scattering cross section depends more strongly than the polarization measurements [40, 41].

Atomic spectroscopy

Yet another method to determine the charge radius of the proton is to measure transition frequencies in hydrogen [42]. For this purpose a transition frequency has to be chosen which depends on the charge radius of the proton. This is true for S-state wave functions where electrons spend most of their time inside the proton itself. In a simplified picture the energies of the S-state in hydrogen are given by [4]:

$$\begin{aligned} E(n) &\simeq -\frac{R_\infty}{n^2} + \frac{L_{1S}}{n^3}, \\ L_{1S} &\simeq \left(8.172 + 1.56 \cdot {r_E}^2\right) \text{ MHz}. \end{aligned} \tag{38}$$

Here r_E is expressed in femtometers. R_∞ is the Rydberg constant and L_{1S} is the Lamb shift of the 1S ground state. By measuring two different transition frequencies, for example $1S - 2S$ [43] and $2S - 8S$ [44], both the Rydberg constant and the charge radius of the proton can be determined. Otherwise it is also possible to extract the charge radius of the proton directly from the $2S - 2P$ transition which is not sensitive to the Rydberg constant [4]. The determinations of the charge radius of the proton done with different transitions, see Fig. 7, are in agreement with the nuclear cross section determinations.

Spectroscopy of muonic hydrogen

It is also possible to determine r_E by measuring transition frequencies in muonic hydrogen. Muonic hydrogen consists of a proton and a muon instead of a proton and an electron like in hydrogen. Since a muon is about 200 times as heavy as an electron the probability of it being inside the proton is increased for a factor of about eight million [45]. This indicates that muonic hydrogen is much more sensitive to the charge radius of the proton than normal hydrogen [2]. It is possible to determine the charge radius of the proton

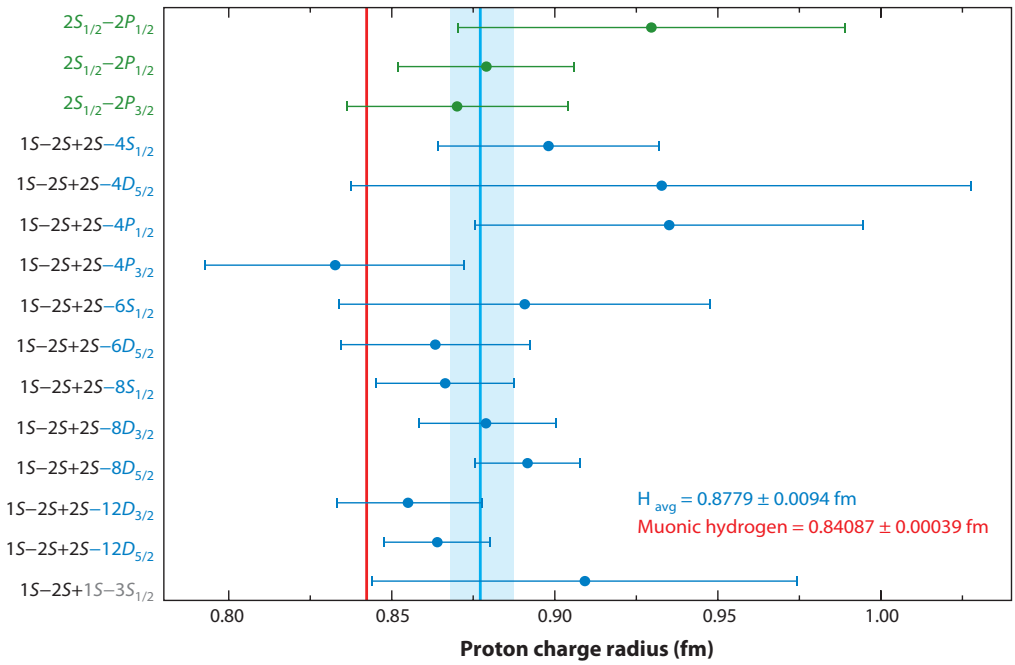

Figure 7: Proton charge radii determined with hydrogen spectroscopy using different transition frequencies. The result of the spectroscopy of muonic hydrogen is also plotted. (source: [4])

by measuring the energy difference for the $2S_{1/2}^{F=1} - 2P_{3/2}^{F=2}$ transition where the transition energy is given by [46]:

$$\Delta E = 209.9779(49) - 5.2262 \cdot {r_E}^2 + 0.0347 \sqrt{{r_E}^2}^3 \, \text{meV} \, . \tag{39}$$

Here r_E is expressed in fm. r_E amounts to about 1.8% of ΔE. Fig. 8 shows the measured resonance spectrum for this transition. The extracted charge radius of the proton for muonic hydrogen is [2]:

$$r_E = 0.84087(39) \, \text{fm} \, . \tag{40}$$

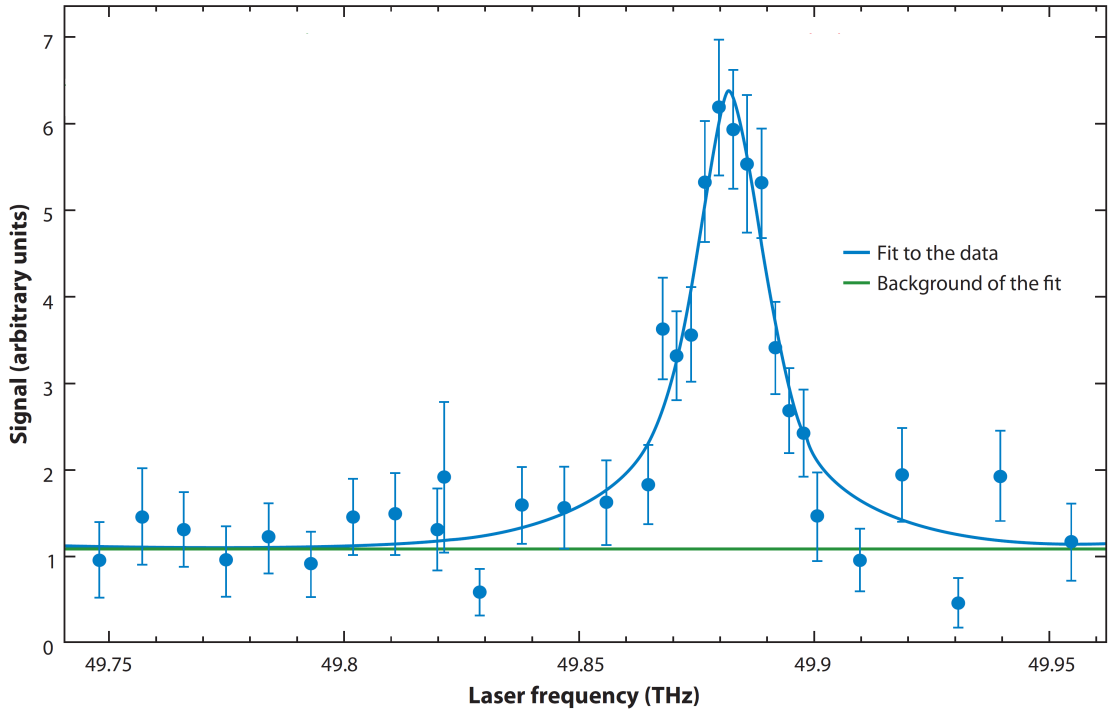

Figure 8: Resonance spectrum of the $2S - 2P$ transition in muonic hydrogen, the peak displays the frequency of the measured resonance. (source: [4])

The Proton Radius Puzzle

The results from elastic cross section measurements in hydrogen and hydrogen spectroscopy, where the charge radius of the proton is found to be $r_E = 0.8751(61)\,\text{fm}$ [3], disagree with the results from muonic hydrogen spectroscopy, where the charge radius of the proton is found to be $r_E = 0.84087(39)\,\text{fm}$ [2]. In Fig. 9 important measurements of the charge radius of the proton are displayed to visualise the discrepancy. The discrepancy is about 4% or 6 standard deviations. The theory of QED tells that the charge radius of the proton should be the same for the extraction with electrons or muons. As there exists no explanation for this discrepancy it has been called the proton radius puzzle. To solve this puzzle more precise measurements are needed. In particular measurements of the electron cross section at the lowest possible values of Q^2 are needed which would allow for a more precise determination of the charge radius of the proton. Dealing with measurements at the lowest known values of Q^2 is the basis of the experiment described in this work.

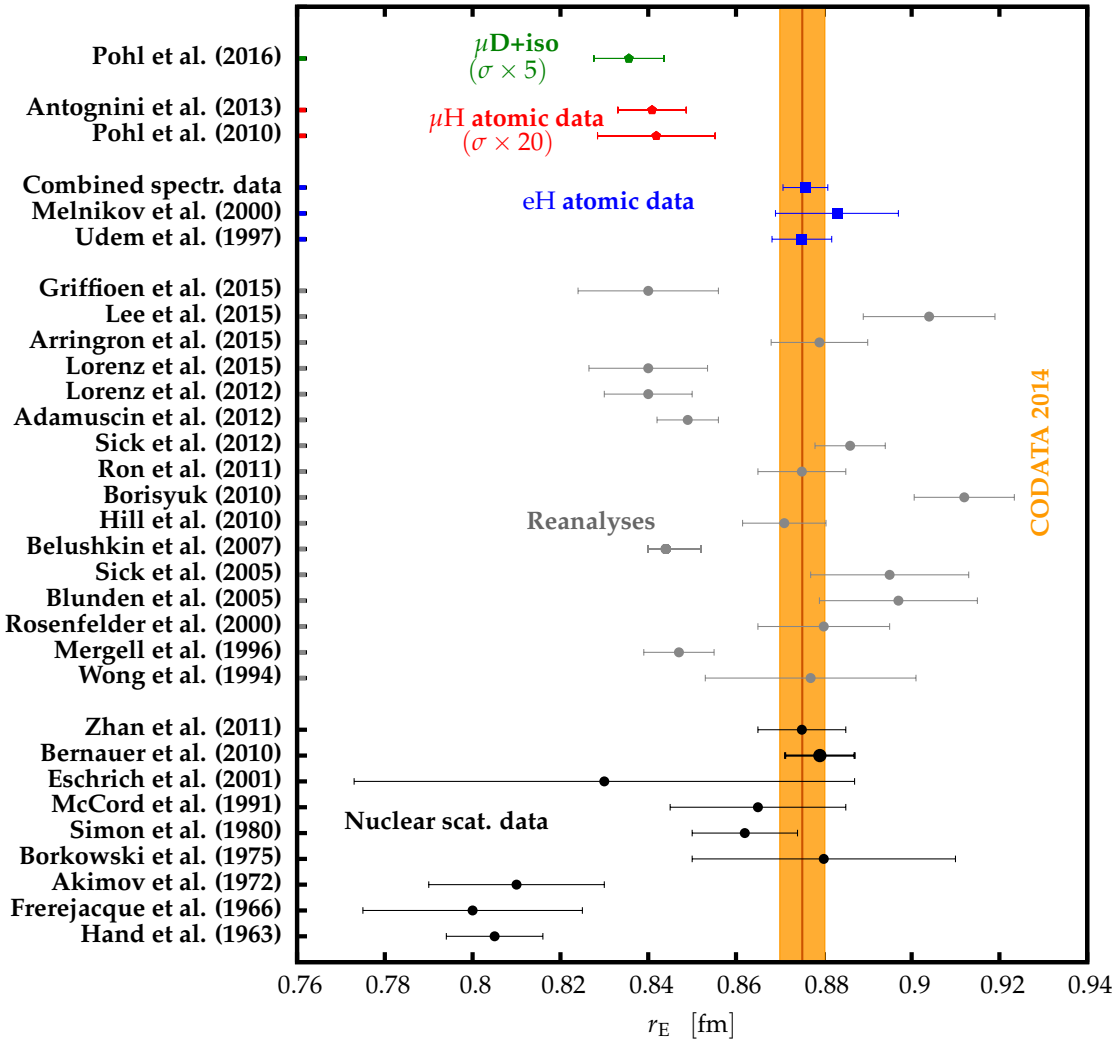

Figure 9: An overview of important measurements of the charge radius of the proton. Full circles show findings of the scattering experiments. Full squares represent values obtained from hydrogen spectroscopy. The values determined from the muonic measurements are represented by pentagons. The uncertainties of muonic data are enlarged for a better visualization. The CODATA value is symbolised by the dark orange line while the orange band symbolises its uncertainty. (source: [47, 48])

3

INITIAL STATE RADIATION

To measure the cross section for elastic electron scattering at very low values of Q^2 a very low beam energy or a very low detected scattering angle are needed, as can be seen from equation 18. At the MAMI facility both are limited, and already in the experiment of 2010, mentioned above, measurements at the lowest possible scattering angle and energy were performed [5]. The lowest beam energy with stable beam conditions is 195 MeV, this limitation is due to the design of the accelerator. The lowest detectable scattering angle is limited to about 15° because of the configuration of the spectrometer hall. This implies that the lower limit, when measuring elastically scattered electrons, for Q^2 is $0.004\,(\mathrm{GeV}/c)^2$. Therefore another method is needed to be able to measure cross sections at even lower Q^2 without changing the overall setup of the accelerator or the detection facility. One possible method to do this is to measure not only the elastic cross section but also the radiative tail. This approach has already been used in particle physics to measure e^+e^- into hadrons cross sections in a single experiment over a large range of center of mass energies [49, 50]. The radiative tail arises predominantly from electrons emitting Bremsstrahlung, see Fig. 11 (bottom) and Fig. 12 (top). Unfortunately with the detector setup at MAMI the emitted real photon cannot be detected, just the scattered electron is measured. In Fig. 10 a simulation of the elastic peak and the radiative tail in terms of the energy of the scattered electron is shown for a beam energy of 195 MeV. The boundary between elastic peak and radiative tail in the plot is somewhat arbitrary. On the top abscissa Q^2_{calc} is calculated only with information from the scattered electrons assuming elastic scattering. Considering equation 18 with equation 8 gives the following equation:

$$Q^2 = \frac{4 \cdot E'^2 \cdot \sin^2\left(\frac{\theta}{2}\right)}{1 - (Mc^2)^{-1} \cdot (1 - \cos(\theta))}\,. \tag{41}$$

Equation 8 is only valid for elastic scattering. This indicates for the calculated Q^2_{calc} in Fig. 10 an initial state radiation process has been assumed where the incoming electron emitted a real photon before its interaction with the proton. In this case the electron has already lost part of its initial energy and when the scattering process takes place its energy is lower than the beam energy was. In this case the usage of equation 41 to calculate Q^2_{calc} yields the value of Q^2 at the vertex with which the proton is probed. Consequently Q^2 is lower than for elastic scattering. Hence the cross section at lower values of Q^2 than in elastic cross section experiments can be detected without changing anything about the setup.

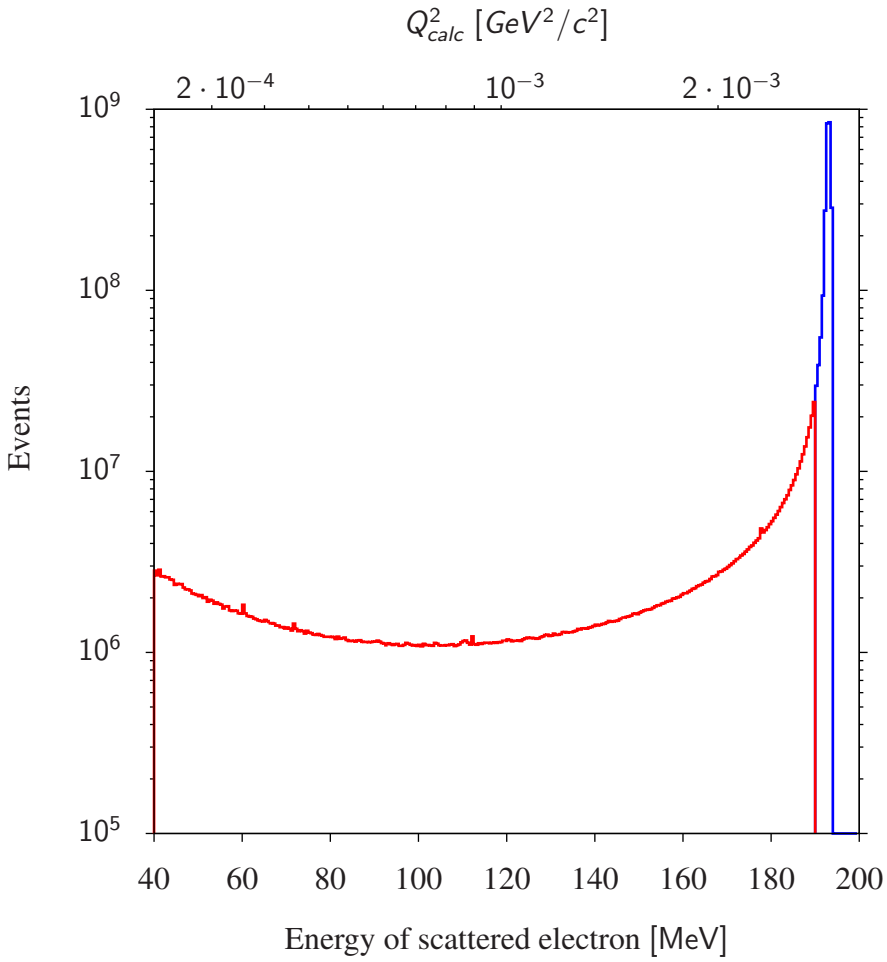

Figure 10: Simulation of the elastic peak (blue) and radiative tail (red) in terms of the energy of the scattered electron for an incoming electron energy of 195 MeV. On the second abscissa also the Q^2_{calc} calculated with the energy and scattering angle of the scattered electron is shown. The boundary between the peak and tail is arbitrary and was for this plot chosen at 190 MeV.

However, if the electron emits a real photon after the scattering process, the so called final state radiation (FSR), then the usage of equation 41 is no longer valid and therefore the calculated Q^2_{calc} as well as the form factor it implies is not correct. The measured spectrum in Fig. 10 arises from initial as well as from final state radiation and of course further Feynman processes. Therefore the calculated Q^2_{calc} and the form factor it implies which is displayed on the second abscissa is correct only for a part of the events. To learn the overall correct Q^2 and form factor distribution a sophisticated simulation is used [51]. In the simulation the Bethe-Heitler diagrams, initial and final state radiation, as well as the Born diagrams are explicitly calculated, see Fig. 11 and 12. Higher order diagrams are considered as effective corrections. Thus information about Q^2 and the underlying form factor distribution are available and can be used to distinguish initial from final state radiation. In Fig. 13 the correct Q^2 is

displayed on the ordinate as well as Q^2_{calc} which is calculated using only the scattering angle θ and E'.

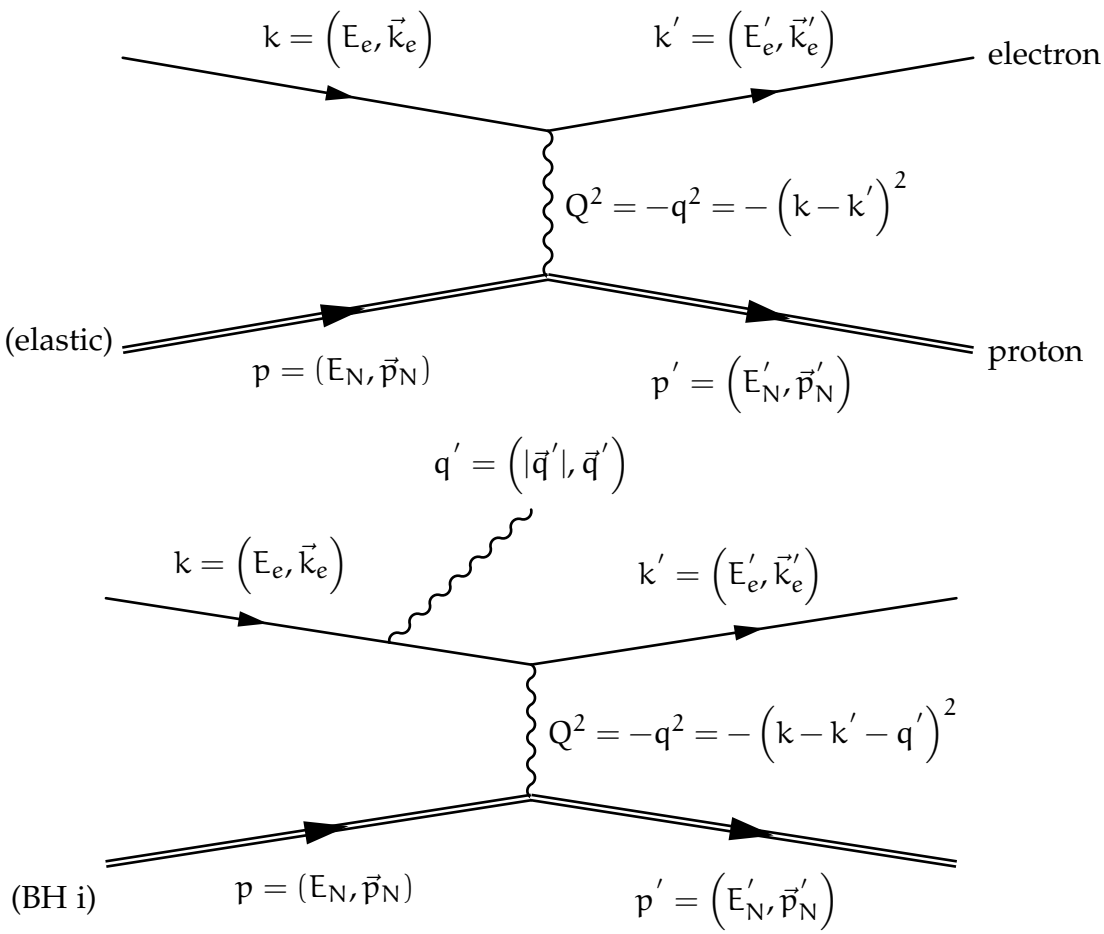

Figure 11: Top: Feynman diagram for elastic electron-proton scattering. Bottom: Bethe-Heitler diagram where the electron emits a real photon before the scattering process, also called initial state radiation.

In the plot the downwards curved red line is caused by initial state radiation. In this case Q^2 of the initial state radiation diagram is the same as if it is calculated from E' and θ using equation 41. The horizontal red line in the plot is caused by final state radiation. In this case Q^2 is the same as for elastic scattering where no photon is emitted because the photon is emitted after the scattering process hence it does not affect Q^2. For most events the photon is emitted in the direction of the electron emitting it, see Fig. 14. The events between, above and below the two distinctive red lines are caused by photons emitted in directions different than the directions of the incoming or outgoing electron.

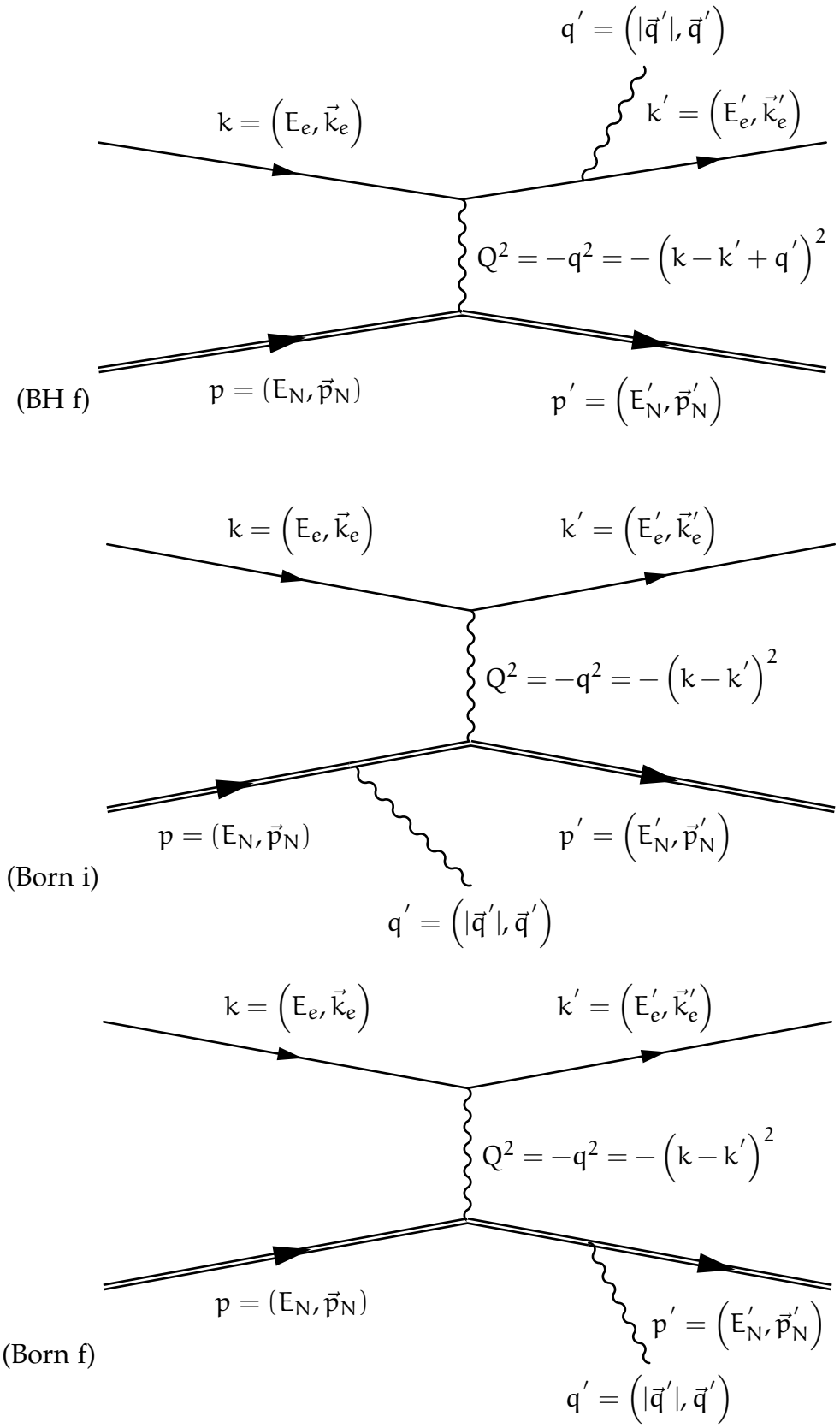

Figure 12: Top: Bethe-Heitler diagram where the electron emits a real photon after the scattering process, also called final state radiation. Middle: Born diagram where the proton emits a real photon before the scattering process. Bottom: Born diagram where the proton emits a real photon after the scattering process.

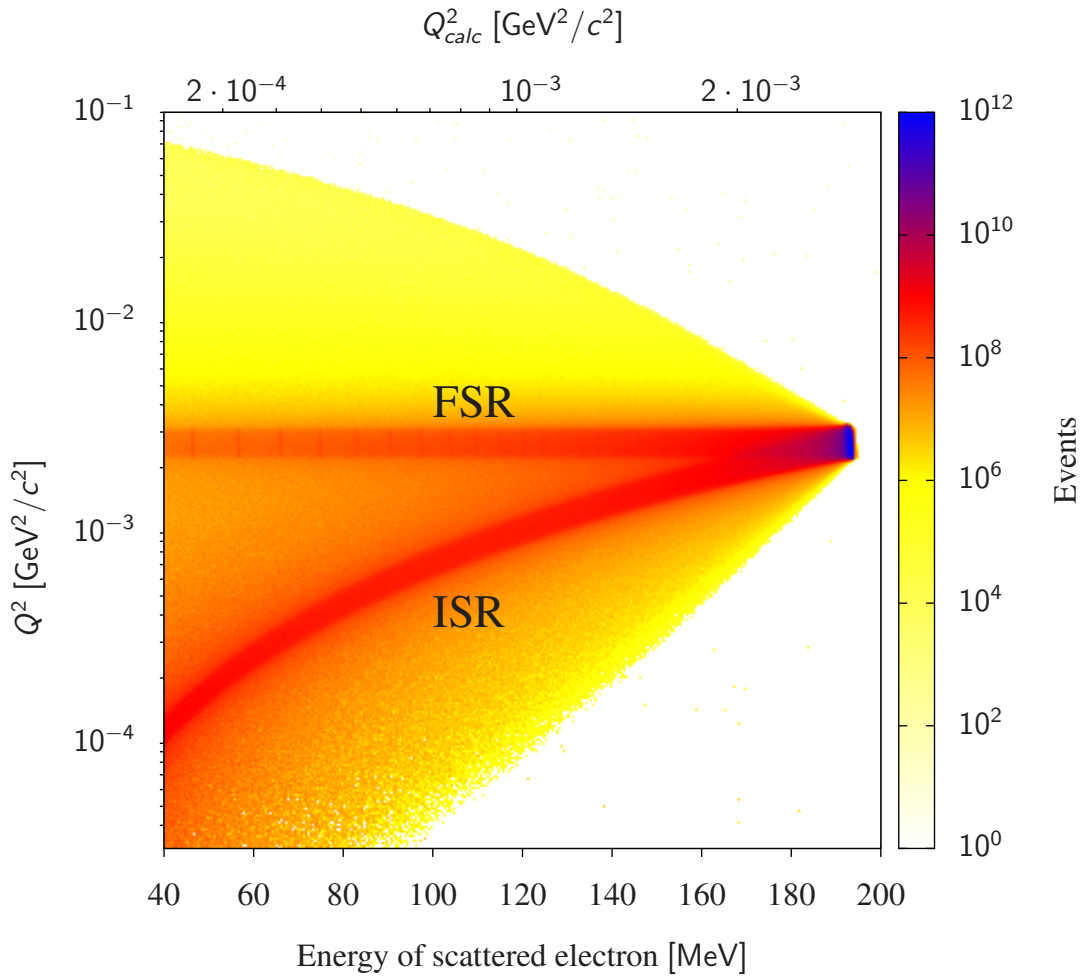

Figure 13: Results of the full simulation as a function of Q^2 at the vertex on the ordinate and the energy of the scattered electron and Q^2_{calc} on the abscissa for a beam energy of 195 MeV. Q^2_{calc} is calculated using the energy of the scattered electron and θ assuming only an ISR process. (source: [52])

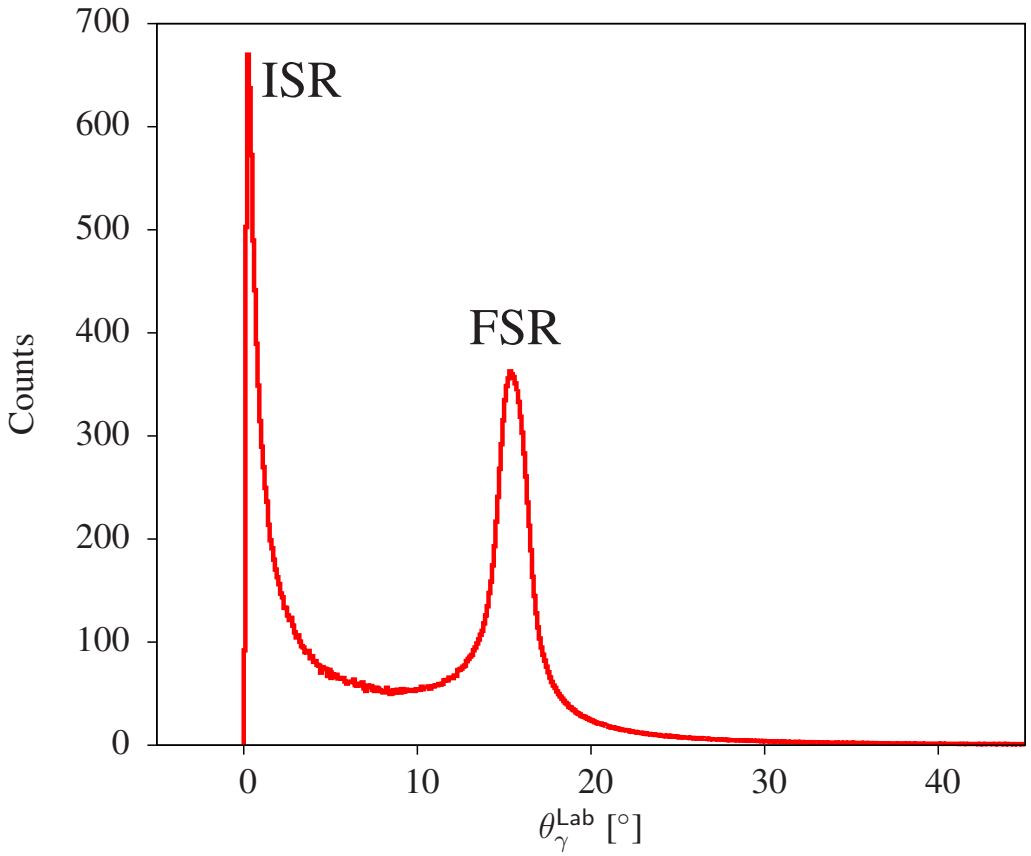

Figure 14: Simulation as a function of the angle of the emitted photon θ_γ^{Lab} with respect to the direction of the beam. The scattered electron was detected at about 15°. The peak at about 0° arises from electrons emitting a photon before the scattering process (ISR), the peak at about 15° arises from electrons emitting a photon after the scattering process (FSR).

By measuring just the scattered electron during the actual experiment together with a simulation it is possible to distentangle the different contributions in the radiative tail. In the simulation the only parameter which can be varied is the proton electric form factor. As this experiment will take place at a scattering angle of about 15° and low Q^2 the contribution of G_M to the cross section is below 0.5%. Therefore it suffices to use the already known behaviour of G_M for the simulation from Ref. [27]. Then the only free parameter is G_E and this has to be adjusted in order to match the data from the experiment and the data from the simulation. This is the idea behind the usage of initial state radiation in order to acquire the proton electric form factor at very low values of Q^2 without changing the overall setup of the MAMI facility.

3.1 *Next order corrections*

Using the Feynman rules for the leading order Bethe-Heitler and Born diagrams in Fig. 11 and 12 the amplitudes are as follows (here in Heaviside-Lorentz units):

$$\mathfrak{M}_{BH,i} = -e^3 \overline{u}\left(k'\right) \epsilon_\nu^* \gamma^\mu \frac{\not{k} - \not{q} + m}{(k-q)^2 - m^2} \gamma^\nu u(k) \frac{1}{q^2} \overline{u}\left(p'\right) \Gamma_\mu u(p) \,,$$

$$\mathfrak{M}_{BH,f} = -e^3 \overline{u}\left(k'\right) \epsilon_\nu^* \gamma^\nu \frac{\not{k}' + \not{q} + m}{(k'+q)^2 - m^2} \gamma^\mu u(k) \frac{1}{q^2} \overline{u}\left(p'\right) \Gamma_\mu u(p) \,,$$

$$\mathfrak{M}_{Born,i} = e^3 \overline{u}\left(p'\right) \epsilon_\nu^* \Gamma^\mu \frac{\not{p} - \not{q} + M}{(p-q)^2 - M^2} \Gamma^\nu u(p) \frac{1}{q^2} \overline{u}\left(k'\right) \gamma_\mu u(k) \,,$$

$$\mathfrak{M}_{Born,f} = e^3 \overline{u}\left(p'\right) \epsilon_\nu^* \Gamma^\nu \frac{\not{p}' + \not{q} + M}{(p'+q)^2 - M^2} \Gamma^\mu u(p) \frac{1}{q^2} \overline{u}\left(k'\right) \gamma_\mu u(k) \,,$$

$$\not{x} = \gamma^\mu x_\mu \,. \tag{42}$$

ϵ is the photon polarization vector, m is the electron mass, M is the proton mass and p, p', k, k' and q are four-vectors like in Fig. 11. To calculate the cross section, equations 15 and 16 have to be used.
But as already mentioned also higher order diagrams contribute to these four diagrams. Therefore to get even more precise results the next order diagrams can be used as an effective correction. These diagrams need different efforts to be calculated. Diagrams which contain loops take a lot of time to be calculated, but fortunately they do not vary much with respect to Q^2 for this kind of experiment and can be used as an effective correction for a whole setup, see also chapter 6.1. These diagrams are visualised in Fig. 15. A more detailed description about these diagrams may be found in Ref. [29].
Another group of diagrams considered as effective correction to the first order exact calculation are soft photon corrections on the electron side. These diagrams are shown in Fig. 16. The correction for these diagrams are currently approximated as an effective correction using elastic corrections to the cross section, see chapter 6.1, applying the following expression [29]:

$$\left|\mathfrak{M}^{\text{soft photon}}_{\text{BH+Born}}\right|^2 = |\mathfrak{M}_{\text{BH+Born}}|^2 \cdot \left(\frac{e^2}{4\pi^2}\left(-\frac{1}{\epsilon_{IR}} + \gamma_E - \ln\left(\frac{4\pi\mu^2}{m^2}\right)\right)\left(\frac{\nu^2+1}{2\nu}\ln\left(\frac{\nu+1}{\nu-1}\right) - 1\right) + \delta_R\right) . \tag{43}$$

All variables in the brakets in equation 43 are explained in Ref. [29]. δ_R represents the finite part of the correction and contributes to the overall cross section. The rest cancels out against corresponding terms in the virtual corrections. δ_R is calculated in the limit that $Q^2 \gg m^2$ [29]:

$$\delta_R = \frac{\alpha}{\pi}\left(\ln\left(\frac{\left(\Delta\tilde{E}_S\right)^2}{\tilde{E}_e\tilde{E}'_e}\right)\left(\ln\left(\frac{Q^2}{m^2}\right) - 1\right) - \frac{1}{2}\ln^2\left(\frac{\tilde{E}_e}{\tilde{E}'_e}\right) + \frac{1}{2}\ln^2\left(\frac{Q^2}{m^2}\right) - \frac{\pi^2}{3} + Sp\left(\cos^2\left(\frac{\tilde{\theta}}{2}\right)\right)\right) . \tag{44}$$

To calculate the correction given by equation 44 a special coordinate system is needed, see Ref. [29]. The energies $\tilde{E}_e$ and $\tilde{E}_e^{'}$ and the scattering angle of the electron $\tilde{\theta}$ are given in this coordinate system by:

$$
\begin{aligned}
M_{m1}^2 &= \left(p^{'} + l\right)^2 = \left(p + q - q^{'}\right)^2 , \\
\tilde{E}_e &= \frac{M}{M_{m1}} \left(E_e - \frac{Q^2}{2M} - \frac{k \cdot q^{'}}{M} \right) , \\
\tilde{E}_e^{'} &= \frac{M}{M_{m1}} \left(E_e^{'} + \frac{Q^2}{2M} - \frac{k^{'} \cdot q^{'}}{M} \right) , \\
\sin^2\left(\frac{\tilde{\theta}}{2}\right) &= \frac{E_e E_e^{'}}{\tilde{E}_e \tilde{E}_e^{'}} \sin^2\left(\frac{\theta}{2}\right) , \\
\Delta\tilde{E}_S &= \frac{M_{m1}^2 - M^2}{2M_{m1}} .
\end{aligned}
\tag{45}
$$

Here l is the four-vector of the soft photon.
There are also corrections on the proton side which are again included in terms of an elastic approximation see chapter 2.1, equation 34. The diagrams for these processes are illustrated in Fig. 17. In the same way the Coulomb correction is applied like in equation 35.
These corrections then need to be applied in the following way to the Bethe-Heitler and Born cross section analogous to equation 36 [29]:

$$
\left(\frac{d\sigma}{d\Omega}\right)_{\text{BH+Born corr.}} = \left(\frac{d\sigma}{d\Omega}\right)_{\text{BH+Born}} \frac{\exp\left(\delta_{\text{vertex}} + \delta_R\right) + \delta_1 + \delta_2 + \delta_C}{\left(1 - \delta_{\text{vac}}/2\right)^2} . \tag{46}
$$

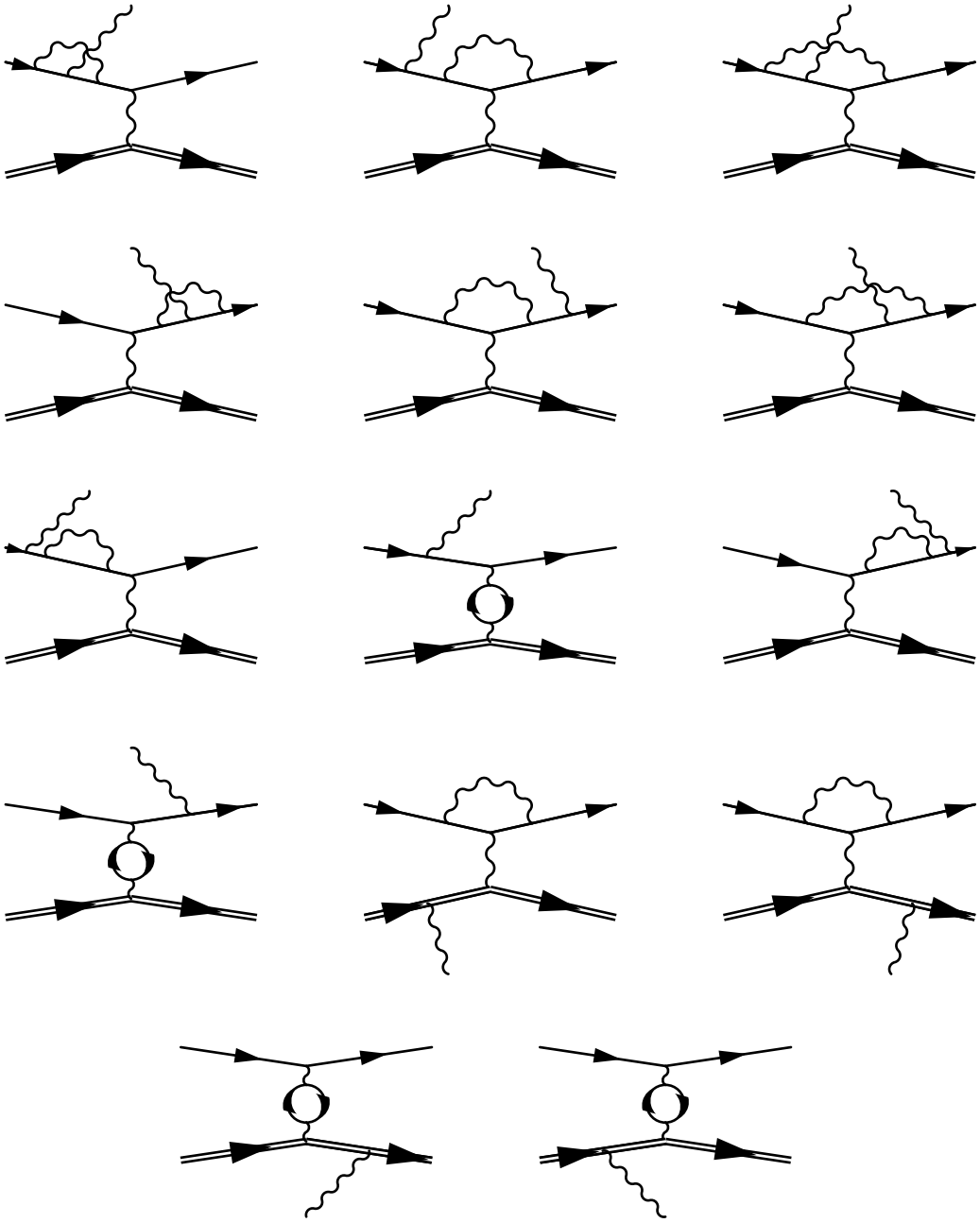

Figure 15: Next order virtual correction diagrams to the Bethe-Heitler and Born diagrams.

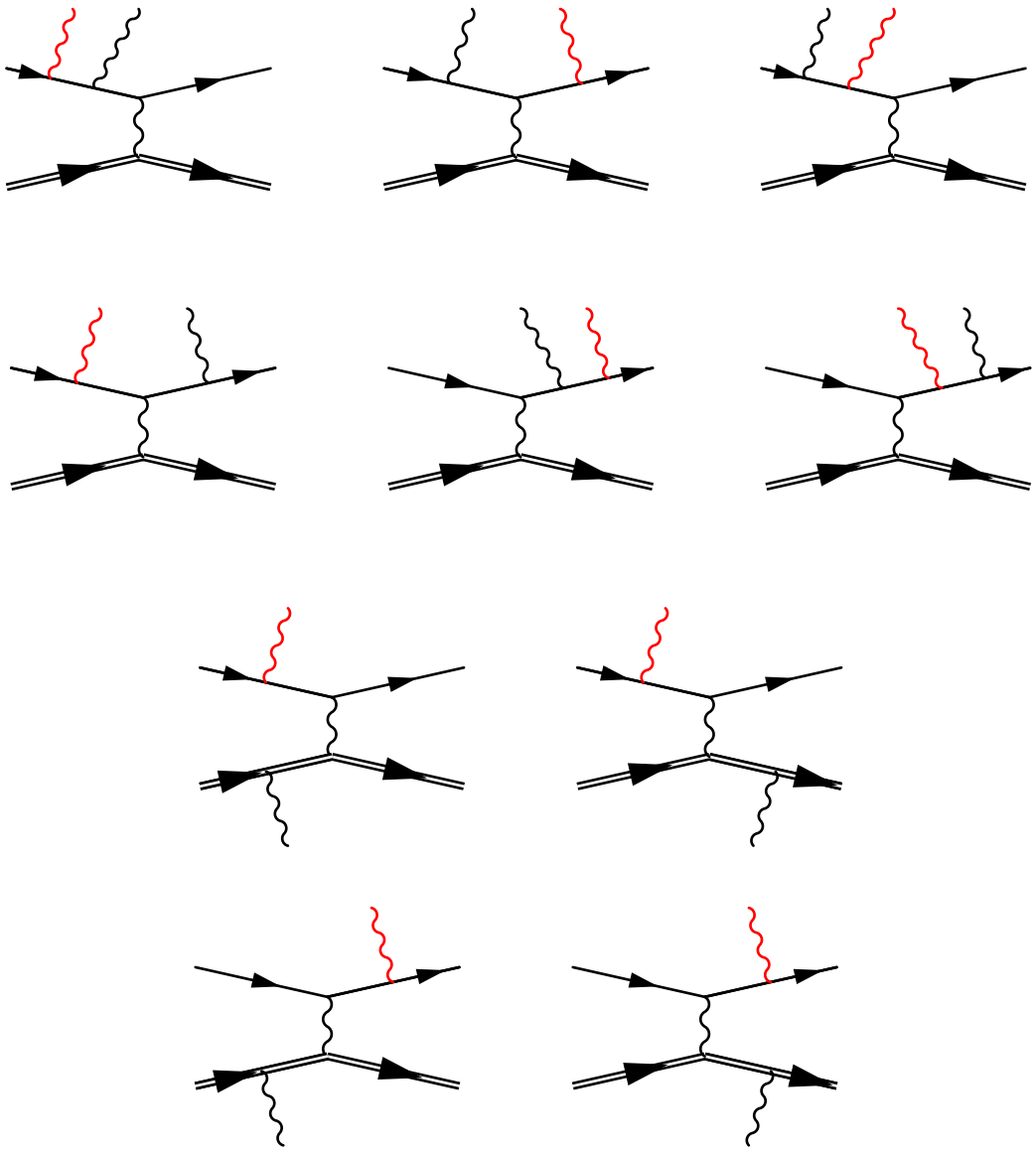

Figure 16: Next order soft photon emission contribution on the electron side to the Bethe-Heitler and Born diagrams. The soft photons are colored in red.

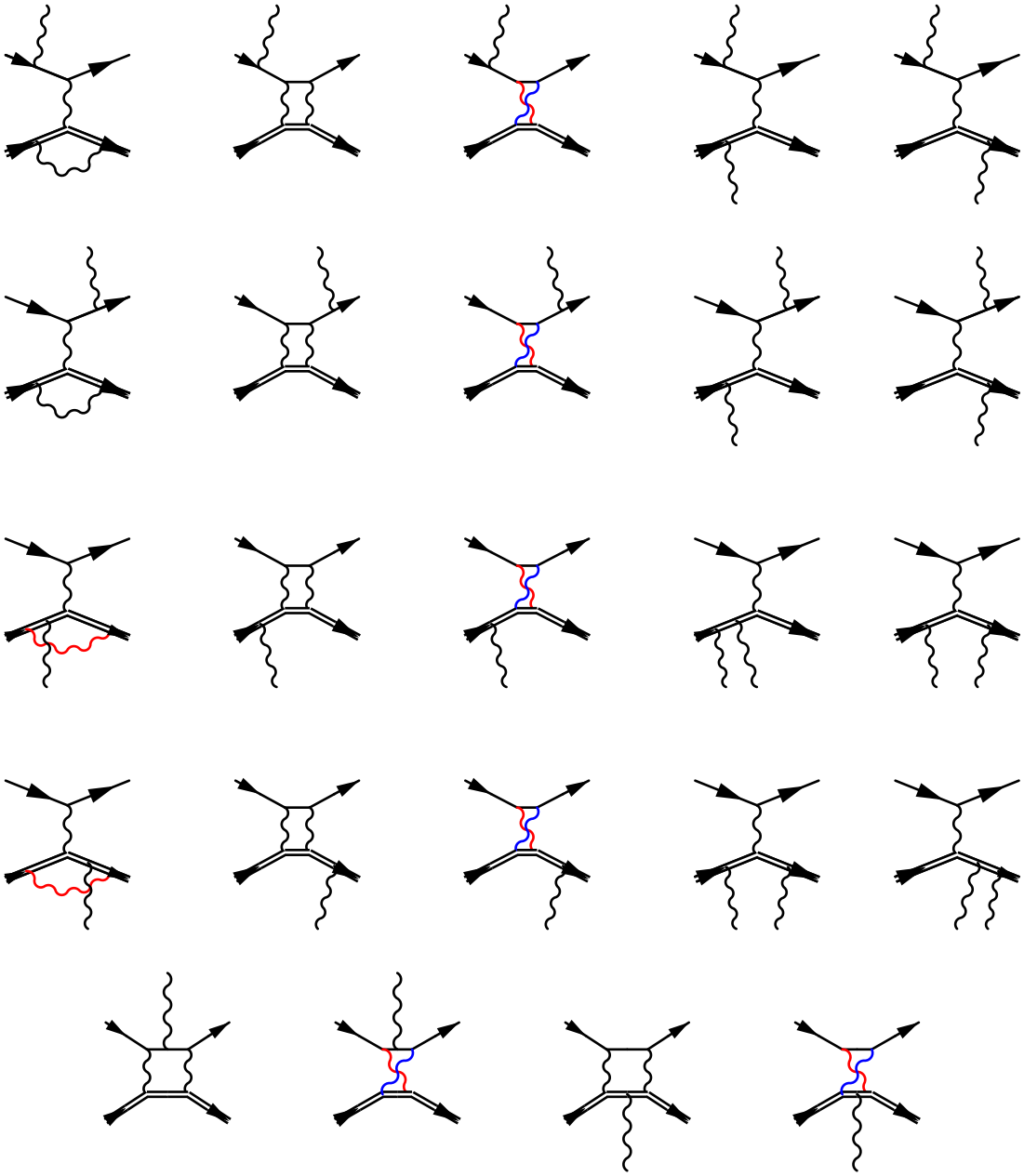

Figure 17: Next order proton vertex correction diagrams. The colors are used to make the diagrams clearer in the cases where the lines cross each other.

4

EXPERIMENTAL SETUP

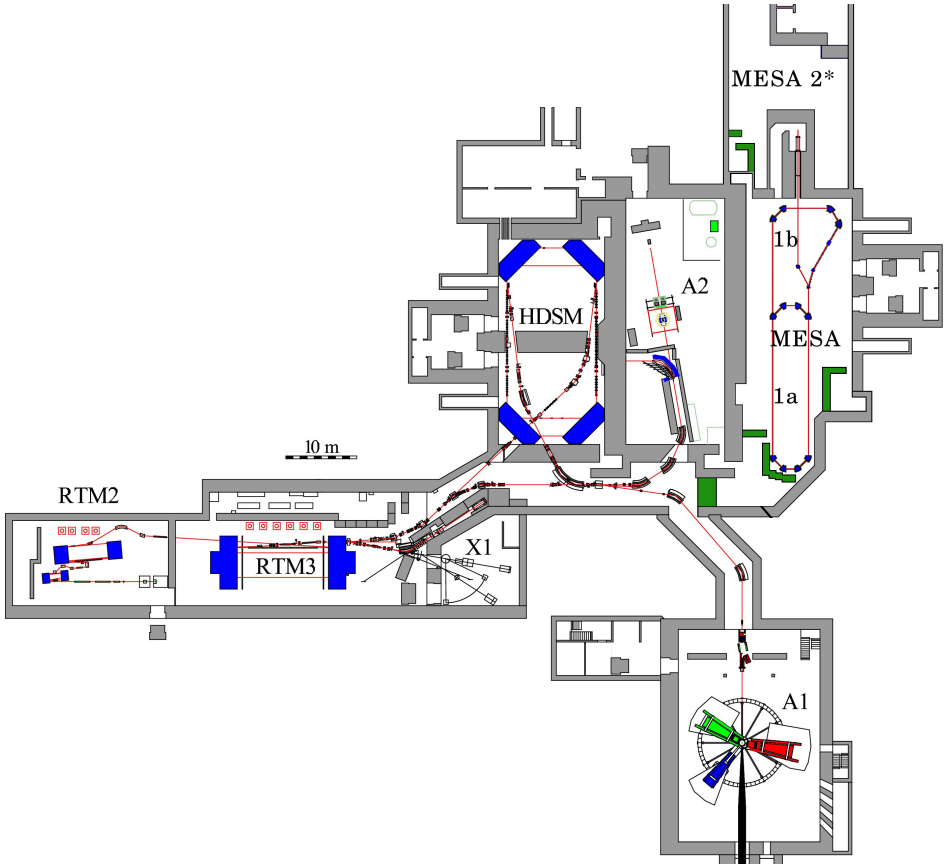

Figure 18: Floor plan of the MAMI facility; the red lines display the electron beam lines. The actual experiment took place in the hall labeled A1. (source: [53]).

The experiment to determine the proton electric form factor took place at the MAMI (Mainz Microtron) facility. The facility encompasses an accelerator and three experimental areas: X1, A2 and A1, as well as the new MESA accelerator which is under construction, see Fig. 18. The MAMI accelerator provides an electron beam and consists of five different stages: injector, RTM1, RTM2, RTM3 and HDSM. The injector is a linear accelerator and has an extraction energy of 3.97 MeV. RTM1, RTM2 and RTM3 are race track microtrons. They have an extraction energy of 14.86 MeV, 180 MeV and 855 MeV respectively. The HDSM is a harmonic double sided microtron and its nominal extraction energy is 1.5 GeV [54]. For experiments beam energies between 160 MeV and 1604 MeV in various steps can be delivered from RTM3 or the HDSM [55]. The (1σ) en-

ergy spread is 30 keV at 855 MeV and 110 keV at 1.5 GeV [56]. The accelerator produces a high quality continuous wave electron beam with a maximum beam current of 100 µA [57]. There are two different electron sources, one for an unpolarized and one for a polarized beam.

Figure 19: Picture of the A1 hall where the experiment was performed. The three spectrometers A (red), B (blue) and C (green) are visible. The shielding houses of Spec. A and Spec. C are opened and the detectors are visible. (source: [27])

This experiment took place in the A1 experimental hall using unpolarized beam energies of 495.25 MeV, 330.26 MeV and 195.15 MeV with beam currents ranging from 10 nA to 1 µA. There are three spectrometers called Spec. A, Spec. B and Spec. C, see Fig. 19. For the measurement Spec. A and Spec. B were used. Spec. A consists of a quadrupol, a sextupol and two dipoles, see Fig. 20

	Spec. A	Spec. B
Central scattering angle [deg]	$23-155$	$15-57$
Maximum central momentum [MeV/c]	665	810
Maximum solid angle [msr]	28	5.6
Momentum acceptance	$\pm 10\%$	$\pm 7.5\%$
Momentum resolution	10^{-4}	10^{-4}
Angular resolution at target [mrad]	$\leqslant 3$	$\leqslant 3$
Position resolution at target [mm]	$3-5$	$\leqslant 1$
Length of central path [m]	10.75	12.03

Table 1: Main parameters of the spectrometers A and B. The momentum acceptance is with respect to the central momentum.

left. The quadrupol and the sextupol are used to enlarge the acceptance in the non-dispersive plane and to correct for optical aberrations respectively [58, 59]. To achieve a high momentum resolution a point-to-point focusing was chosen in the dispersive plane. In the non-dispersive plane a parallel-to-point focusing was chosen in order to determine the scattering angle with high precision [58]. Spec. B consists only of a clamshell dipole [58], to be able to measure at small scattering angles, see Fig. 20 right. It has a point-to-point focusing in the dispersive as well as in the non-dispersive plane. The spectrometers' main parameters are listed in Table 1. They are installed such that they can be rotated around a central axis for measuring at variable scattering angles. At their pivot the target is installed. The electrons from the accelerator interact with the target and scattered particles can be detected using the spectrometers' detector setup.

The setup of the detectors is basically the same for both spectrometers. It consists of vertical drift chambers (VDCs) for track reconstruction, plastic scintillators for triggering and a gas Čerenkov detector for particle identification, see Fig. 21. The detectors are placed in a shielding house, see Fig 19, with 40 cm thick Boron carbide loaded concrete walls covered with a 5 cm thick layer of lead on the inside [58], to prevent particles randomly hitting the detectors and causing background signals.

After exiting the magnetic field of the spectrometer the particles first traverse the VDCs to achieve the best possible position resolution. A VDC is a chamber filled with gas through which wires are spanned. Particles passing through ionize the gas and the wires detect the ejected electrons resulting in a detectable electronic signal, details may be found in Ref. [60]. VDCs are well suited for determining particle tracks with a high resolution. Multi wire proportional chambers for example have a worse resolution than VDCs [60]. Also horizontal drift chambers have a worse resolution than VDCs. And if a wire stops working the efficiency in a horizontal drift chamber is much more reduced than in a VDC [60]. There are four VDCs installed in each spectrometer in the vicinity of

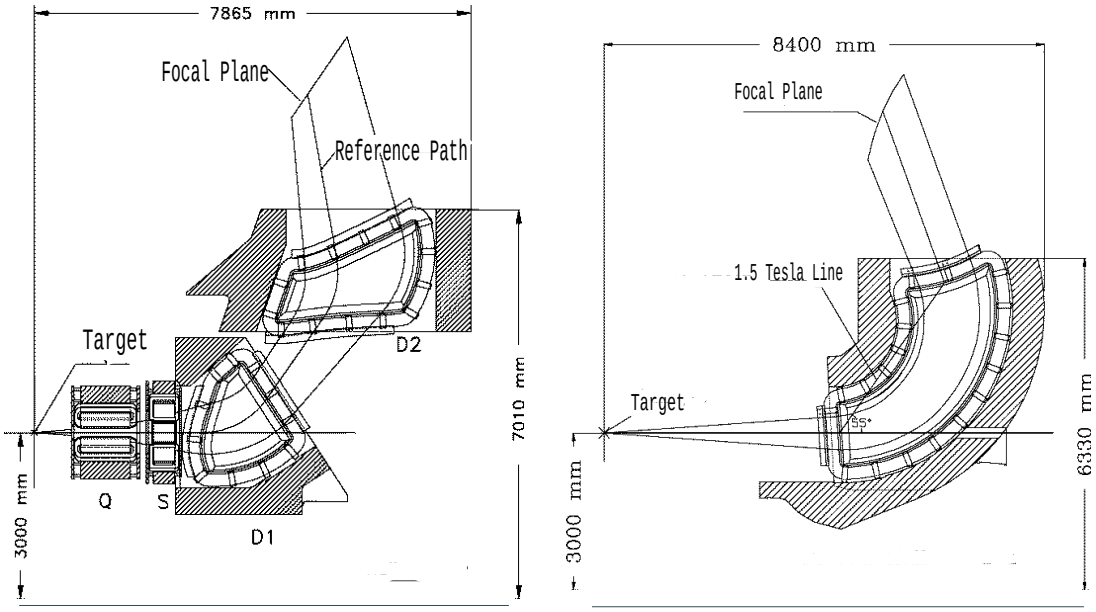

Figure 20: Left: Magnet arrangement of Spec. A. Right: Magnet arrangement of Spec. B. (source: [27])

the focal plane. Two of them are the so called X-layers and two the so called S-layers whose wires are rotated for 40° with respect to the X-layers. Ideally two VDCs would be enough to determine the two coordinates of the crossing particle as well as its angles with respect to the chambers. However, by installing two further VDCs 20 cm above the first two VDCs the angular resolution was improved by an order of magnitude [58]. The resolution is approximately 100 µm for the spatial coordinates and 1 mrad for the angular coordinates [60]. To optimally determine the coordinates of the particles the drift velocity of the ejected electrons in the gas mixture has to be known. Therefore the drift velocity was monitored during the whole experiment and the best drift velocity was determined from the data. This procedure is described in Ref. [27]. During the analysis the information of the particles crossing through the VDCs are inserted into so called transfer matrices. These matrices are polynomials and they emulate the magnetic properties of the spectrometer. The result after their application are the properties of the particle after the scattering process at the scattering vertex in the target. The momentum of the particle, its coordinate along the beam direction and the two Cartesian angles are reconstructed.
After the VDCs the particles pass through two layers of scintillators. The first layer (dE-plane) is 3 mm thick and used as a timing detector for low energy protons or deuterons [58]. The second layer (ToF-plane) is 10 mm thick and provides a fast timing signal which can be used as a reference signal for the VDCs [58]. Each layer consists of about 15 scintillator bars, which are read out by photomultiplier tubes. The scintillator bars also determine the energy deposition of the particles and hence can also be used for particle identification purposes.
A gas Čerenkov detector is passed at last. It can also be used as a trigger. In

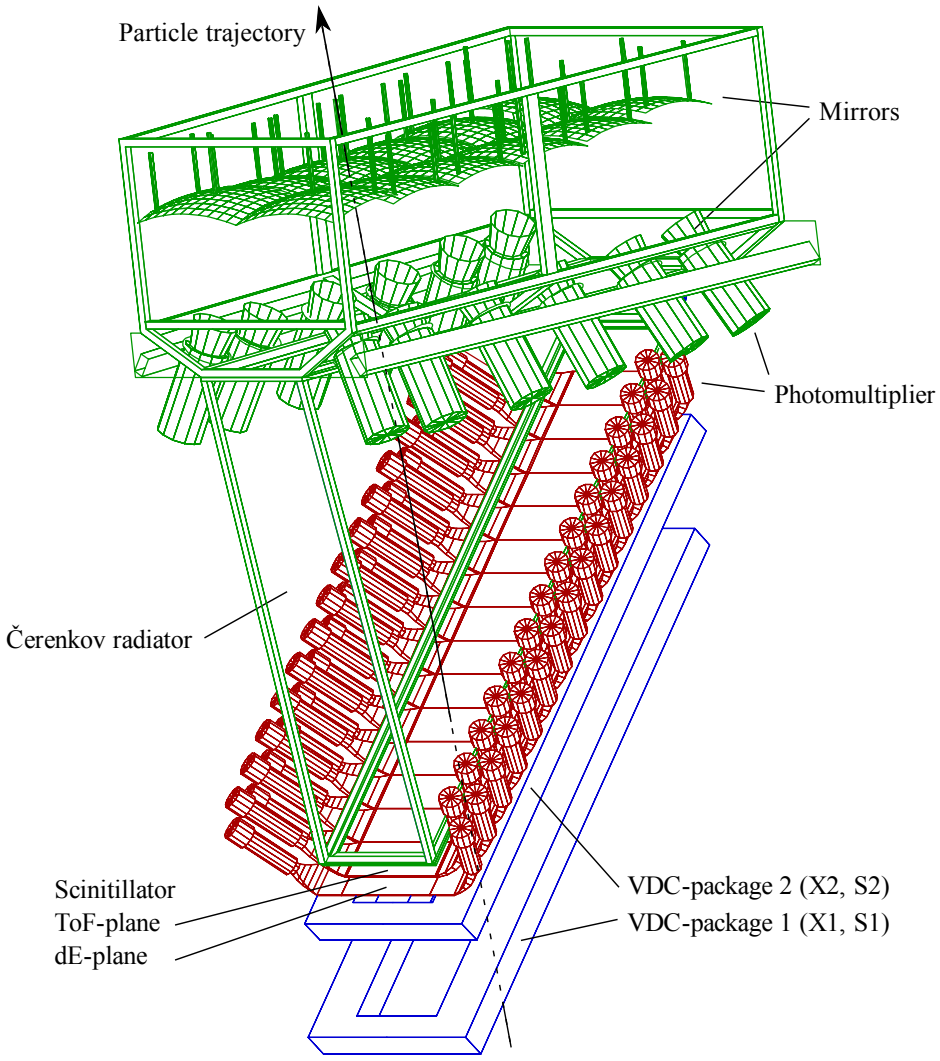

Figure 21: Model of the detector equipment. A particle first crosses the four layers of VDCs (blue) , then two layers of scintillators (red) and at last a gas Čerenkov detector (green). (source: [27])

normal operating mode it is used to distinguish electrons or positrons, depending on the polarization of the spectrometer's magnets, from heavier charged particles. The detector is filled with a gas called 1,1,1,3,3,3-Hexafluoropropane which has an index of reflection of 1.001045 [61]. When charged particles are faster than the velocity of light in this gas, Čerenkov light is emitted which is detected by photomultiplier tubes. For this kind of gas only electrons or positrons with momenta higher than 9 MeV/c can produce Čerenkov light. The next heavier charged particles, pions, need momenta higher than 2.5 GeV/c to produce Čerenkov light, which is not possible in this facility [62].
As the goal of this work is to determine the proton electric form factor, a target of protons is needed. The best target for this experiment is hydrogen. To obtain a small statistical uncertainty, it is necessary to yield a high luminosity. Therefore employing hydrogen in a liquid state is much more convenient than

gaseous hydrogen. In the A1 hall a cryogenic liquid hydrogen target has been used many times before [5, 63], see Fig. 22. The target cell has an oval form of 49.5 mm length and 11.5 mm width and is surrounded by 10.16 µm of havar foil. The hydrogen inside the target cell is circulated through a so called "Basel-Loop" by a ventilator to prevent local variations of temperature in the target, see Fig. 22 (right). Inside the target chamber a heat exchanger is installed to absorb energy from the Basel-Loop. It is connected to a secondary loop filled with hydrogen which is cooled by a Philips compressor. The hydrogen inside the target is undercooled for $1-2\,\mathrm{K}$ to ensure that little local temperature variations do not evaporate the hydrogen [64].
The scattering chamber including the target cell is under vacuum. The chamber consists of aluminium and has windows where the scattered electrons enter the spectrometers. Through these windows which are made of 120 µm thick Kapton, a polymide film, some amount of air still can diffuse into the chamber and then freeze at the target cell. To even further reduce the possible amount of these cryogenic depositions at the target cell, the windows were sealed with a 6 µm thick film of Kevlar.

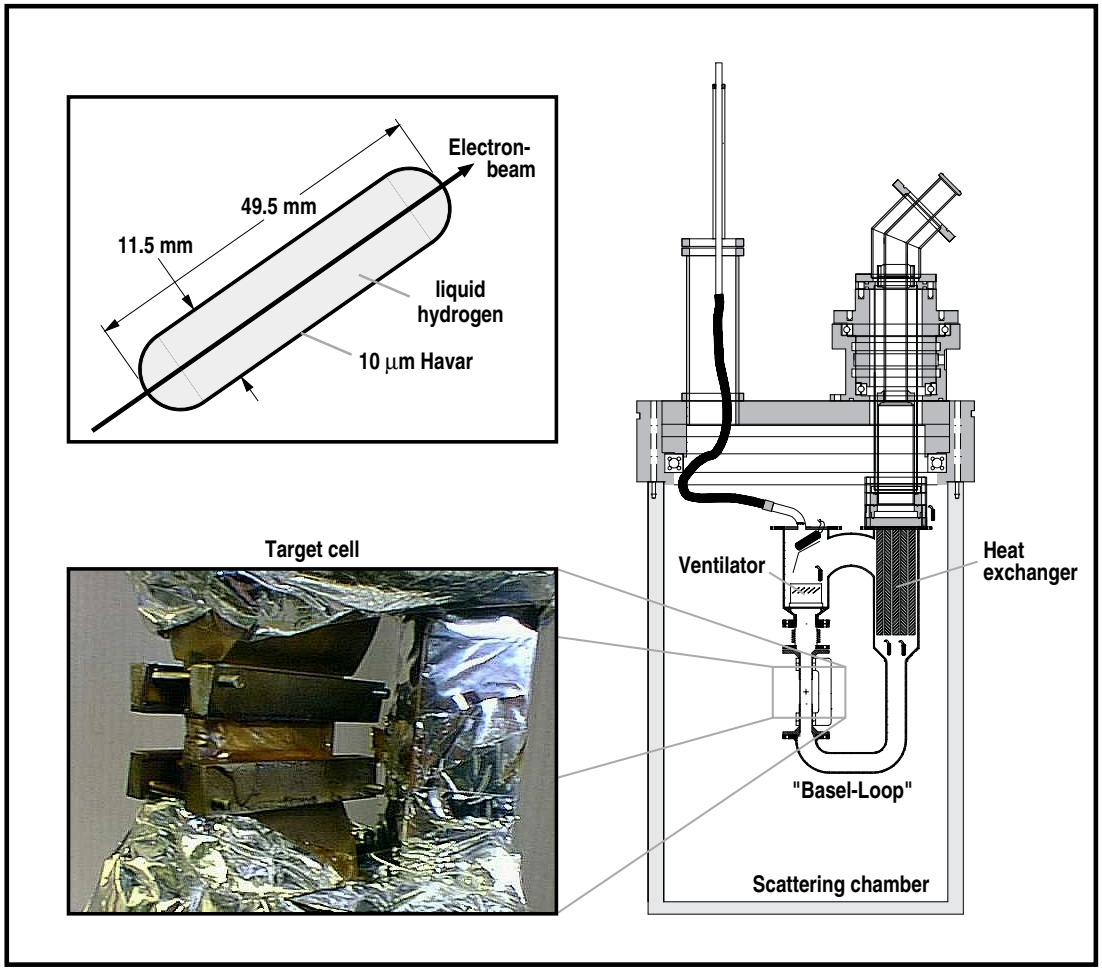

Figure 22: Top left: Geometry of the target. Bottom left: Picture of the target. Right: Model of the target chamber. (source: [27])

To monitor the position of the beam at the target a beam stabilisation modul was installed. Every three minutes it stopped the data acquisition and changed to a diagnostic mode. During this time the beam position was checked automatically and corrected to a predefined position if any change in its position would have been detected. Whilst this time also a pA-meter was read out to determine the beam current. The pA-meter works like a common ampere meter by measuring the potential drop across resistors. During the measurement the electron beam is deflected on a circular aperture, while during regular beam time the beam is guided through the circular aperture. At this stage in the accelerator the beam has an energy of about 100 keV. The aperture is well isolated and is grounded across the pA-meter which measures the current [65]. The pA-meter was used to measure currents smaller than 1 μA. For currents greater than 1 μA a Foerster probe is used instead [27]. A Foerster probe consists of a magnetically susceptible core surrounded by two coils of wire. Through one coil an alternating current is sent and this current is compared with the one in the second coil. In the absence of an external field the two currents match, but in the presence of an external field they are shifted depending on the magnetic field and such can be used to reliably determine the current of the beam in the region above 1 μA [66, 67]. Parallel to the beam monitors Spec. A was used to monitor the relative beam luminosity. For the further analysis Spec. A was rather used than the pA-meter because it was more stable and its behaviour is known better. There are also other advantages by using the relative luminosity over the beam current for the analysis. For example any possible fluctuation in the density of the liquid hydrogen or in the beam position are considered in the luminosity measurement, but if only the beam current is measured, such effects would have to be considered by external determinations.
As a supplementary beam current measuring device a SEM (secondary electron emission monitor) was installed behind the target cell, still in the scattering chamber. The monitor consisted of three aluminium foils, the beam had to pass. The beam ejects electrons from the foils [68]. The two outer foils were kept at a positive potential to absorb low energy secondary electrons. The foil in the middle was connected to an electronic integrater measuring the charge lost by the foil due to secondary electron emission [69]. The charge was converted to a frequency and then read out. However, the overall performance of the SEM was not precise enough to determine the beam current reliably, see Fig. 23. This figure shows that while the rate of the data acquisition is quite stable the rate of the SEM varies for over 20%. Consequently it could not be used to determine the beam current.

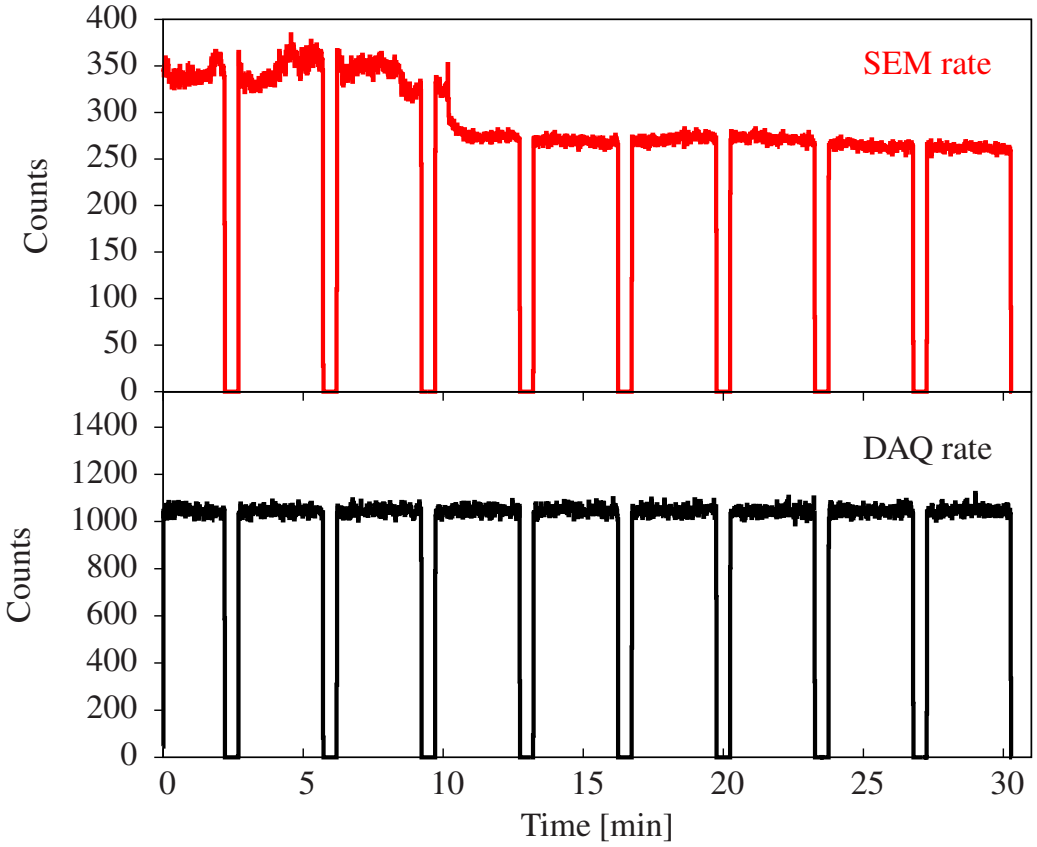

Figure 23: Comparison of the SEM rate (top) to the data acquisition rate (bottom). The rate of the SEM varies for over 20% while the rate of the data acquisition is almost stable. The short periods every three minutes during which the rate drops to 0 is the above mentioned diagnostic mode. During this time the beam position was checked and the pA-meter was read out.

The actual data taking took place from 29 July to 4 August 2013 and from 12 August to 2 September 2013. During the experiment Spec. B was used for the cross section measurement and Spec. A was used to monitor the luminosity. Spec. B was kept at the same angle with respect to the beam line at 15.207°, which is the smallest possible angle the spectrometer can be positioned to. Spec. A was placed at 60° for the first part of the experiment and at 50° for the second part of the experiment. Originally it had been planned not to move Spec. A at all, but the monitoring of the target walls and the cryogenic depositions was considered to be more convenient at 50°. By keeping the conditions of Spec. A during each energy setup constant, systematic uncertainties in the luminosity determination were drastically reduced. For Spec. B only the magnetic field was changed after each setup to measure the radiative tail of the elastic peak and such measure the cross section at smaller Q^2. In Table 2 an overview of the beam time is given. In appendix A all setups are listed. The setups were chosen such that they did overlap for one half of the acceptance with their neighbouring setups. This way it was possible to check that the setups in the overlapping regions gave consistent results. For each setup about

Beam Energy [MeV]	495.25	330.26	195.15
Duration [days]	5.7	6.6	11.2
Setups	9	12	21
Central Momentum [MeV/c]	$289.2 - 485.9$	$155.9 - 325.9$	$48.0 - 193.6$
Q^2 Range $[10^{-3} \cdot (\mathrm{GeV/c})^2]$	$6.01 - 17.06$	$1.74 - 7.64$	$0.16 - 2.69$

Table 2: Overview of the beam time. Each setup has a different central momentum. The uncertainty of the beam energy is always 0.16 MeV. In appendix A all setups are listed

10^7 events were recorded for Spec. B aiming, for a precision of one percent in the final analysis. The data were divided into 30 minutes lasting runs. To obtain this number of events for each setup about 10 runs were taken. The magnetic field of Spec. B was measured before every run. After each setup the magnetic field was changed to record the next part of the radiative tail. The radiative tail was measured at three different beam energies, such that the radiative tail of one energy measurement did overlap with the elastic peak of the next measurement. This way it was possible to justify usage of the initial state radiation method by comparing the results of the overlapping parts of the measurements.

5

CALIBRATIONS

Prior to the actual form factor determination a thorough investigation of parameters concerning the data had to be performed, thus ensuring that the later extracted values of the form factor are not biased by some external influence. For this purpose the stability of the spectrometers' magnetic fields, the performance of the detectors and the density of the hydrogen inside the target had to be examined.
In Fig. 24 the different coordinate systems used during the analysis are shown. The coordinate system called vertex (x, y, z) has its origin at the center of the target. The vertex coordinate z, which is often used, has the same direction as the incoming beam. The non-dispersive angle is the angle in the floor of the spectrometer hall, while the dispersive angle is the angle with respect to the floor plane. The focal (x, y) coordinate system is in the focal plane of each spectrometer and it is parallel to the plane of the detectors. The tracks determined with the VDCs are given in this system.

5.1 *Detector calibration*

The overall performance of all detectors needed to be checked such that inefficiencies could be corrected for in the following analysis. There the Čerenkov detector was used to make a cut accepting only electrons. Therefore it was important to know the performance of the Čerenkov detector for the whole momentum acceptance. Hence it was necessary to measure elastic electron peaks distributed over the whole momentum acceptance. For the calibration of the Čerenkov detector dedicated data was used. During these beam times the central momentum was changed only for a few per cent such that the measured elastic peak was at a different position in the momentum acceptance, ensuring that almost the whole momentum acceptance was covered with elastic peaks. To determine the Čerenkov detector's efficiency first a cut accepting the elastic peaks was made as well as a cut accepting good tracks in the VDCs requiring that in every single layer more than two wires detected a signal. To determine a track, a signal in two VDC layers would have been enough. For each of these selected events the Čerenkov detector also should have detected a signal. Then the ratio of these selected events to the events where the Čerenkov detector also did have a signal was made. This ratio determined the efficiency. The efficiency over the whole momentum acceptance for the 330 MeV beam energy setting of Spec. B is shown in Fig. 25. The results for Spec. A and the other

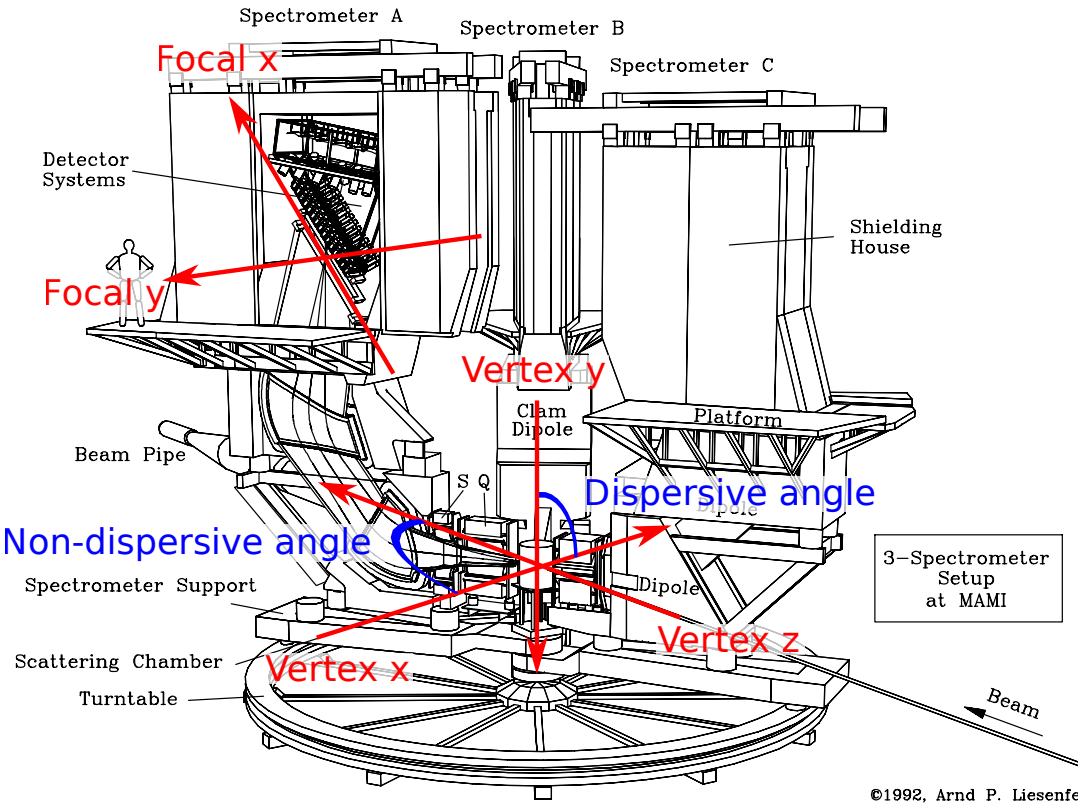

Figure 24: Model of the A1 hall: In particular, the coordinate systems used during the analysis are highlighted. (modified version of source: [70])

energies are similar. The gaps in the plot are caused by the lack of data for these momenta. The efficiency depending on the momentum of the scattered electrons is almost constant and the data were corrected applying this information. In Table 3 the Čerenkov detector's mean efficiency for the three energy settings for Spec. A and Spec. B are listed.

Beam Energy [MeV]	Efficiency Spec. A	Efficiency Spec. B
495.25	99.85%	99.69%
330.26	99.83%	99.75%
195.15	99.64%	99.20%

Table 3: Efficiency of the Čerenkov detectors for Spec. A and Spec. B depending on the beam energy. The uncertainty of the beam energy is always 0.16 MeV, the uncertainty of the efficiency is 0.12% for all setups.

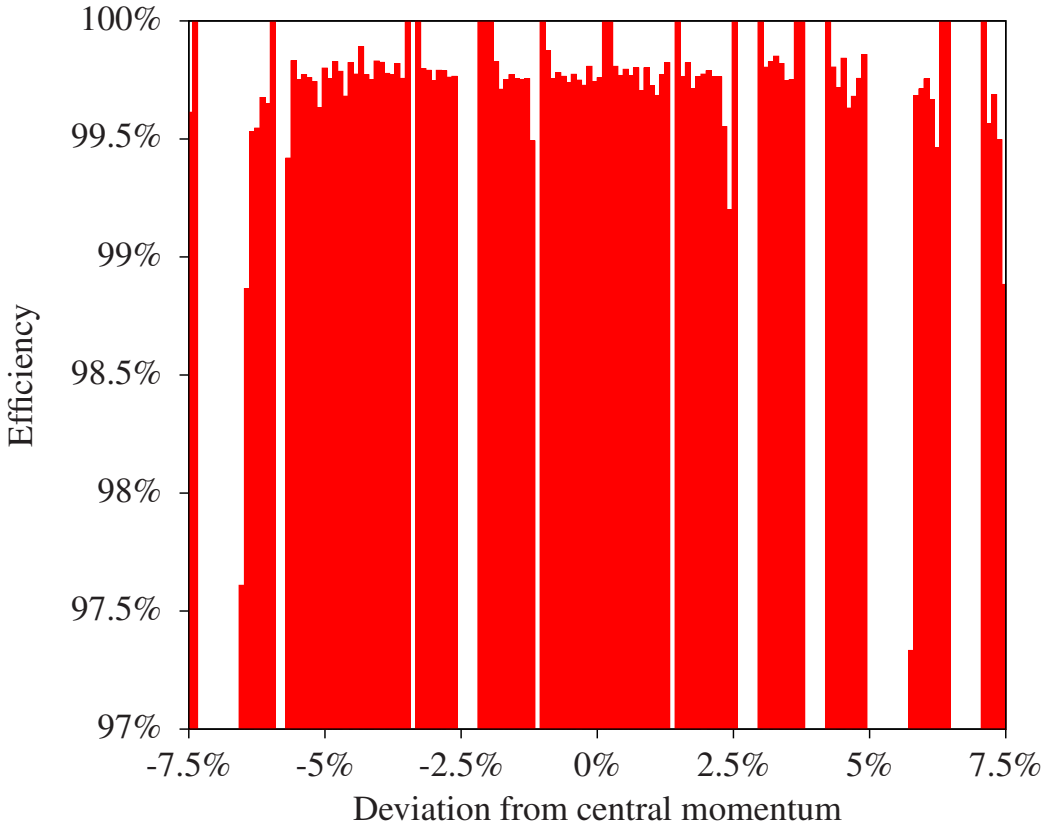

Figure 25: Efficiency of the Čerenkov detector depending on the momentum of the scattered electrons. The momentum is described as the deviation from the central momentum of Spec. B. Where the gaps in the plot are, no data was available.

The efficiency of the trigger detector was also determined. During the experiment the thick ToF scintillator layer was used for triggering, hence dedicated data had to be taken to determine its efficiency. For this purpose the thin layer called dE was used as trigger detector. In the analysis an additionally cut on the Čerenkov detector was made to be sure that the particles were really electrons and had not already been stopped by the thin dE layer. The efficiency was calculated as the ratio of these events when the ToF layer also had a signal divided by all events. In Fig. 26 the efficiency is displayed for Spec. A and Spec. B. The dips in the efficiency arise from the edges of the scintillator bars, the sharp dip at -10% for Spec. A and about $\pm 8\%$ for Spec. B are the limits of the spectrometers' acceptances. As the efficiency is not homogenous over the momentum acceptance, in the analysis the data were corrected according to the efficiency given in Fig. 26.
The VDCs' efficiency needed to be determined also, since they provide information about the momentum and the scattering angle of the particles. The efficiency of a single VDC layer is not important, relevant is the efficiency for the track reconstruction. To obtain enough information to reconstruct a particle track at least one X-layer and one S-layers has to have a signal. In a first

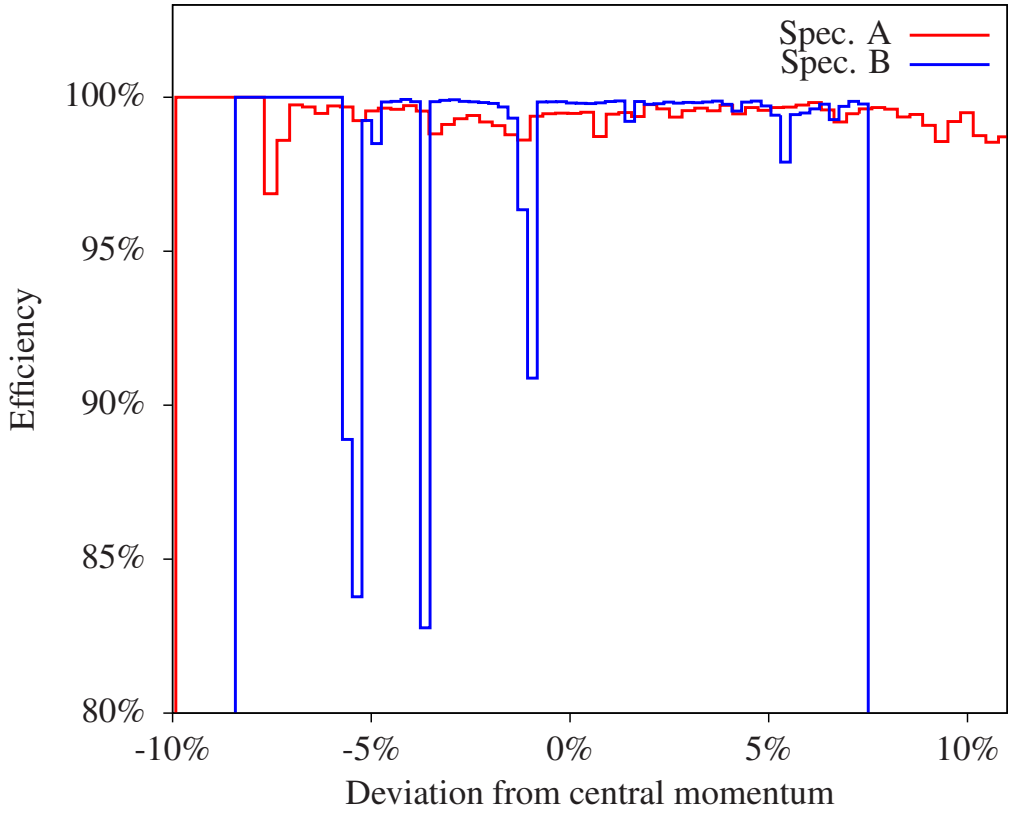

Figure 26: Efficiency of the ToF scintillator layer for Spec. A and Spec. B depending on the momentum of the scattered electrons. The momentum is described as the deviation from the central momentum of Spec. A or Spec. B.

step the efficiency of each single layer was determined and then the track efficiency with the above mentioned condition was calculated. Fig. 27 displays the efficiency of the first X-layer of Spec. B for a beam energy of 330 MeV depending on the two spatial coordinates. The efficiencies for the other energies and layers are similar. The white area is out of the acceptance and consequently the efficiency is 0. Fig. 28 shows the track efficiency for the same conditions as in Fig. 27. As the efficiency is almost constant with respect to the focal plane coordinate y, in the analysis the efficiency was corrected with respect to the focal plane coordinate x, as can be seen in Fig. 29, which is the projection of Fig. 28 on the focal plane coordinate x.

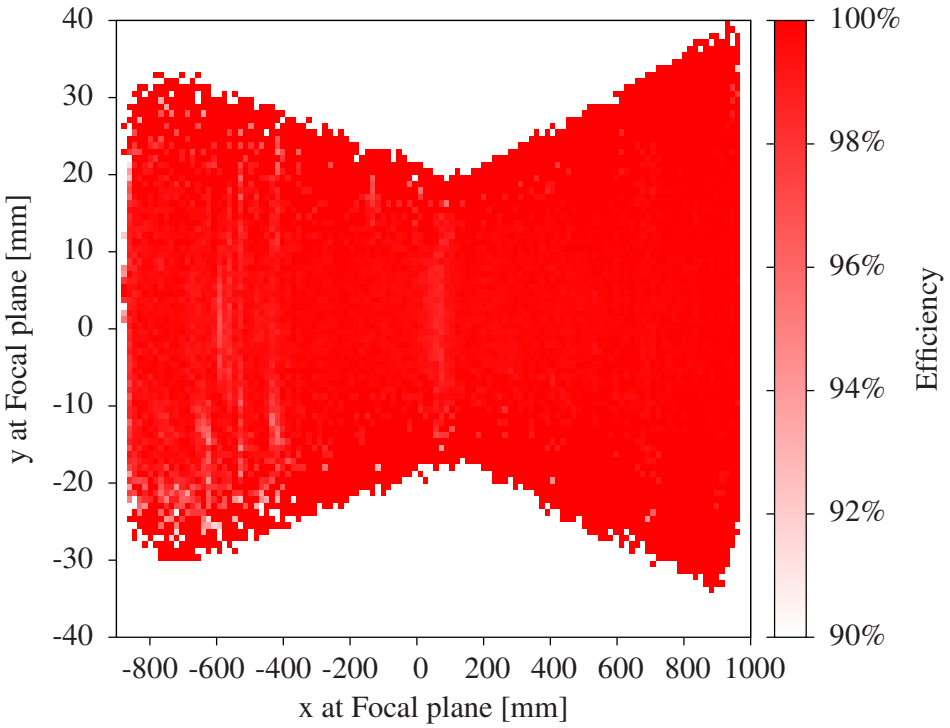

Figure 27: Efficiency of the first X-layer of Spec. B for a beam energy of 330 MeV depending on the two spatial coordinates. The white area is out of the acceptance and therefore the efficiency is 0.

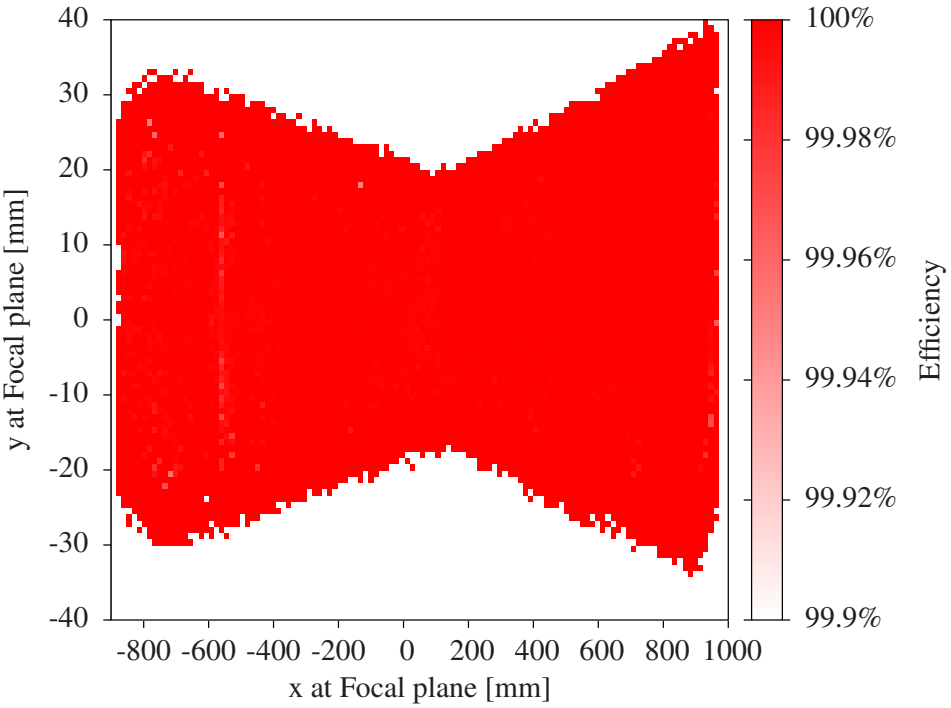

Figure 28: Track efficiency of Spec. B for the 330 MeV beam energy setting depending on the two spatial coordinates. The white area is out of the acceptance and therefore the efficiency is 0. (source: [52])

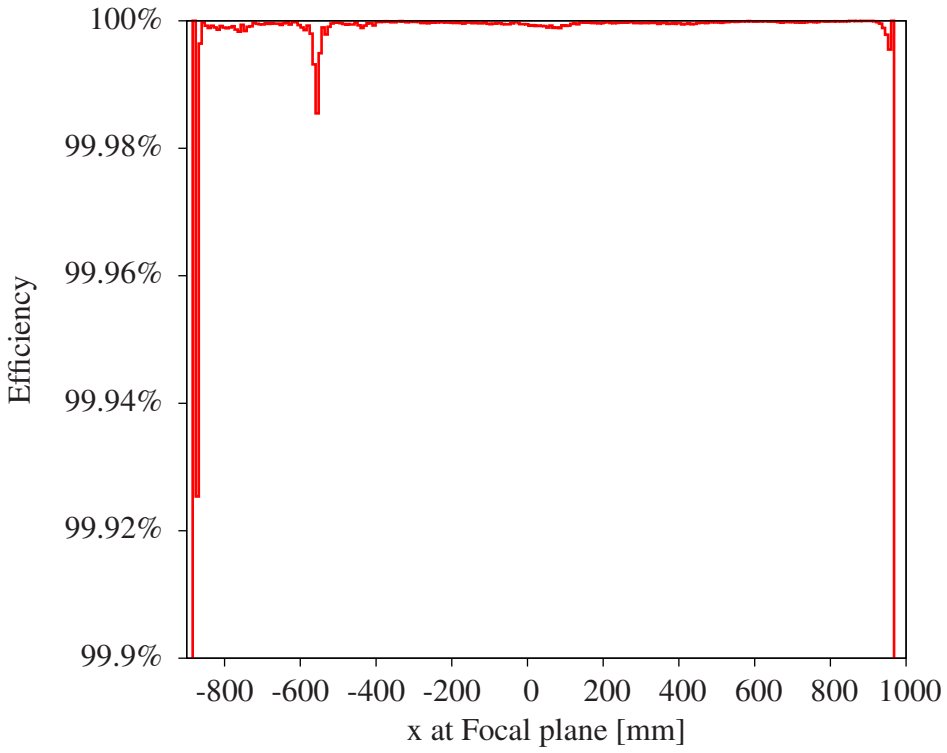

Figure 29: Track efficiency of Spec. B for the beam energy of 330 MeV depending on the x coordinate at focal plane. The acceptance in the x coordinate the at Focal plane ranges from −880 mm to 965 mm, outside of this range the efficiency is 0.

5.2 *Determination of external effects*

Besides of the detector efficiencies there were different other effects which could influence the extraction of the form factor and therefore were studied.

Precision of the spectrometer's central momentum

The knowledge of the spectrometers' magnetic field is very important. Using the track information of the VDCs the momentum of the scattered particle could be determined. But the algorithm needed the spectrometers' magnetic field as an input variable in order to work. To measure the magnetic field each spectrometer is equipped with Hall probes as well as with a NMR (Nuclear Magnetic Resonance) system [27]. The NMR system is more stable than the Hall probes, whose results are more temperature and radiation dependent. Consequently the NMR results were used as input variables for the VDCs' tracking algorithm. For every run recorded during the experiment the magnetic field of Spec. B was measured. To check the stability during the setups, all values belonging to one setup were averaged and then the relative difference of the average was evaluated for all runs depending on the NMR system, the Hall probe, and the current of the dipole, see Fig. 30 and Fig. 31. The standard deviation for these values of the NMR system is $8 \cdot 10^{-5}$ which can be regarded as the relative precision of the momentum determination. The standard deviation for these values of the Hall probe is $2 \cdot 10^{-4}$ which is larger than the one for the NMR system as expected. The standard deviation for these values of the current measurement is $9 \cdot 10^{-4}$. There is no apparent correlation between the NMR system and the other two, indicating that the variations arise from the uncertainties of the devices.

Angle of the spectrometer

In addition to these examinations also the accuracy of Spec. B's angular position was checked. To measure the angle, each spectrometer is equipped with a readout system. This system was reviewed by measuring the scattering angle of the spectrometer with a theodolite and comparing it with the value of the readout system. Thereby a small deviation was detected, see Fig. 32. A linear function was fitted to describe this deviation:

$$\text{Readout Angle} - \text{Measured Angle} = -0.034 \cdot \text{Readout Angle} - 0.00056^\circ \,.$$

Using this result the read out angle of the spectrometer system of 15.25° was corrected to the above mentioned 15.207°.

Density of liquid hydrogen

A parameter which had to be monitored during the data taking was the density of the liquid hydrogen inside the target cell. During the experiment the

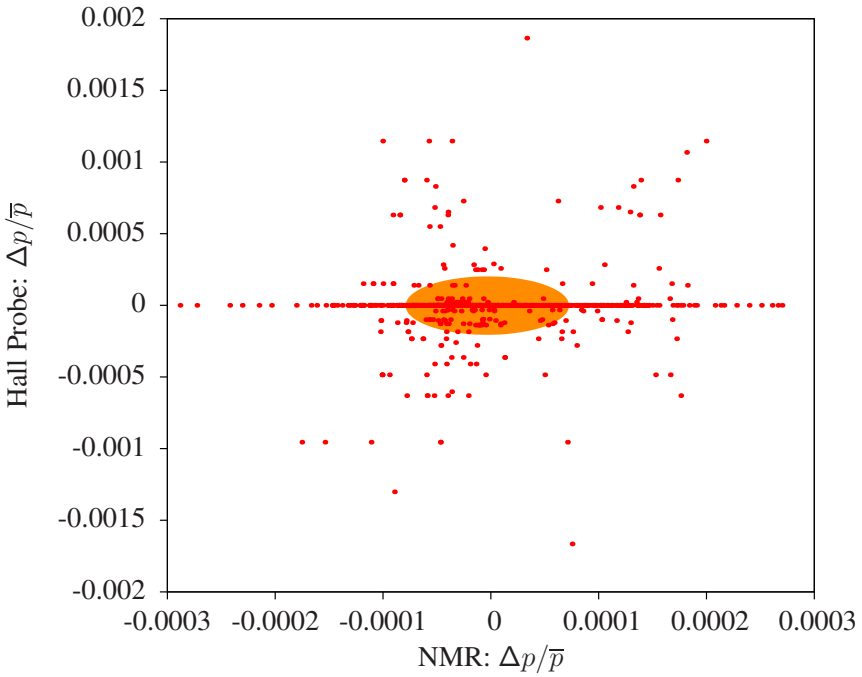

Figure 30: Relative deviations of the NMR readouts from the average versus the relative deviations of the Hall probe readouts from the average. The orange ellipse displays the 1σ confidence ellipse.

temperature and the pressure of the hydrogen inside the target were measured. With these values the density of the hydrogen could be determined. But first the sensors themselves were calibrated. For that purpose the theoretical saturated vapour trend [71] was compared to the measured values when warming up the undercooled hydrogen, see Fig. 33. The measured values of the pressure sensor were compared to a local weather station after the beam time, when the target cell was ventilated. It was detected that the pressure sensor had an offset of 21 mbar. The data were corrected for this value but yet they did not match the theoretical trend. Thus the temperature data were also corrected for 0.06 K to match the theoretical trend, the result is the red curve in Fig. 33.
The density of the undercooled hydrogen was calculated with the Hankinson-Thomson model [72]. The calculated density of the hydrogen inside the target depending on the time after the beginning of the experiment is shown in Fig. 34. During the time without data the experiment was halted. There was practically no density fluctuation during the entire experiment, the fluctuations which can be seen are basically only due to the resolution of the sensors.

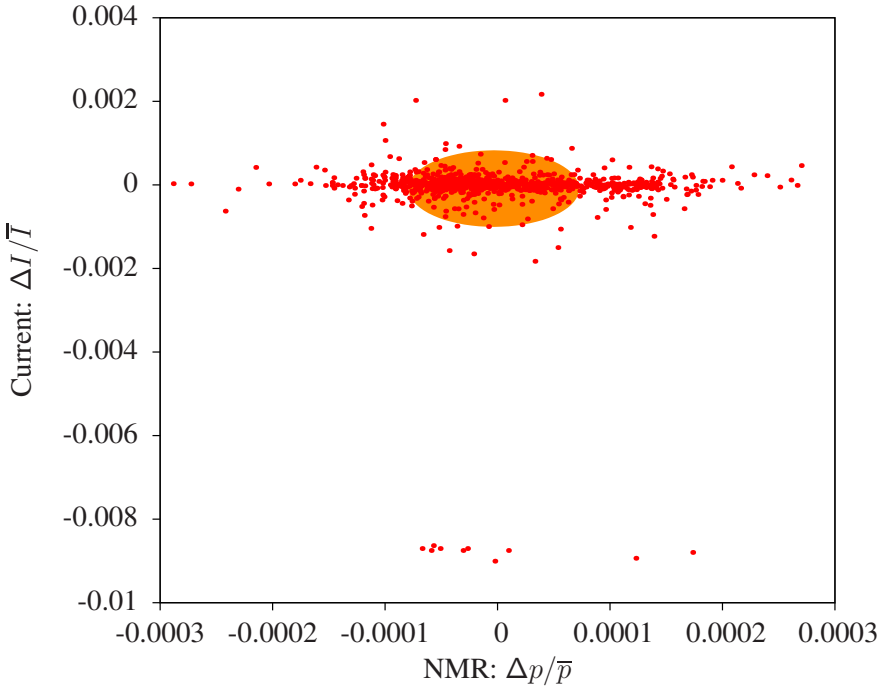

Figure 31: Relative deviations of the NMR readouts from the average versus the relative deviations of the current readouts from the average. The orange ellipse displays the 1σ confidence ellipse.

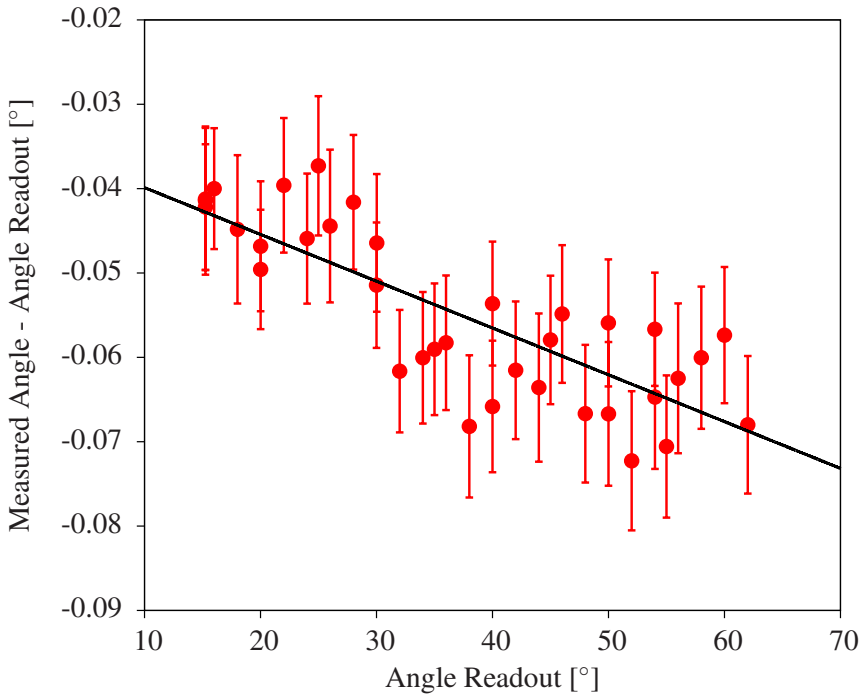

Figure 32: Deviation of the angle readout system of Spec. B from the measurement of the angle with a theodolite. In black a linear fit to the data has been added.

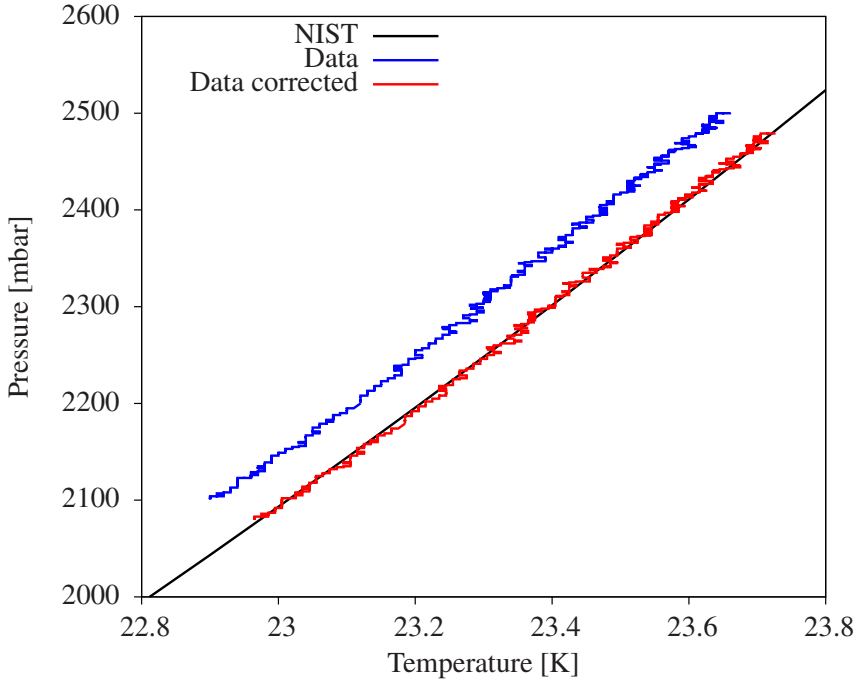

Figure 33: The black curve shows the data from the National Institute of Standards and Technology (NIST) for saturated vapour of hydrogen [71]. The blue curve displays the measured data and the red curved shows the data after the calibration of the sensors.

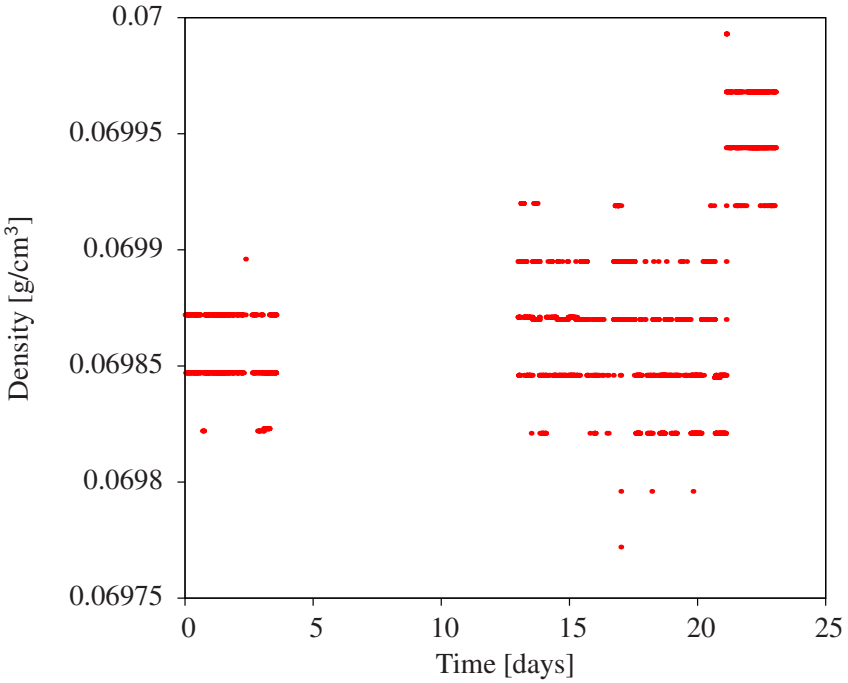

Figure 34: Calculated density of hydrogen inside the target cell depending on the time after the beginning of the experiment. During the time without data points the experiment was halted. The fluctuations are basically only due to the resolution of the sensors.

6

DATA ANALYSIS

In the analysis the acquired data were compared to a simulation to extract the proton electric form factor. Also background events had to be considered and were simulated. For the analysis a software package called `Cola++` was used [27]. `Cola++` reads the raw data from the experiment and determines the tracks of the scattered electrons at the VDCs. Then it applies the transfer matrices to calculate the scattering angle, momentum and scattering vertex of the electron with respect to the beam axis. A second program, `Lumi++`, was used to determine parameters related to the luminosity. For this experiment `Lumi++` was used only to determine the dead time of the spectrometers, while Spec. A was used to determine the relative integrated luminosity for every data run. A third program called `Simul++`, described in the next section, simulated the cross sections and acceptances for the interactions of electrons with hydrogen, havar, nitrogen and oxygen among others.

6.1 *Simulation*

The purpose of a simulation is to mimic the behaviour of real experiments. Therefore it needs algorithms describing reality as good as possible. The simulation for this experiment did not only calculate the cross section for an electron scattering from a proton in the Born approximation, but it exactly calculated the Bethe-Heitler and Born diagrams together with higher order corrections, which were added as effective corrections to the cross section, see chapter 3.1. It also modelled the energy losses of electrons traversing the target cell and spectrometer. The acceptance of the real spectrometer was also included into the simulation. In the simulation the incoming electron beam was first generated. Its properties, the energy and momentum, were known from the accelerator data. Then a scattering vertex in the interior of the target cell was generated. For this a model of the target cell was implemented, see also appendix B. For this model the geometry of the real cell was employed. It consisted of a havar foil confining the hydrogen in the inside. It was also possible to add a layer of cryogenic depositions on top of the havar foil. After the generation of the scattering point the electron was corrected for external Bremsstrahlung [73] and for the multiple scattering effects in the region from the entrance point to the target cell to the scattering point. Next the cross section for the scattering process:

$$e^- p \to e^{-'} p' \gamma$$

was calculated. In the simulation the four-vectors of all particles were known. The amplitudes in equation 42 were evaluated explicitly. Detailed information about this calculation may be found in Ref. [27].
The calculation of the cross section for hydrogen was done in several steps. After the generation of the scattering angles of the scattered electron, see appendix C, the energy of the scattered electron was generated with an approximate angular distribution given by the expression:

$$E' = E'_{el} \cdot r^{\frac{1}{t}}, \; t = \frac{2 \cdot \alpha}{\pi} \left(\ln \left(\frac{Q^2}{m^2} \right) - 1 \right), \tag{47}$$

where r is a random number uniformly distributed over the interval $r \in [0, 1]$. In the next step the angle ϕ between the emitted photon and the electron emitting it was generated with the following expression [27]:

$$\begin{aligned} \phi(r) &= F^{-1}(r) \\ F(\phi) &= \frac{1}{-4 - 2\frac{E_e}{|\vec{k}_e|} \cdot \ln\left(\left(\frac{E_e}{\vec{k}_e} - 1 \right) / \left(\frac{E_e}{\vec{k}_e} + 1 \right) \right)} \\ &\quad \times \left(\frac{1 - \left(\frac{E_e}{|\vec{k}_e|} \right)^2}{\frac{E_e}{|\vec{k}_e|} - \cos\phi} - \cos\phi - 2\frac{E_e}{\left|\vec{k}_e\right|} \ln\left(\frac{\frac{E_e}{|\vec{k}_e|} - \cos\phi}{\frac{E_e}{|\vec{k}_e|} + 1} \right) - 2 + \frac{E_e}{\left|\vec{k}_e\right|} \right). \end{aligned} \tag{48}$$

The inverse of the function $F(r)$ was calculated with the bisection method which could be applied since F is a monotone function [74]. Then the cross section for the event was calculated applying equations 42 and 16. The distributions used for generating the energy of the scattered electron and the photon angle approximate the correct cross section and such the uncertainty of the calculated events was smaller than with a uniform distribution. This approach is called importance sampling [74]. In the end the weight for the generation of the scattered electron energy and the photon angle were multiplied with the cross section and the weight of the generation of the energy of the scattered electron was taken out [27]. Applying this approach for the generation of the scattered electron energy also had a second advantage. In the limit of the energy of the emitted photon becoming 0 the cross section is divergent. Therefore there was a limit in the simulation for the smallest photon energy. This limit should be as small as possible, because events, where the energy of the emitted photon is very small, have a very large cross section. By using the above mentioned distribution for the generation of the scattered electron energy this limit could be as small as 10^{-10} GeV due to programming knacks, instead of 10^{-5} GeV when using a uniform distribution. Hence, the cross section calculation was

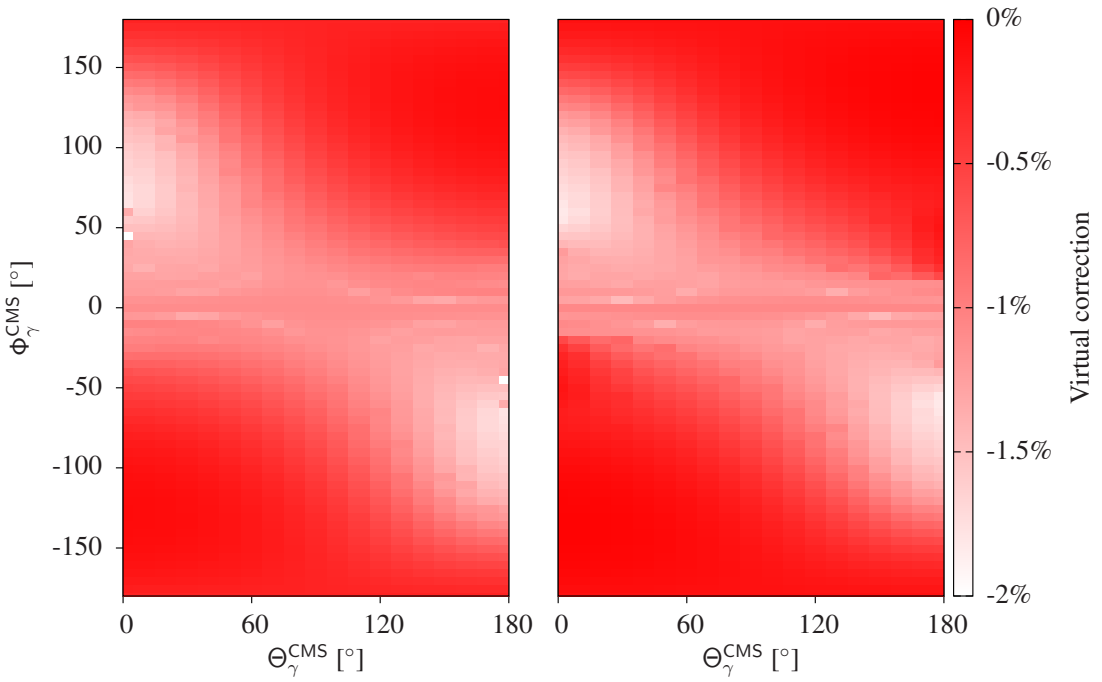

Figure 35: Contribution of the virtual corrections to the cross section for the setting ISR_330_03 (left) and ISR_330_04 (right) depending on the polar and azimuthal angle of the emitted photon, given in the center of mass system.

more precise. After the scattering process the Bremsstrahlung and multiple scattering of the scattered electron from the scattering point to the entrance of the spectrometer were calculated. For a sketch of the electron's path see appendix B. At this point also the effective radiative corrections described in chapter 3.1 were employed. The calculation of the effective virtual corrections described by the diagrams shown in Fig. 15 was computational very costly, therefore a stand alone simulation was used to calculate these corrections once for each momentum setting. This could be done because the relative difference for neighbouring momentum settings was small. As an example the correction for two neighbouring settings is shown in Fig. 35. The correction depended on the scattering angle of the emitted photon which was known in the simulation. The overall effect of the different corrections on the cross section for the 330 MeV beam energy setting is displayed in Fig. 36. There can be seen that especially the next order soft photon correction was very important for the simulation. The energy loss contribution of the electrons in the target cell and the spectrometer's entrance windows was crucial to the simulation of the calculated energy of the scattered electrons, as the position of the elastic peak and consequently the radiative tail would have been shifted without this correction. The contributions of the external Bremsstrahlung, the proton correction and the virtual correction were smaller but still of vital importance as this experiment aimed for a precision better than one per cent.
The results of these calculations were the four-vectors of the scattered electron and emitted photon and the weight for the event determined during the cross

section calculation. These results could then be used for further analysis where cuts were applied on certain parameters.

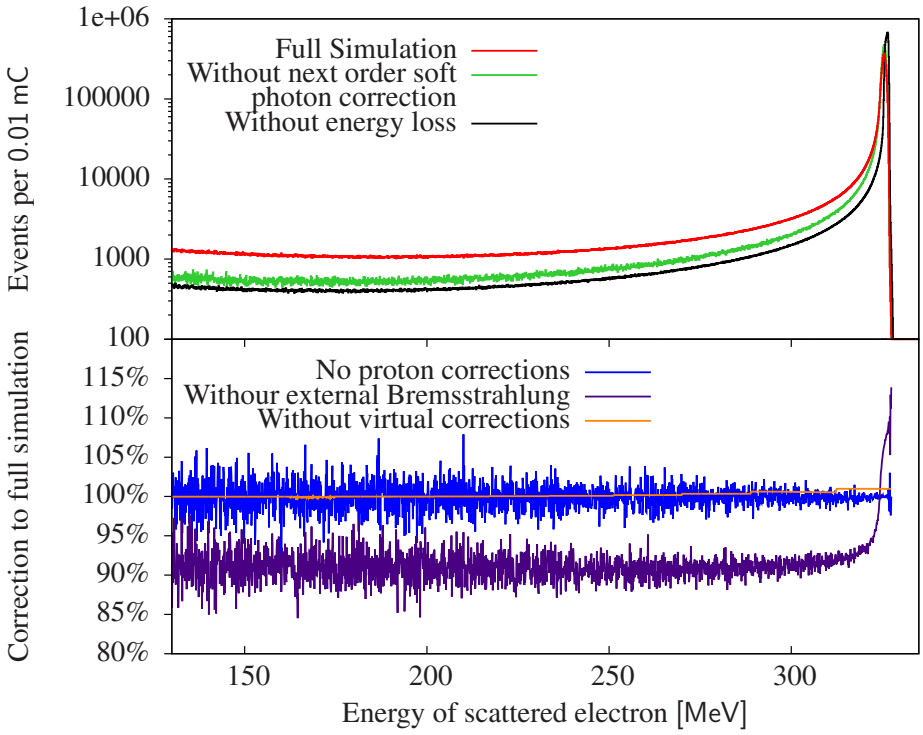

Figure 36: Contribution of different corrections to the full cross section calculation for the 330 MeV setting depending on the energy of the scattered electron.
Top: In red the complete simulation is plotted, in green the complete simulation without the contribution of the next order soft photon correction is shown and in black the complete simulation without the contribution of the next order photon correction and external Bremsstrahlung and the energy loss of the electron during its way through the target cell into the spectrometer is presented.
Bottom: The ratio between the simulation without the proton corrections and the complete simulation is plotted in blue, in indigo the ratio between the simulation without the effects of the external Bremsstrahlung and the complete simulation is shown and in orange the ratio between the simulation without the virtual corrections and the complete simulation is presented.

Background simulation

To complete the analysis of the experiment, simulations for electron scattering from nitrogen, oxygen and havar targets were needed because processes on these nuclei contributed background to the experimental data. Havar is an alloy of 42.5% cobalt, 20% chromium, 17.86% iron, 13% nickel, 2.8% tungsten, 1.6% molybdenum, 0.2% carbon and 0.04% beryllium [75]. To model the cross section for these nuclei the Mott cross section, see equation 7, multiplied by an

appropriate form factor was used [15]. These form factors were approximated by the so called Helm's model [76]. Within this model is the charge distribution modelled as a convolution of a homogeneously charged sphere with radius R and a Gaussian distribution of variance σ:

$$\rho_H(r, R, \sigma) = \rho_{h.s.}(r; R) * \rho_G(r; \sigma) \ . \tag{49}$$

The form factor is given by the product of the Fourier transforms of $\rho_{h.s.}$ and ρ_G:

$$\begin{aligned} F_H(q) &= F_{h.s.}(q) \cdot F_G(q) \\ &= \frac{3}{(qR)^2}\left(\frac{\sin(qR)}{qR} - \cos(qR)\right) \cdot \exp\left(-0.5\,(q\sigma)^2\right) \ . \end{aligned} \tag{50}$$

The proper values for R and σ for the considered elements are given in Ref. [76]. For the nitrogen form factor another model is used, which is described in Ref. [77]. There the form factor is given as follows:

$$\begin{aligned} F^2\left(q^2, \theta\right) &= F_L^2\left(q^2\right) + \left(\frac{1}{2} + \tan^2\left(\frac{\theta}{2}\right)\right) F_T^2\left(q^2\right) \ , \\ F_T^2\left(q^2\right) &= \frac{2}{3}\frac{J+1}{J}\frac{x}{a^2M^2}\left(\frac{\mu}{Z}\right)^2 \cdot \left(1 - \frac{2x}{3} + \lambda\frac{2x}{3}\right)^2 \cdot \exp\left(-2\,(x+d)\right) \ , \\ F_L^2\left(q^2\right) &= \left(\left(1 - \frac{2}{3}\frac{Z-2}{Z}x\right) \cdot \exp\left(-x-d\right)\right)^2 \\ &\quad + \frac{q^4}{180}\frac{(J+1)\,(2J+3)}{J\,(2J-1)}\left(\frac{Q}{Z}\right)^2 \cdot \exp\left(-2x-2d\right) \ , \\ x = \frac{1}{4}q^2a^2; \ d &= \frac{1}{4}q^2 \cdot \left(a_p^2 - \frac{a^2}{A}\right) \ . \end{aligned} \tag{51}$$

J is the angular momentum of the ground state of nitrogen, therefore $J = 1$. $A = 14$ is the atomic number of nitrogen and $Z = 7$ its charge number. a_p is 0.63 fm according to Ref. [77]. $a = 1.75$, $\lambda = 0.44$ and $\mu = 30$ were determined by fits to the data taken in Ref. [76]. In Fig. 37 a comparison between nitrogen data and the model given with equation 51 is shown [76].

The simulation for nitrogen, oxygen and havar was much more simple than the one for hydrogen. The radiative corrections were considered in the peaking approximation. This was not problematic during the analysis because with the data from the target walls the simulation was corrected. This was possible since in the vertex plots the peaks of the walls could clearly be identified, while the underlying contribution of hydrogen was modelled exactly with the simulation, see Fig. 49. Therefore any discrepancy between data and simulation in the region where the peaks from the walls were, was assumed to be due to the approximated form factor model of the simulation for nitrogen, oxygen and havar.

The generation of events was done such that they appeared only at the location

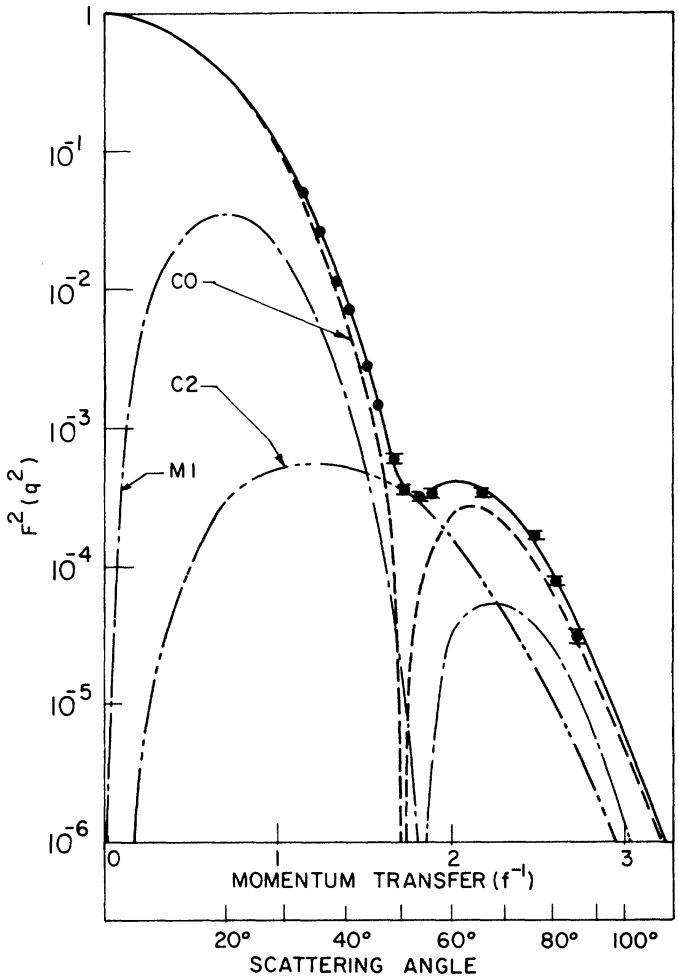

Figure 37: Fit to elastic nitrogen data at 400 MeV beam energy. M1 corresponds to F_T^2 in equation 51 and the sum of C0 and C2 corresponds to F_L^2 in equation 51. The solid line is the total curve of the three terms. (source: [76])

of the foil or the cryogenic depositions. The calculation of the energy loss as the electron passes through the target cell into the spectrometer is explained in appendix B.

Pion simulation

When measuring the radiative tail it is also possible to detect electrons with low momentum which do not originate from elastic scattering processes. As for this experiment the beam energy was always high enough to produce pions, some events in the radiative tail originated from the pion production processes which contributed to the background in the data. To consider these contributions the MAID model which was already included in the `Simul++` software was used [78]. With this simulation the two possible processes:

$$e^- + p \rightarrow e^{'-} + n + \pi^+,$$
$$e^- + p \rightarrow e^{'-} + p^{'} + \pi^0,$$

from which the spectrometer could detect a scattered electron were modelled. The electrons originating from pion production contributed up 14% of all events. But the contribution is only important in the radiative tail, if the electron lost enough energy to produce a pion, see Fig. 50 (bottom).

6.2 *Data preparation*

In the first step the integrated luminosity needed to be determined. Since the data contained also background contributions, they had to be cut away in the analysis or to be considered in the simulation. Electrons scattered off the target cell frame were also recorded and needed to be removed. Also events due to backscattering of elastically scattered electrons off the entrance flange of Spec. B were recorded and needed to be subtracted. There were contributions due to the target walls and the cryogenic depositions which condensed at the target walls during the experiment. These events were simulated and such taken into account.

Integrated luminosity

In the experiment Spec. A was used as a relative luminosity monitor. During each energy setting its conditions were not changed at all, such that no systematic uncertainty during the luminosity determination would occur. Its conditions were set such that it detected the elastic peak for each momentum setup. Hence the events it counted during each data run were directly related to the integrated luminosity for the run. During the analysis a cut on the vertex position was made to remove contributions of the cryogenic depositions which are explained below. Also a cut on the energy of the scattered electron was made to accept only elastically scattered electrons. For the same reason a cut on the Čerenkov signal was made. The dead time of the applied detector system was also corrected for. For each energy setting one run was selected to serve as a relative normalisation for the integrated luminosity. The obtained integrated relative luminosity was then used for the further analysis with Spec. B as an input parameter for the simulation. As this was only a relative luminosity determination, for each energy setting one global normalisation factor still remained undetermined, see chapter 7.

Target frame

In the experiment some of the scattered electrons scattered one more time off the frame of the target back into the acceptance of Spec. B. This had not been expected before the experiment. The target frame can be seen in Fig. 22. The frame consisted of four metal bars visible in the middle of the picture. Already during the experiment it was learned that the target position was set too high, such that some scattered electrons hit the target frame. The effect can be seen in Fig. 38 and 39. For the explanation of the phenomenon see appendix D.

The vertex z axis is in the direction of the incoming electron beam, where the 0 position is at the center of the target chamber. Most of the scattered electrons coming from the liquid hydrogen scattered elastically. If they scattered again off the target frame, they lost some energy and were not recorded in the elastic setup because they were not in the momentum acceptance of the spectrometer any more. This effect caused the deficiency of events in the upper left corner in Fig. 38 which shows the results for the elastic 330 MeV beam energy setting. However, these lost events reappeared in the acceptance for settings in the radiative tail which can be seen in Fig. 39. It shows data for the second setup of the 330 MeV beam energy setting. The abundance of events in the upper left corner is due to these electrons. As there was no possibility to verify which events exactly did originate from the target frame, a general cut rejecting events with a dispersive angle greater than $-1°$ for the whole analysis was implemented. The abundance of events at the left and right side at vertex z ± 25 mm was due to the target walls and was expected.

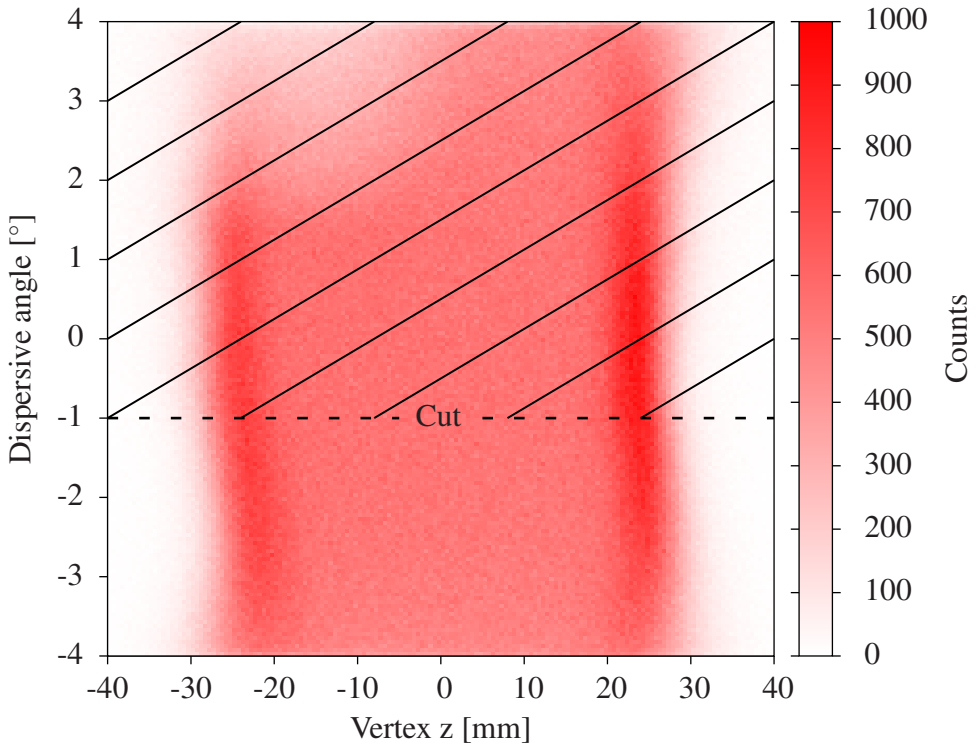

Figure 38: Effect of the target frame on the hydrogen data for the setting ISR_330_00. The deficiency of events in the upper left corner (positive dispersive angles) is due to the target frame which represents an obstacle for events scattering in forward direction. The vertex z axis is in the direction of the incoming electron beam (see Fig. 60), where the 0 position is at the center of the target chamber. Due to this problem a cut rejecting events with a dispersive angle greater than $-1°$ was made.

To estimate the remaining contribution of the target frame despite the above described cut on the dispersive angle, data with two different cuts on the vertex z coordinate were compared. The first cut was the one used during the

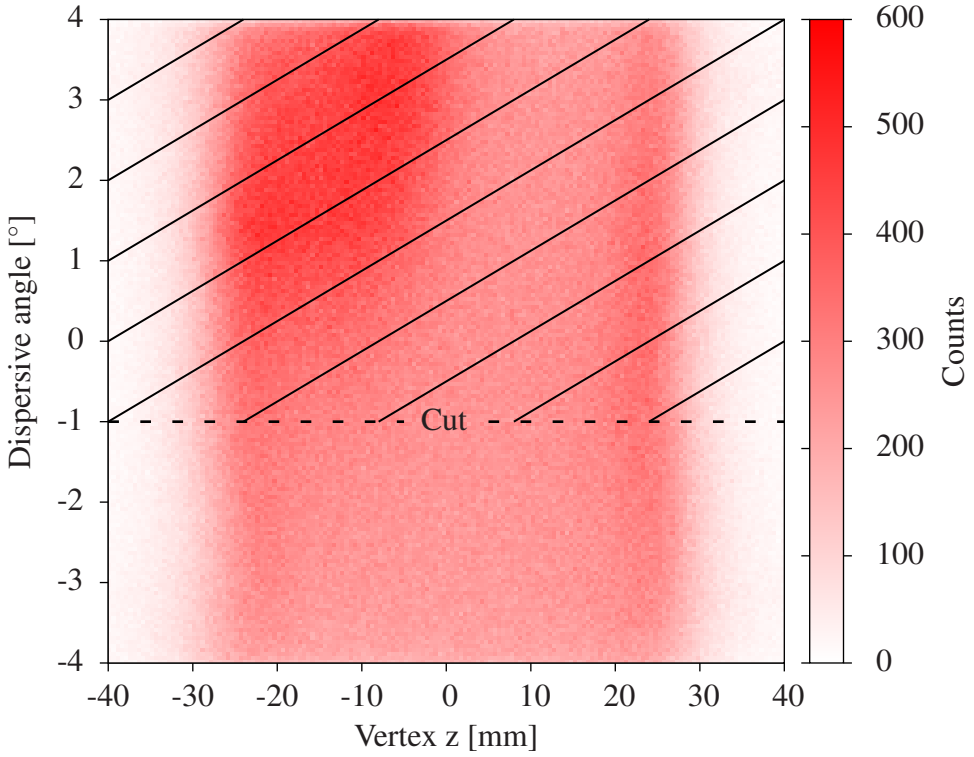

Figure 39: Effect of the target frame on the hydrogen data for the setting ISR_330_02. The abundance of events in the upper left corner is due to electrons scattered from the target frame back into the acceptance of the spectrometer. Due to this problem a cut rejecting events with a dispersive angle greater than $-1°$ was made.

final analysis accepting events ranging from 1.5 mm to 11.5 mm with respect to the vertex coordinate z. The second cut was more restrictive and accepted events ranging from 6.5 mm to 11.5 mm with respect to the vertex coordinate z. Then the results of the two data sets were compared for every momentum setup. The events in the restrictive cut were normalised by a factor of 2 to the cut used during the analysis by comparing the number of bins with respect to the vertex coordinate z. The comparison of the two cuts is shown in Fig. 40. To estimate the contribution of events originating from the target frame, the ratio of the cut used during the analysis and the more restrictive cut was calculated, see Fig. 41. In this plot the result of this ratio is shown for all momentum setups. These results were used to correct the data during the further analysis. The background coming from the target frame, together with the accompanying cuts represents a serious restriction for this experiment. Because of it more than one half ot the statistics was lost and introduced a significant source of systematic uncertainty. For future experiments of this kind an improvement would be to construct a new target cell where the target frames would be further apart. On the other hand the application of a windowless and frameless gas jet target would solve this problem once and for all.

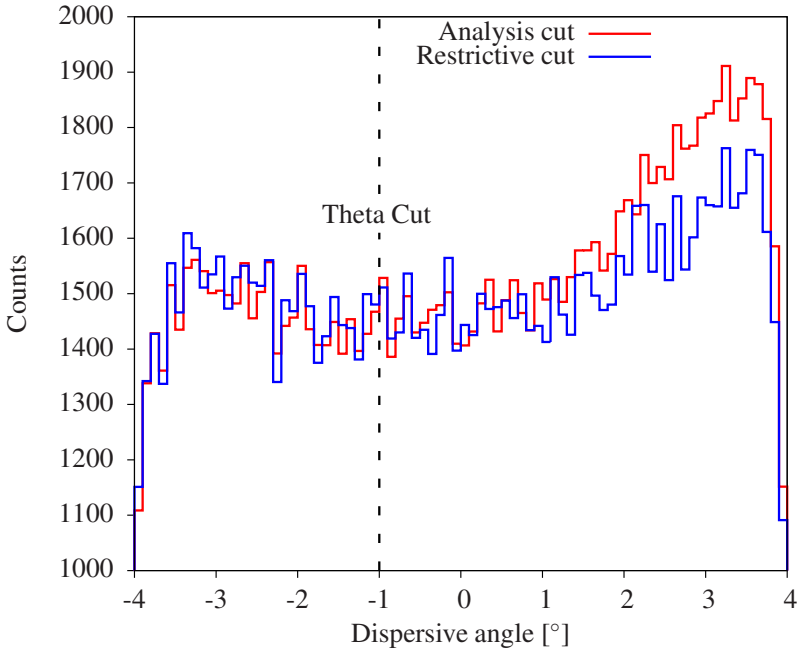

Figure 40: Estimation of the remaining target frame contribution for the setting ISR_330_04. In red the data with the regular cut accepting events ranging from 1.5 mm to 11.5 mm with respect to vertex z are plotted. In blue the data with a more restrictive cut accepting events ranging from 6.5 mm to 11.5 mm with respect to vertex z and scaled by a factor of 2 are plotted. The ratio of the two sets in the region, where the dispersive angle is smaller than $-1°$, was used to estimate the remaining target frame contribution.

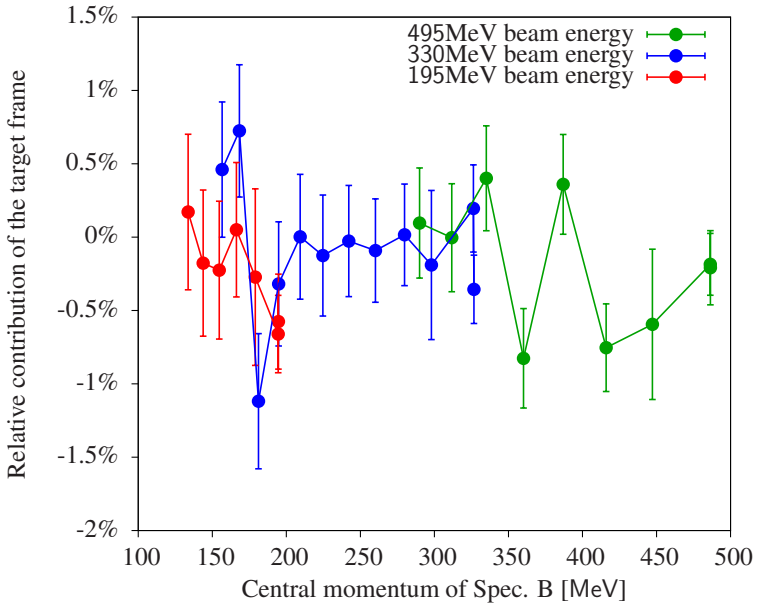

Figure 41: Relative contribution of events originating from the target frame after the global cut rejecting events with a dispersive angle greater than $-1°$. The data are represented by the points, the lines are just for a better visualisation.

Cryogenic depositions

Besides the elastic peaks of hydrogen and elements inside the target walls the data of Spec. A contained also peaks belonging to electrons which scattered from nitrogen or oxygen. These contributions were expected because the residual air still being in the target chamber predominantly froze at the cold target walls. For the analysis it was important to determine the amount of this cryogenic depositions in order to properly include it in the simulation. During the 330 MeV and 195 MeV settings the elastic peaks of the cryogenic depositions were measured with Spec. A such that for each momentum setup of Spec. B the amount of cryogenic depositions could be analysed. This was possible as the conditions of Spec. A were constant during any setting, as described in chapter 4. In Fig. 42 an example of this analysis for the 195 MeV beam energy setting is shown. In black the data are plotted and in red the simulation for the havar foil and the resulting amount of cryogenic depositions. The analysis was done such that the integral of the data and the simulation were matched. Therefore the amount of cryogenic depositions in the simulation was adjusted. The distribution of the data and simulation do not match perfectly which is because there was no exact model for the cross section calculation available and the models described in chapter 6.1 were used as the best approximation. The peaks in this plot belong to cryogenic depositions, consisting mostly of nitrogen, and havar target foils. For the 495 MeV beam energy setting the elastic peak of nitrogen was not in the acceptance of Spec. A, hence the data acquired with Spec. B had to be used to determine the amount of the cryogenic depositions for this energy setting. Since only in the first and last momentum setup of this energy setting the elastic nitrogen peak was in the acceptance of Spec. B, the amount of cryogenic depositions in the setups in between was determined by applying a linear fit to the two obtained values.
The resulting amount of cryogenic depositions, given as the area density, for all three energy setups is shown in Fig. 43. Each point represents one momentum setup of Spec. B and these values were added to the analysis especially for the simulation of cryogenic depositions. For the comparison: The mean area density of liquid hydrogen was 346 mg/cm^2 during this experiment and the one of the havar foil was 17 mg/cm^2.

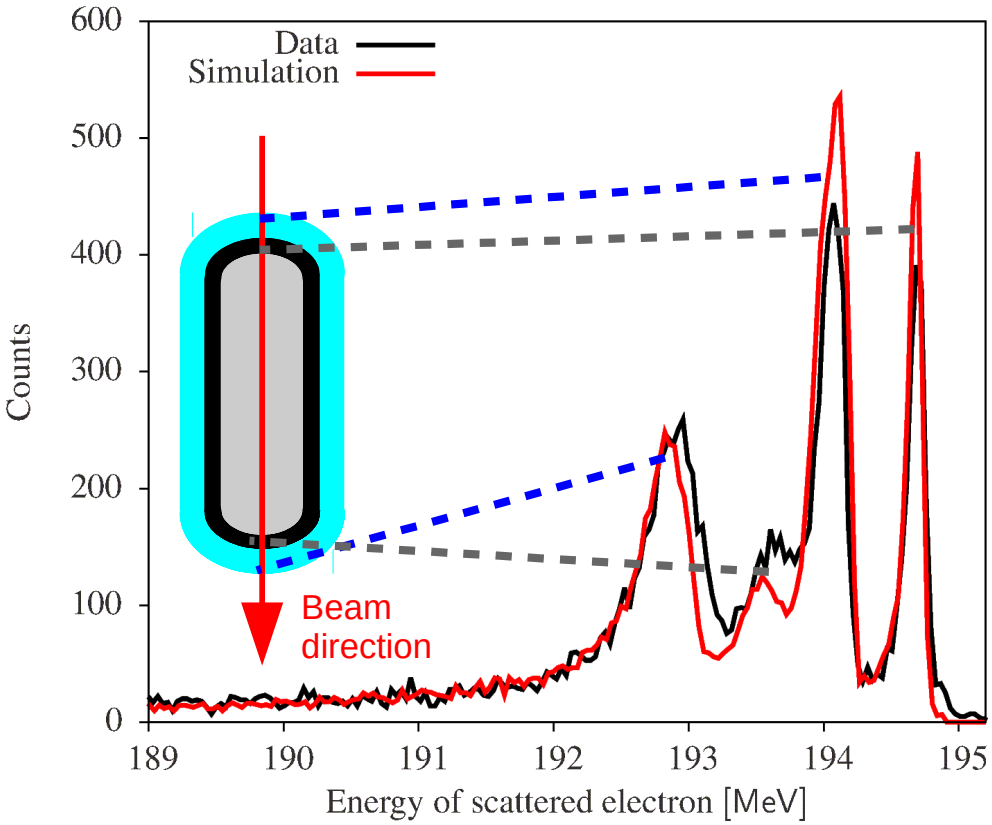

Figure 42: Cryogenic depositions for the setup with the beam energy of 195 MeV. In black the data and in red the simulation for the havar foil and the cryogenic deposition is plotted. The amount of cryogenic depositions was adjusted such that the integral of the data and the simulation matched. The four peaks, connected via the dashed lines to the model of the target cell, belong to electrons scattering off cryogenic depositions or the havar foil when entering or exiting the target cell. In the target model liquid hydrogen is plotted in gray, the havar foil in black and cryogenic depositions in cyan. The peak at 194.7 MeV was caused by electrons scattering off the havar foil at the entrance of the cell. The peak at 194.1 MeV was caused by electrons scattering off cryogenic depositions which were on top of the havar foil at the entrance. The peak at 193.6 MeV belongs to electrons scattering at the exit of the cell and the one at 192.9 MeV belongs to electrons scattering off cryogenic depositions on the exit of the cell. These two peaks are shifted because electrons lost energy when traversing the liquid hydrogen and the havar foils on their way through the target cell.

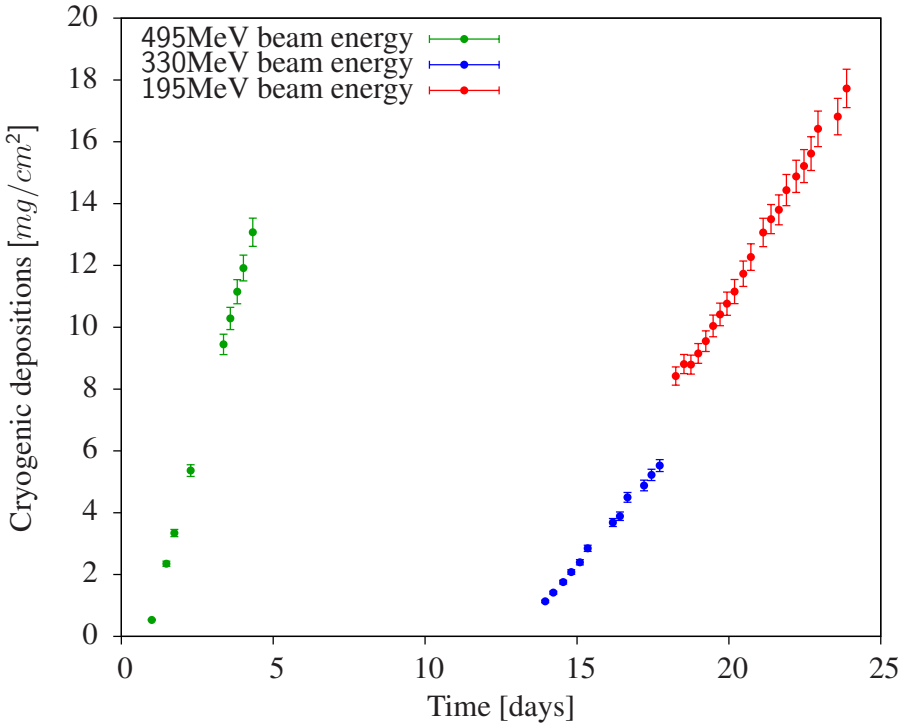

Figure 43: Result of the analysis of cryogenic deposition as a function of time. Each point belongs to one momentum setup. The time axis starts at the beginning of the beam time. The three energy settings are plotted in the displayed colors.

Entrance flange of Spec. B

In Fig. 44 the entrance flange of Spec. B is shown, which caused additional background. The effect which caused this is the same as for the target frame: It happened that scattered electrons interacted with this flange, scattered back into the acceptance of Spec. B and got recorded. These electrons would without the flange be out of the acceptance of the spectrometer. In the case of a setup for elastic scattering almost all of these background events could be successfully cut away. Unexpectedly this was not the case when measuring the radiative tail where the accepted momenta of the scattered electrons were far away from the elastic peak. To account for this effect a fit to the recorded data was made in order to estimate the amount of events stemming from the flange.
To fit the data an exponential function with an offset was considered. In Fig. 45 the fit to the data for the setting ISR_195_00 is shown. The contribution of events originating from the flange in the region of interest, which is on the vertex coordinate z from 1.5 mm to 11.5 mm, is very small as expected. Fig. 46 top shows the same plot for the setting ISR_195_05. There the amount of events stemming from the flange is comparable to the amount of events from the hydrogen itself and even in the region of interest a considerable amount of events came from the entrance flange, as can be seen by the approximation given by

Figure 44: Photo of the entrance flange of Spec. B.

the fit. Fig. 46 bottom displays the same plot for the setting ISR_195_19 as an example of the conditions when measuring at low momenta. Here no fit is shown because it would be not precise enough. In the setups with low accepted momentum at 195 MeV beam energy almost all events originated from scattering processes on the entrance flange. Therefore the setups ISR_195_06 to ISR_195_19 (see appendix A) had to be excluded from the final analysis.
In Fig. 47 the relative contribution of events originating from scattering processes at the entrance flange in the region of interest (ranging from 1.5 mm to 11.5 mm with respect to the vertex coordinate z, see below) is displayed for all three energy setups. To obtain these results the integral of the fit function in this region was divided by the integral of all events in this region. For the elastic settings this amount is very small and was rising with the decreasing value of the central momentum of Spec. B. For the fitting procedure an uncertainty of 3.5% was determined.
To avoid contributions of the entrance flange in future experiments of this kind it is necessary to replace the existing flange with a different construction. This replacement should have very thin walls, such that the cross section for electron scattering would be reduced for some orders of magnitude in comparison with the existing flange. Since such a construction would not be stable enough

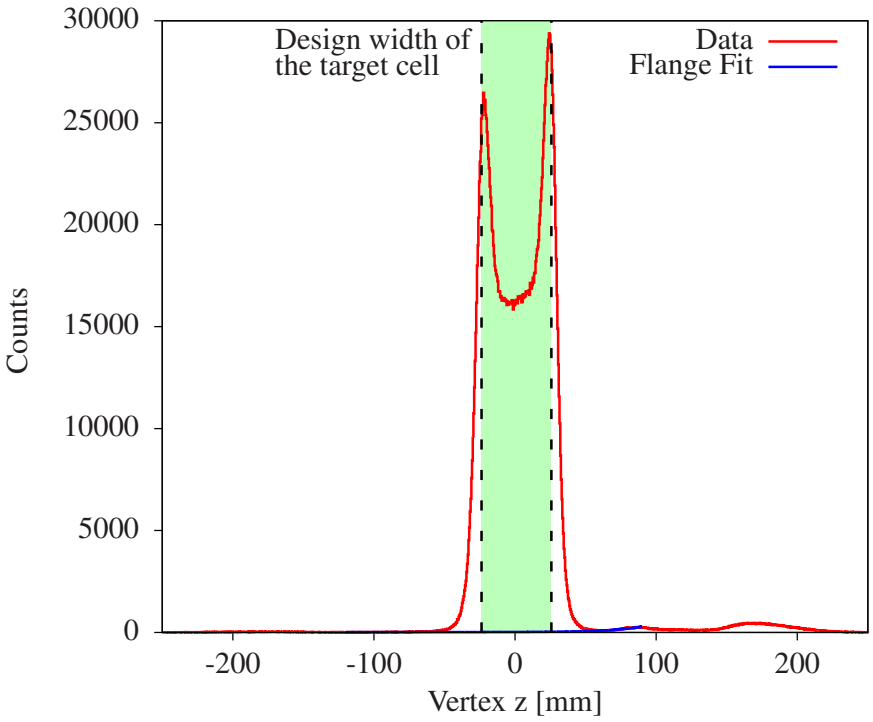

Figure 45: Data, shown in red, for the setting ISR_195_00 depending on vertex z. The amount of events stemming from the entrance flange of Spec. B is very small, visible on the right side. With a cut on the region of interest it could almost be completely eliminated. In blue a fit to approximate the amount of events coming from the entrance flange is shown. The green area illustrates the design width of the target cell.

to contain vacuum, it should be filled with helium, which has a much longer radiation length than air.

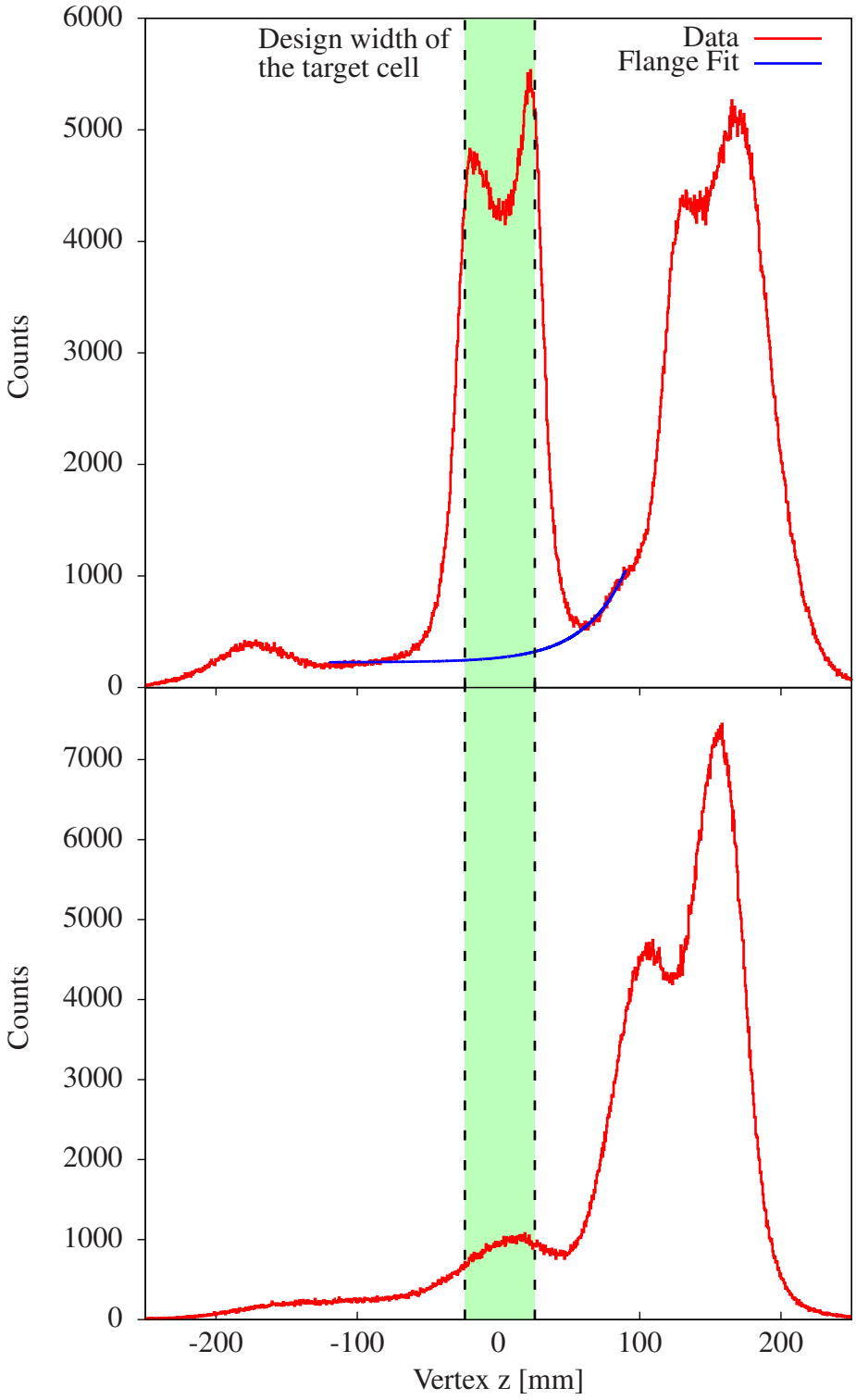

Figure 46: Top: Data, shown in red, for the setting ISR_195_05 depending on vertex z. The amount of events coming from the entrance flange of Spec. B is comparable to the amount of events stemming from the liquid hydrogen. In blue a fit to approximate the contribution of events coming from the entrance flange to the total number of events in the region of interest is shown. The green area illustrates the design width of the target cell.
Bottom: Data for the setting ISR_195_19 at the smallest measurable momentum. The amount of events coming from the entrance flange of Spec. B is larger than the number of events originating from liquid hydrogen.

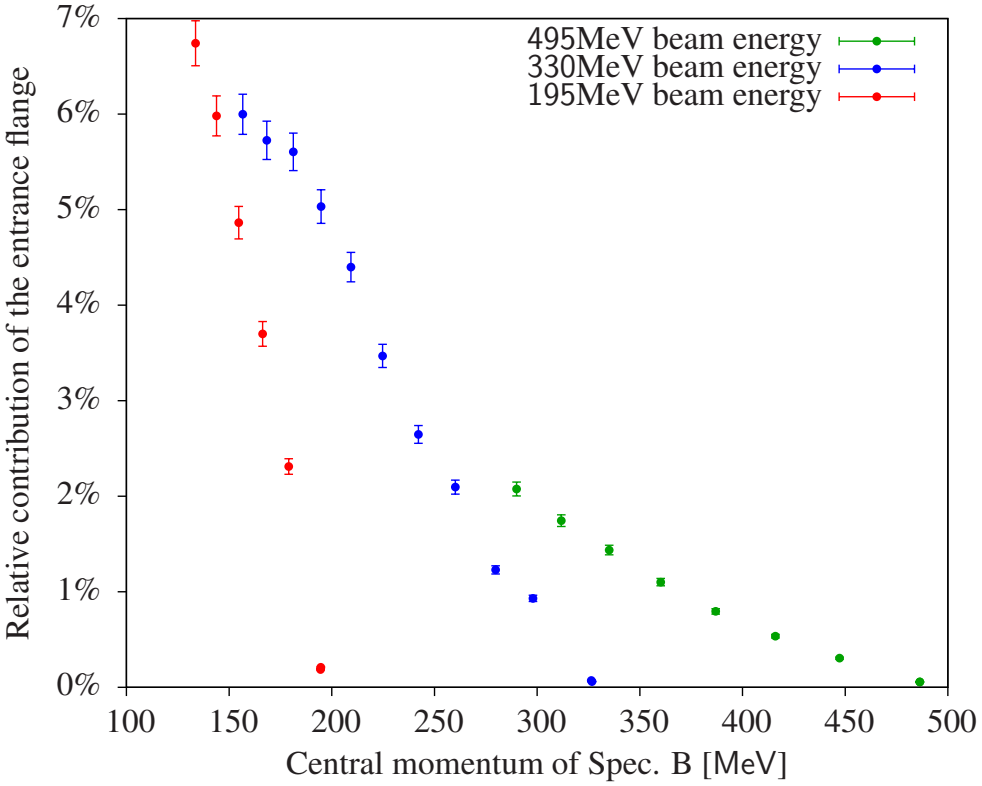

Figure 47: Relative amount of events originating from the entrance flange of Spec. B for all analysed energy settings.

Resolution determination

In Fig. 48 a qualitative picture of the analysis, which contains no actual data, in terms of the vertex coordinate z is shown.

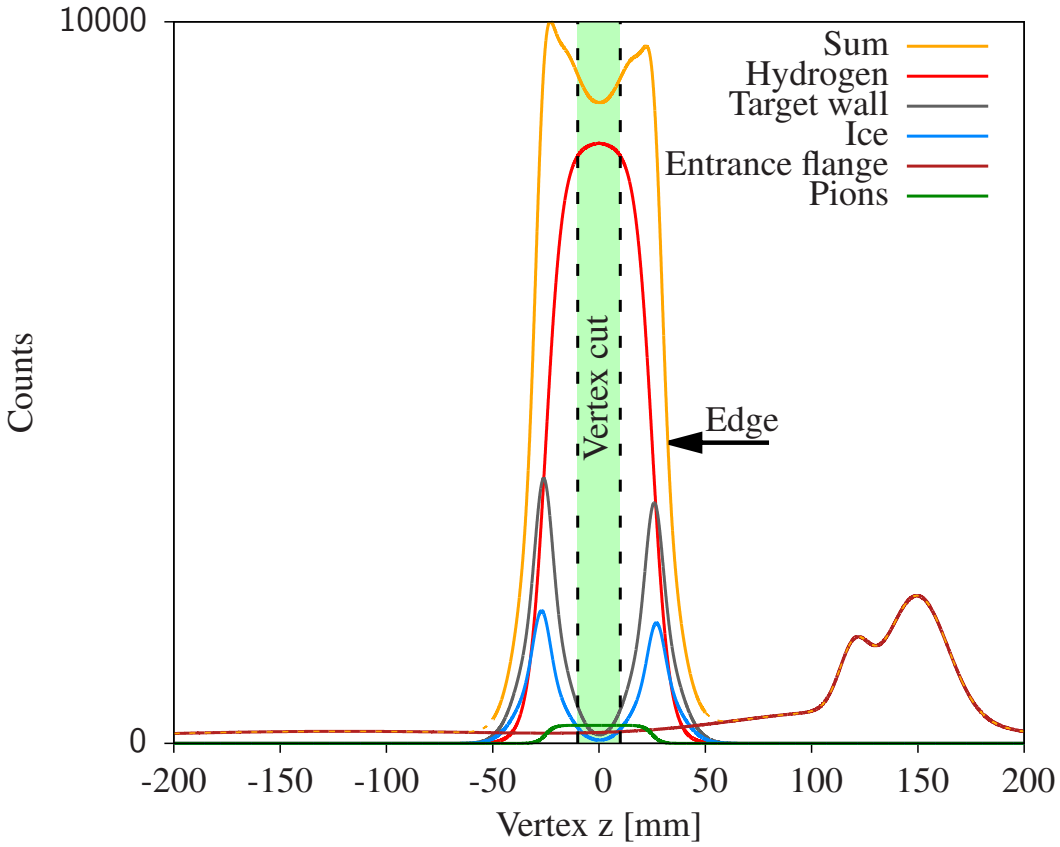

Figure 48: Qualitative example of the vertex z histogram in the analysis. This plot contains no actual data. During the experiment only the orange curve "Sum" would be measured. In this picture also the different contributions adding up to the orange curve are plotted, but they cannot be isolated in the actual analysis. Therefore the simulation will be needed, which is able to simulate the "Hydrogen" contribution, the "Target wall" contribution, the "Ice" contribution and the "Pion" contribution. The simulation will need the distribution of the "Edge" as an input parameter, which can be determined from the orange curve. This distribution depends on the resolution of Spec. B. The "Entrance flange" contribution will be estimated by the fitting procedure described above. The green area displays a possible cut for the final analysis such that the contributions from the target walls and the ice would be minimal.

There all the contributions, which were measured during the experiment, are plotted separately: In red the contribution from the hydrogen, in gray the contribution from the target walls, in blue the contribution from the cryogenic depositions, in dark red the contribution from the entrance flange and in green the contribution from the pions. In the actual data it was not possible to dis-

tinguish between these different contributions. In the data only the sum of all these contributions, which is shown in orange, was measured. Since only the contribution from hydrogen is relevant for the determination of the form factor, the simulation described above was needed to calculate all different contributions, in order to isolate the events originating only from hydrogen. An exception are the events originating from the target flange for which no simulation was available, therefore the fitting procedure described above was applied. In the simulation the resolution at the vertex coordinate z reconstruction was needed as an input parameter. It would be adjusted so that the edges, see Fig. 48, of the simulation matched the ones in the data. The vertex coordinate z would also be used to determine a cut which would removed most of the events originating from the havar foils or the cryogenic depositions. A possible cut condition is shown in Fig. 48.
In the actual analysis the chosen cut accepted events from 1.5 mm to 11.5 mm with respect to the vertex coordinate z for the entire analysis, see Fig. 49. This cut had to be applied to the data as well as to the simulation. In the simulation the quality of the cut depended on the knowledge of the vertex resolution of Spec. B. Therefore the resolution had to be determined for every single setup, because it depended on the central momentum of the spectrometer. To model the resolution a superposition of two Gaussian distributions was fitted to the data. This superposition was implemented in the simulation during the analysis of this experiment. At this point the simulation for the target wall and cryogenic deposition contribution was also scaled to match the height of the target walls in the simulation with the data. This scaling was needed because the form factors for the simulation of the target wall and the cryogenic deposition were only approximately known, see chapter 6.1. In Fig. 49 the result of the fitting procedure and the scaling is shown. For the scaling the interval ranging from vertex $z \in [19\,\text{mm},\ 26\,\text{mm}]$ was used. The scaling factor was adjusted such that the integral of the data and the simulation in this interval agreed. For the adjusting of the resolution the right edge in the plot was used as a reference point. The left edge was not chosen because there was the possibility that minor contributions stemming from the target frame would have influenced the result. During the adjusting process the parameters were tuned such that the data and simulation did agree best. An uncertainty of 3.5% was determined for these results. In the plots the different parts of the simulation are shown. In Fig. 49 (top) the results for the setting ISR_330_00 are displayed. Here no events originating from pion production were present and the effect of the entrance flange was so small, that it would not be visible, therefore this is not plotted. In Fig. 49 (bottom) the results for the setting ISR_330_10 are shown. Also the simulated events originating from pion production are shown. The data without the subtraction of the contribution from the entrance flange are shown as well. In Fig. 50 the contribution of the target walls and the cryogenic depositions determined with this procedure as well as the contributions from pion production for all analysed settings are plotted. The calculation of the pion production processes has an uncertainty of 5% due to the MAID model.

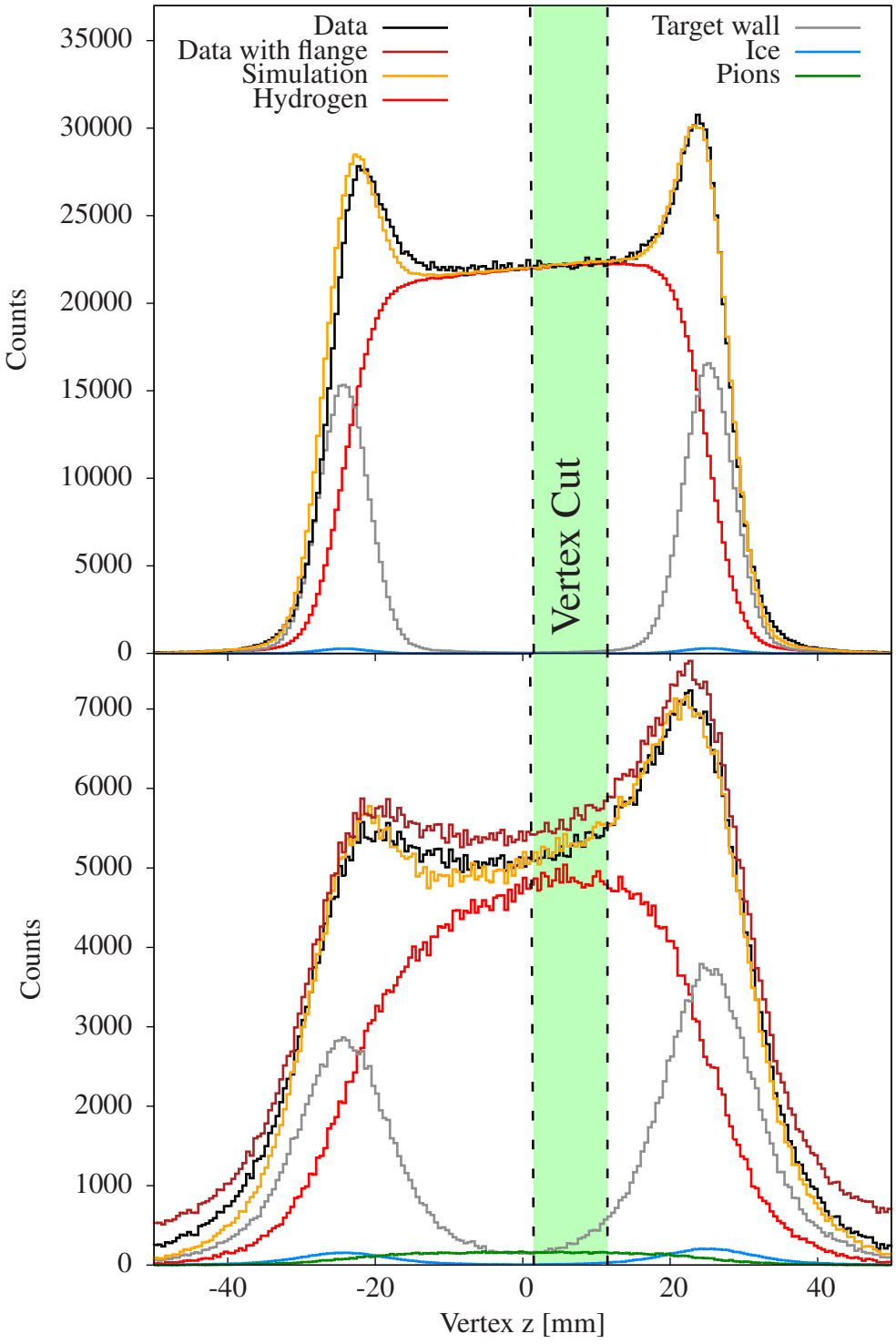

Figure 49: Top: Vertex plot for the setting ISR_330_00. The vertex resolution has been adjusted in the simulation such that it agreed with the one in the data. Data are plotted in black and the full simulation in orange. Simulation for electrons scattering only off liquid hydrogen is plotted in red, only off the target walls in gray and only off cryogenic depositions labeled "Ice" in blue. Inside the green band the events remaining after the vertex cut in the final analysis are shown.
Bottom: Vertex plot for the setting ISR_330_10. Electrons originating from pion production is plotted in green, data without the subtraction of the contribution of the entrance flange in dark red.

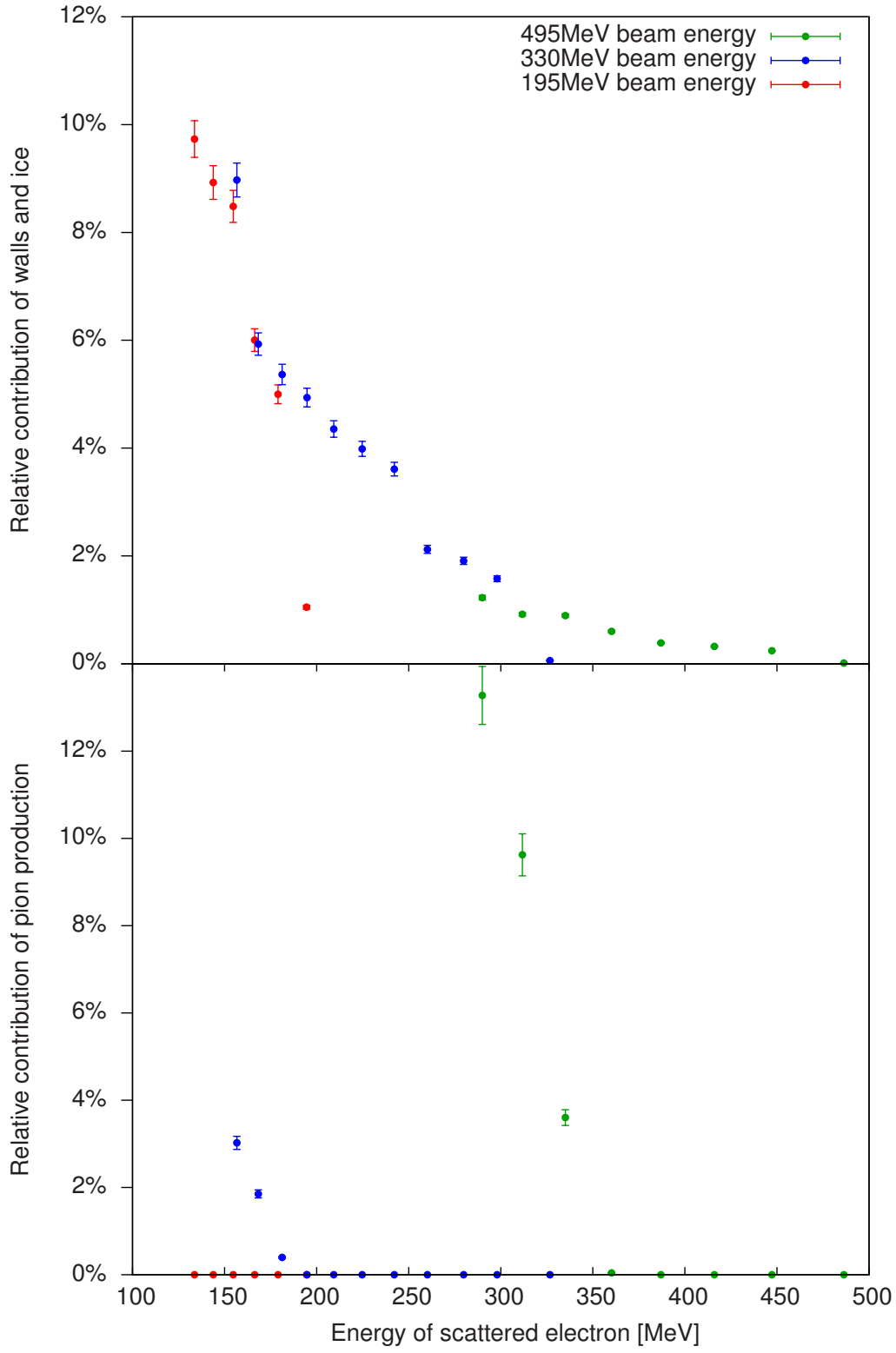

Figure 50: Top: Relative amount of events originating from the target walls and cryogenic depositions for all analysed settings.
Bottom: Relative amount of events originating from pion production for all analysed settings.

7

RESULTS

In Fig. 51 a qualitative picture for the comparison of data and simulation is shown. This plot contains no actual data and serves only as an illustration of how the comparison between data and simulation was done and what a difference between data and simulation implies. In this example each of the three beam energy configurations consists of three momentum settings. The settings have some overlap such that it can be checked, that the overlapping regions are consistent with each other. Also the data from the different beam energies are overlapping so that it can be checked if a possible deviation from the simulation is present in both energy settings. The simulated events are a combination of events from hydrogen, the target walls, cryogenic depositions and pion production. The data are corrected for the effect of the entrance flange. The cuts mentioned above are applied to the data, as well as to the simulation. In the part of the simulation, where the electron scatters off a proton, an established form factor will be used to calculate the cross section. It is not expected that the combined simulation will match the data perfectly, since the form factor was determined from a different experiment. The effect of an incorrect form factor is shown in Fig. 51. But if it would agree with the simulation in the order of a few per cent, this would justify the usage of the ISR method. Differences between data and simulation could also be due to higher order effects or uncovered backgrounds. However, if it would be assumed that the calculation of the cross section worked flawlessly, then the differences between data and simulation could be used to extract new values of the form factor. To determine these values, the form factor in the simulation will be adjusted, such that the data and simulation will match perfectly.
In the actual analysis a substantial discrepancy between data and simulation was observed for the elastic settings of all three beam energies. This discrepancy was greater than 10% between the elastic peak and 10 MeV below the elastic peak. This effect is shown in Fig. 52 for the setting ISR_495_00. To find the reason for this discrepancy first all possible inconsistencies concerning the data were investigated: The efficiencies of the detectors were examined in detail to check, if there was any inconsistency at the position where the elastic peak was measured, but none was found. The data taking rate was also checked, because in runs including the elastic peak many events were measured in a relatively small area of the detectors. Also there no problem could be found. The transfer matrices which translate the positions in the VDCs to the position at the target were investigated and it was found that they worked as expected. Also the cuts applied to the data and the simulation were

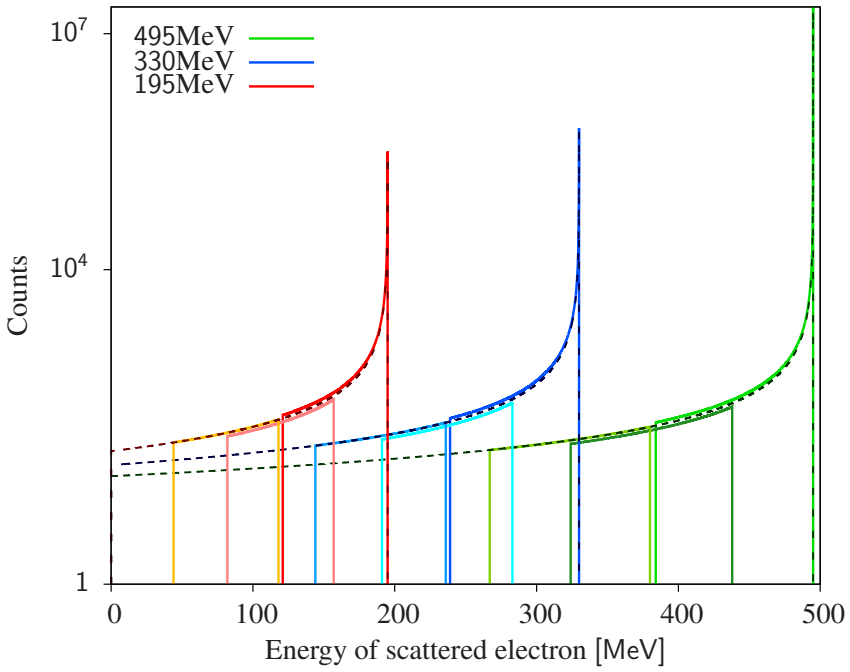

Figure 51: Qualitative example of the simulated and measured spectra in term of the energy of the scattered electron. The "data" are displayed greenish for the 495 MeV beam energy setting, blueish for the 330 MeV one and reddish for the 195 MeV one. Due to the limited acceptance of Spec. B only a part of the radiative tail can be covered with each setup. The "simulation", displayed in dashed lines for the three energy setups of the experiment, covers the whole range from the elastic peak to the point where the scattered electron virtually has no kinetic energy left.

checked and it was concluded that they worked as well as expected. Hence, all potential problems related to the data were excluded. Later the suspicion rose that the external radiative corrections are responsible for the discrepancy because they were not calculated with the same order of precision as the internal radiative corrections [79]. In Fig. 36 bottom the contribution of the external radiation is shown. It can be seen, that this distribution is almost flat in the radiative tail with a significant rise only in the immediate vicinity of the elastic peak. This significant rise of the correction might lead to an incomplete description of the momentum distribution. Therefore it was concluded that this might be the reason why no significant discrepancy appeared in the radiative tail. Especially in the region where the radiative tail of one energy setting overlapped with the elastic peak of another energy setting, no discrepancy in the radiative tail between the data and the simulation of more than about 1% was obtained, see Fig. 53 and 54. Within the scope of this study it was not possible to further investigate this matter. For future analyses the code underlying this simulation will have to be thoroughly checked and special attention will have to be paid to the external radiative corrections.

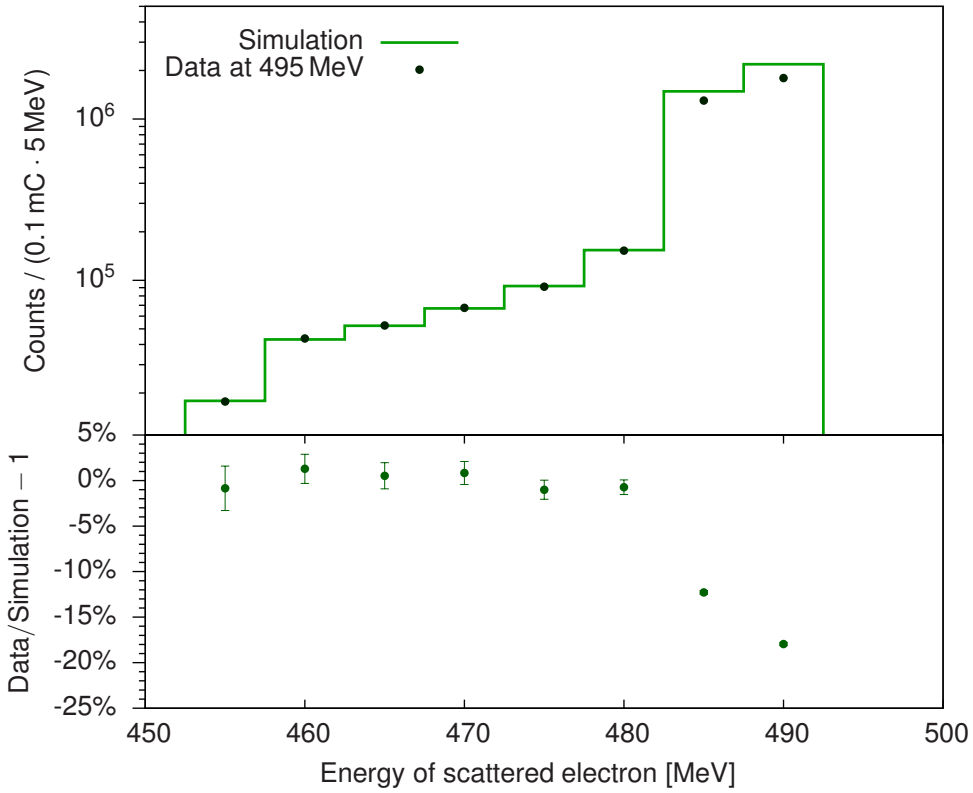

Figure 52: Comparison of data and simulation for the setting ISR_495_00. For the two bins with the highest energy of the scattered electrons there is a discrepancy between the data and simulation for more than 10%. This is probably due to an incomplete description of the external radiative corrections.

The results of the analysis are shown in Fig. 53 and 54. In the simulation the values of the form factor determined in Ref. [27] were applied. Data and simulation matched to about 1% along the whole radiative tail of each of the three different energy setups. Notably in the region, where two energy settings were overlapping, the results of both settings also matched to about 1%. Altogether this justifies the application of the initial state radiation method and is an important result of the analysis.
The remaining differences between data and simulation, apart from statistical fluctuations, could be due to higher order effects missing in the simulation or uncovered backgrounds. However, if it is assumed that the calculation of the cross section works flawlessly and the background processes are well under control, the discrepancies would be due to the difference between the true form factor in the data and the model of the form factor used in the simulation. Using this assumption it has been possible to determine new values of the proton electric form factor in the radiative tail.

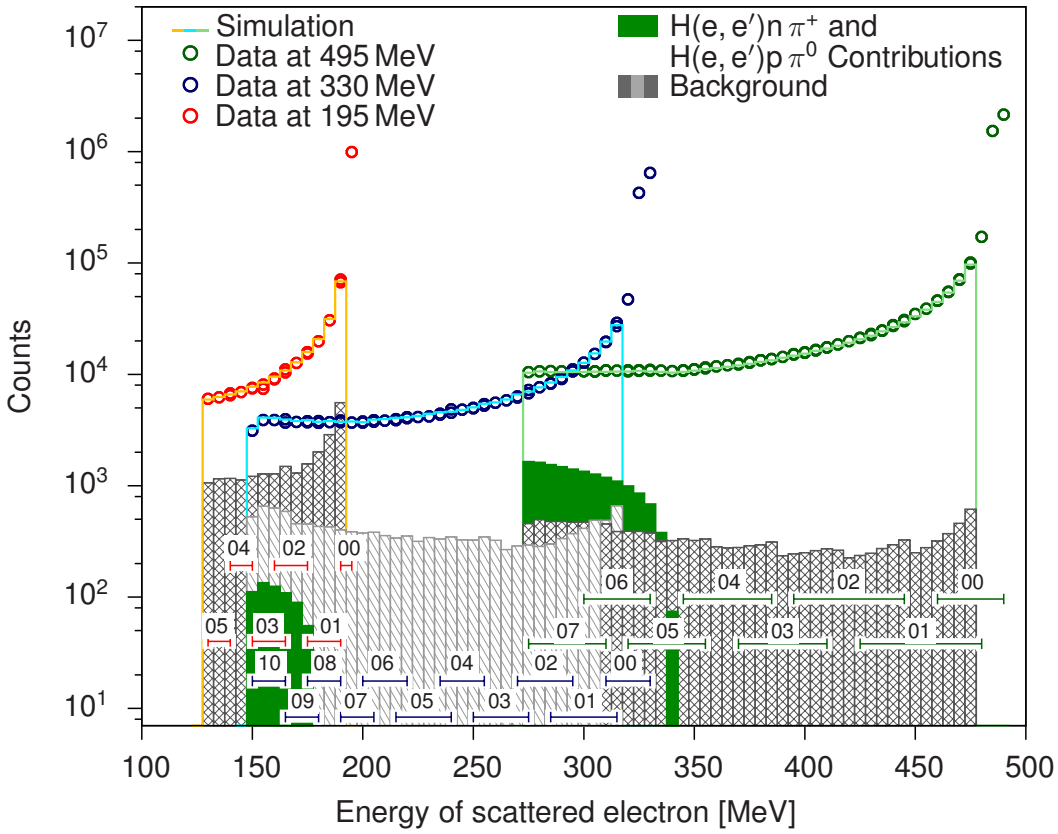

Figure 53: Results of the analysis of all momentum setups and energy settings. The three different beam energies are displayed in different colors. The data are plotted with open circles and the simulation is plotted with histograms. The contributions arising from the target walls, the cryogenic depositions, the target frame and the entrance flange are displayed in gray boxes. The contributions from pion production are displayed in green boxes. For the elastic setting of each beam energy no simulation is shown, because of the probably incomplete description of the external radiative corrections. The labelled bars at the bottom represent the acceptance of Spec. B for the corresponding settings (list of settings: appendix A). For the simulation the values of the form factor obtained in Ref. [27] were applied.

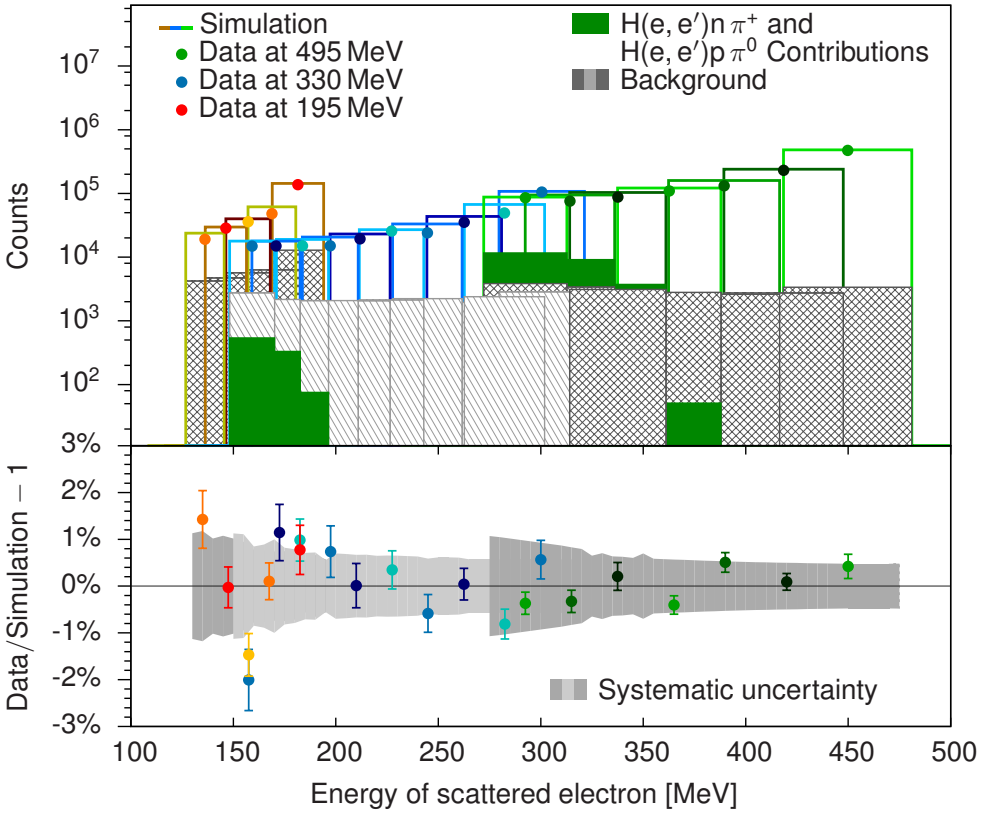

Figure 54: Top: Final results of the analysis of all momentum setups at all three energy configurations. The setups including the elastic peak are excluded because of the probably incomplete description of the external radiative corrections. The three different beam energies are displayed in different colors and the according momentum setups are displayed in variations of the same color to emphasise the different momentum settings. The data are plotted with dots at the position of the central momentum of the according setup. The simulation is plotted with histograms to display the covered momentum range. The contributions arising from the target walls, the cryogenic depositions, the target frame and the entrance flange are displayed with the gray boxes. The contributions from pion production are displayed with green boxes.
Bottom: Relative difference between data and simulation for every momentum setup. The statistical uncertainty is displayed by the error bars of the according dots. The systematic uncertainty is displayed by the gray error band. For the simulation the values of the form factor obtained in Ref. [27] were applied.

Therefore the form factor in the simulation was adjusted such that simulation and data matched perfectly. This needed to be done for every momentum setup separately. To obtain the value of the form factor, where data and simulation matched, the values of the form factor from Ref. [27] were changed for $\pm 5\%$ in steps of 0.1%. Thus for every momentum setup of the three different beam energies 101 individual simulations were performed. Each of these simulations was compared with the corresponding one, where the original form factor was applied. For the comparison of the results with the changed form factors and the results with the not modified form factors it was not enough to only calculate the ratio of the corresponding cross sections and relate this to the ratio between the form factor models. To calculate the cross section in the radiative tail two different values of the form factor are needed. For the calculation of FSR processes the same value of the form factor as for elastic scattering processes is used. This value is constant for the entire radiative tail. But for the calculation of ISR processes a different value of the form factor is needed for each momentum setting. When changing the model of the form factor, all values of the form factor were changed including the value for the FSR processes, see Fig. 55. However, only the contribution of the ISR part is needed. Therefore, for a faithful comparison, the result of each simulation was cut into two parts depending on the angle of the emitted photon, see Fig. 56. The first part contained events which originated from ISR processes. The second part contained events which originated from FSR processes. In order to determine how much the cross section depended on the change in the form factor, the simulation with the form factor model from Ref. [27] was compared with the changed form factor using the following expression:

$$\text{CS. deviation} = \frac{\text{ISR}_{\text{scaled}} + \text{FSR}_{\text{unscaled}}}{\text{ISR}_{\text{unscaled}} + \text{FSR}_{\text{unscaled}}} \,. \tag{52}$$

$\text{ISR}_{\text{unscaled}}$ and $\text{FSR}_{\text{unscaled}}$ are the contributions of ISR and FSR processes for the simulation with the form factor model from [27]. $\text{ISR}_{\text{scaled}}$ are the contributions of ISR processes for the simulation with the changed form factor model. The deviation of the cross section depending on the deviation of the form factor from the form factor of Ref. [27] is for the setting ISR_330_09 shown in Fig. 57. For small variations, like in this analysis, the difference of the cross section depended approximately linearly on the difference of the form factor. In Fig. 58 the slope of the cross section deviation depending on the form factor deviation for all analysed setups is shown. Therefore the corresponding data, exemplarily shown in Fig. 57, were fitted with a linear function. Using these results the values of the form factor of each setup were adjusted such that data and simulation matched exactly. The determined values of the form factor may be found in Fig. 59 and in appendix E.

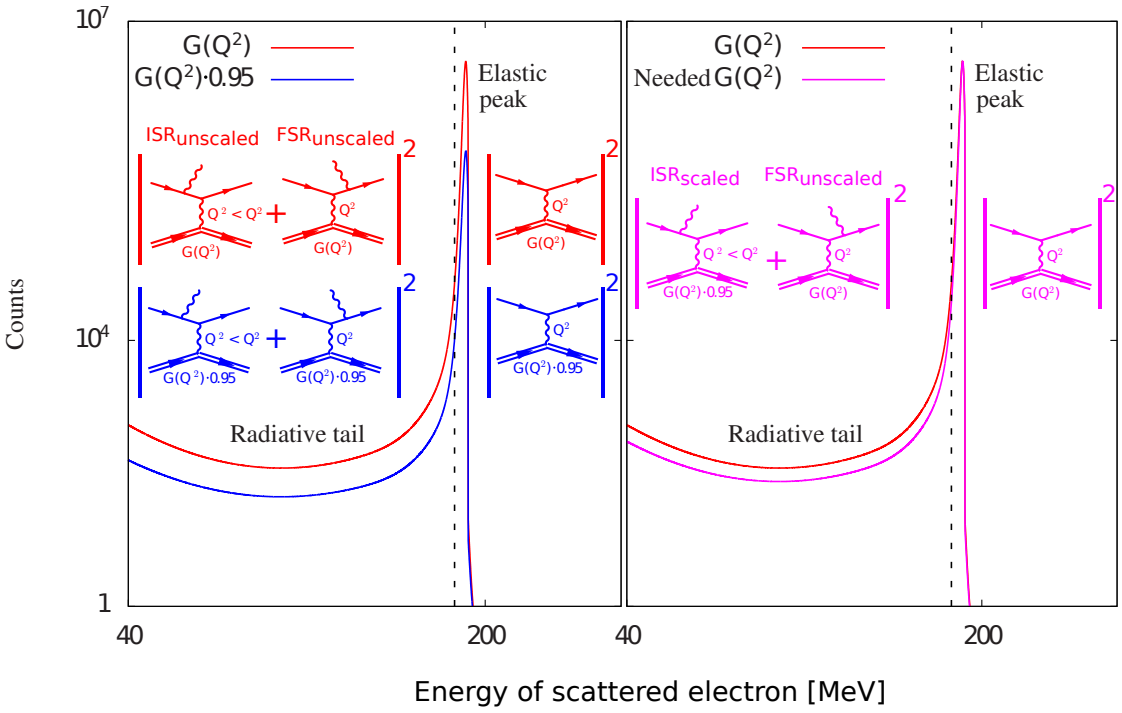

Figure 55: Qualitative illustration (this plot contains no actual data) of the measured distributions with the original and those with the changed form factors. For the results shown in Fig. 54 the form factor model from Ref. [27] was applied. The goal was to determine the values of the form factor for which the data exactly matched the simulation. In the simulation the form factor could only be adjusted simultaneously for all Q^2 by the same amount. However, for the purpose of this analysis only the value of the form factor for ISR processes should be adjusted, since for FSR processes the value of the form factor is the same as for elastic scattering for the entire radiative tail. The red curve and the red Feynman diagrams represent a qualitative example when the original form factor (from Ref. [27]) was applied. The blue curve represents a qualitative example of the change in the count rate (and the cross section) if the form factor was reduced for 5%. As mentioned above, this implies that for ISR and FSR processes the value of the form factor changed, which is illustrated by the blue Feynman diagrams. But the goal was to learn how the count rate (and the cross section) changed if only the value of the form factor for ISR processes changed and the value of the form factor for FSR processes did not change, which is illustrated by the magenta Feynman diagrams. The count rate for this situation is qualitatively shown by the magenta curve. To obtain the desired results the cuts shown in Fig. 56 and then equation 52 had to be applied. The variables used in equation 52 are attributed to the corresponding Feynman diagrams in the plot.

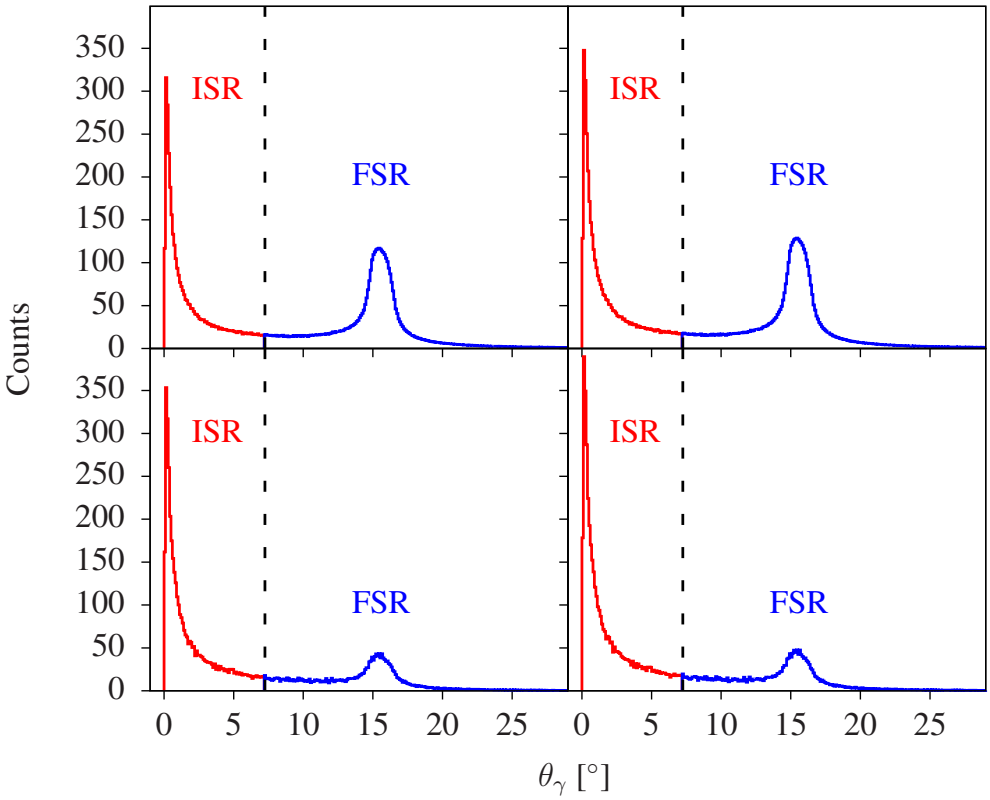

Figure 56: The plots show the distribution of the emitted photon for different setups as a function of the polar angle θ_γ between the emitted real photon and the direction of the beam. The dashed black line shows the cut which was made to distinguish ISR from FSR processes. Top left shows the simulation for the setting ISR_330_01 where the form factor from Ref [27] was used, top right shows the same plot but the form factor was increased by 5%. Bottom left shows the simulation for the setting ISR_330_10 where the form factor from Ref [27] was used, bottom right shows the same plot but the form factor was increased by 5%.

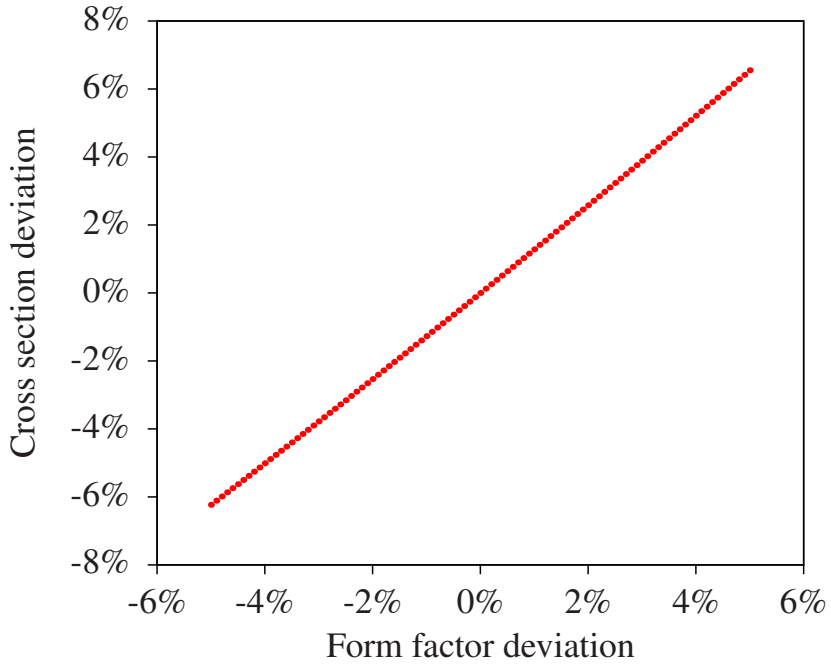

Figure 57: Change in the electron proton scattering cross section depending on the deviation of the form factor in the simulation from the form factor determined in Ref. [27] for the setting ISR_330_09.

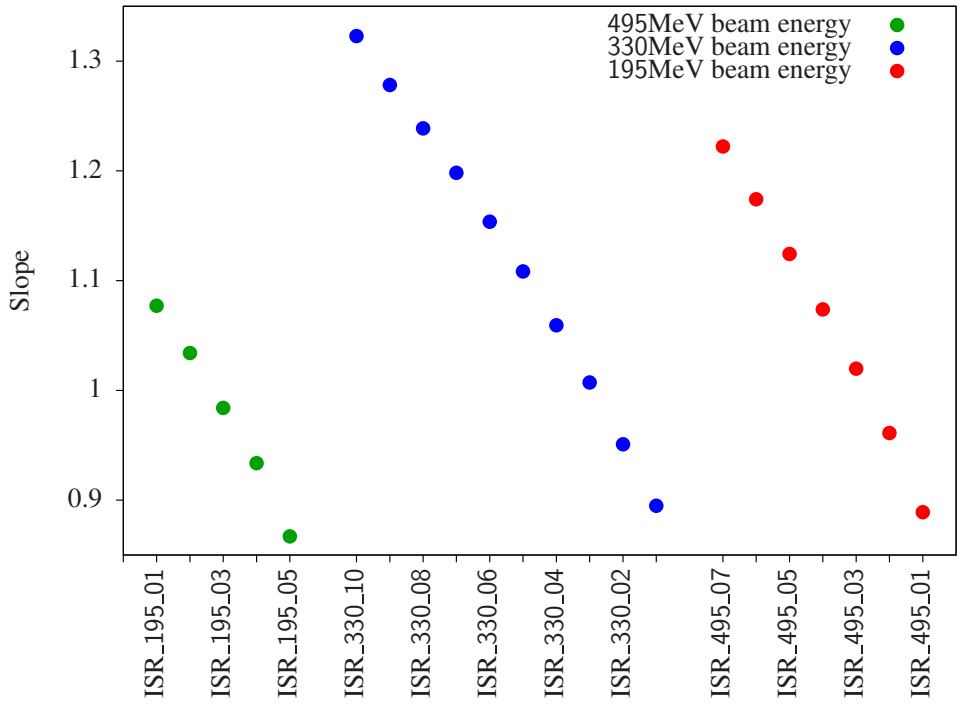

Figure 58: For every analysed setup the slope of the cross section deviation for a given form factor deviation is shown. The slope was determined by fitting a linear function to the cross section deviation depending on the form factor deviation, as it is shown in Fig. 57 for the setting ISR_330_09.

7.1 *Systematic uncertainties*

One advantage of the initial state radiation method is that the sources of systematic uncertainties are much reduced because the parameters of the spectrometers, except for the magnetic field of Spec. B, were not changed during the entire beam time. Furthermore the relative luminosity was monitored by Spec. A rather than measuring only the beam current. Nevertheless some sources of systematic uncertainties occurred during the analysis and are described below:

- The events originating from the pion production have an uncertainty of 5% due to the usage of the MAID model. For the entire analysis this contributed an uncertainty smaller than 0.5%.
- The simulation of background events and the determination of the vertex resolution caused a systematic uncertainty. These two factors are complementary, because a change in the vertex resolution automatically changes the contribution of background events in the analysis, see chapter 6.2, and vice versa. By varying the resolution this uncertainty was found to be 3.5% of the contribution of the background events. For the entire analysis this contributed an uncertainty smaller than 0.5%.
- The determination of the contribution of events originating from the entrance flange led to an uncertainty of 3.5% of the events originating from the entrance flange. This is due to the fit which determined the contribution of these events. For the entire analysis this contributed an uncertainty smaller than 0.2%.
- The contamination with events coming from the target frame led to an uncertainty of 0.4%.
- The simulation for the electron proton scattering cross section led to an uncertainty of 0.3% due to higher order corrections which were not included.
- The relative luminosity determination with Spec. A led to an uncertainty of 0.2% for each momentum setup.
- The uncertainty of the determination of the detector efficiency is 0.2%.

7.2 *Proton radius*

Finally the obtained values of the form factor could be fitted with an appropriate model and the charge radius of the proton could be determined. Unfortunately the major part of the 195 MeV setting, which would provide values of the form factor at very small Q^2, could not be analysed. This implies that the data which could constrain the normalisation, because of the boundary condition: $G_E\left(Q^2 \to 0\right) = 1$, are still missing. Additionally the obtained data have also a

limited reach at high Q^2 giving only limited strength for a precise enough determination of the parameters of a fit. Therefore a simple polynomial fit model with two parameters was chosen, given by the following expression:

$$G_E\left(Q^2\right) = \left(1 - \frac{r_E^2}{6 \cdot \hbar^2} Q^2 + \frac{a}{120 \cdot \hbar^4} Q^4 - \frac{b}{5040 \cdot \hbar^6} Q^6\right), \tag{53}$$

r_E^2 is the squared of the charge radius of the proton. $a = (2.59 \pm 0.19)\,\mathrm{fm}^4$ and $b = (29.8 \pm 14.7)\,\mathrm{fm}^6$ were adopted from Ref. [80]. For each energy setting one global normalisation factor was also still unknown, because with Spec. A only the relative luminosity was determined. These factors were used as open parameters during the fitting procedure. They were adjusted such that the boundary condition: $G_E(0) = 1$ was fulfilled. The result for the normalisation yielded: $n_{195} = 1.006 \pm 0.002_{\mathrm{stat.}} \pm 0.003_{\mathrm{syst.}}$, $n_{330} = 1.002 \pm 0.001_{\mathrm{stat.}} \pm 0.003_{\mathrm{syst.}}$ and $n_{495} = 1.005 \pm 0.002_{\mathrm{stat.}} \pm 0.008_{\mathrm{syst.}}$. The fit has a χ^2 of 58.0, where only the statistical uncertainties were considered, and 18 degrees of freedom. This indicates that the results are dominated by systematic uncertainties. In Fig. 59 the resulting values of the form factor and the resulting fit function are shown. The orange band around the fit displays the statistical uncertainty and the yellow band shows the combined statistical and systematic uncertainty. The error bars of the form factor represent the statistical uncertainty while the systematic uncertainty is plotted as the gray band at the bottom. As the two parameters a and b from Ref. [80] also have uncertainties, a model dependent uncertainty was calculated. The result of the fit yields:

$$r_E = \left(0.810 \pm 0.035_{\mathrm{stat.}} \pm 0.074_{\mathrm{syst.}} \pm 0.003_{\mathrm{mod.}}\right)\ \mathrm{fm}\,. \tag{54}$$

This value has a large uncertainty and cannot distinguish between former results of elastic electron scattering experiments [3] and the result from muon spectroscopy [2].

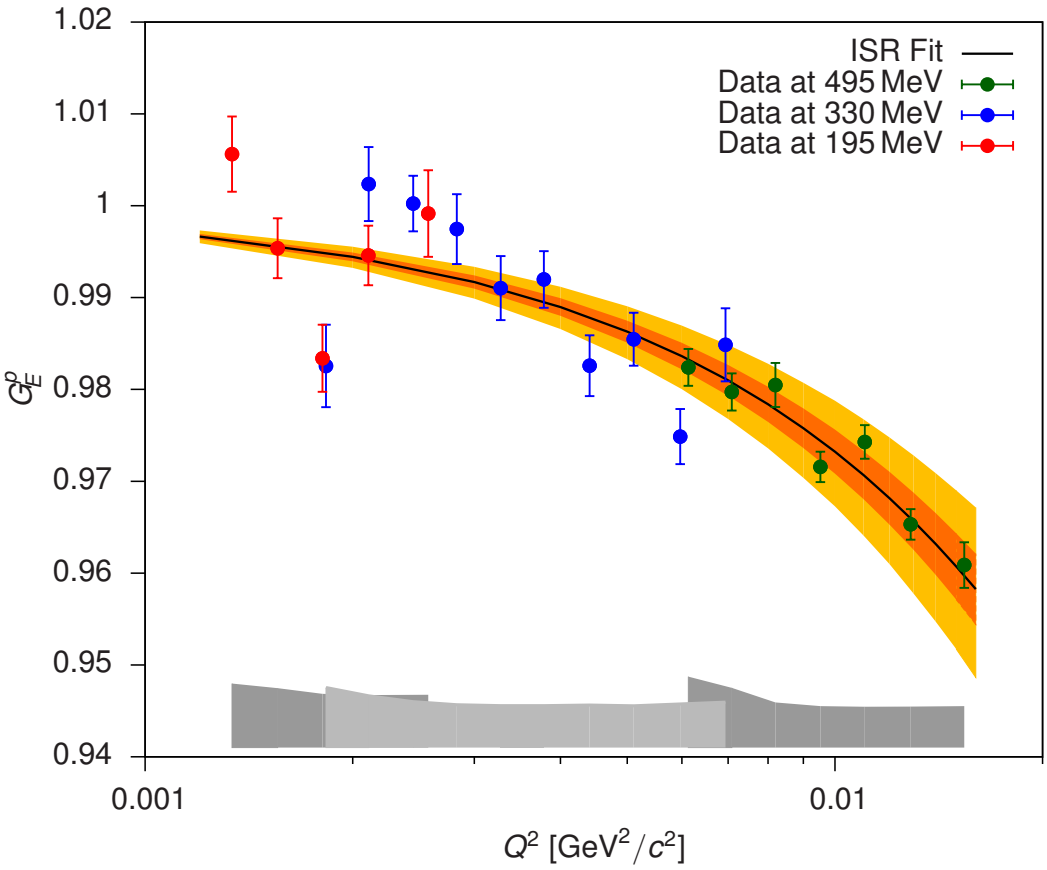

Figure 59: Form factor obtained with the ISR experiment. The error bars of the data points are the statistical uncertainties while the systematic uncertainties are represented by the gray band at the bottom. The fit to the data is shown with the black line. The orange band surrounding the fit represents the statistical uncertainty and the yellow band represents the statistical and the systematic uncertainties of the fit, added in squares. The range of the fit is given just for the Q^2 range investigated during the experiment.
The two values of the form factor at about $0.0018\,(\mathrm{GeV/c})^2$, which are both smaller than the surrounding values were obtained from the settings ISR_330_10 and ISR_195_03. Since the form factor is supposed to be a smooth distribution, both setups were carefully investigated, but no reason for the deviation was found.

8

CONCLUSION AND OUTLOOK

The objective of the presented experiment was to justify the usage of a new experimental technique based on initial state radiation and to use this approach to precisely determine the proton electric form factor at values of Q^2 as low as $Q^2 \approx 10^{-4}\,(\mathrm{GeV/c})^2$ in the A1 hall of the MAMI facility.
In the analysis the experimental data were compared with a simulation, which exactly calculated the Bethe-Heitler and Born diagrams and included higher order diagrams as effective corrections to the cross section. The results of the comparison presented in this work demonstrate that electro-magnetic processes responsible for the radiative tail are understood below a per cent level in regions that are more than 200 MeV away from the elastic peak. Also the overlapping parts of the three energy settings are in agreement to about 1%, thus proving the ISR method to be a valuable experimental technique, which, under the assumption of the flawless description of the calculation of the cross section, can be employed to determine the proton electric form factor at very small four momentum transfers.
Unfortunately, in the present experiment the determination of the form factor at the smallest measured values of Q^2 was obstructed by huge amounts of background events, that were not foreseen before the experiment. There were two major contributions to the background: the entrance flange of Spec. B and the support construction of the target frame. Although the effects of these contributions were studied thoroughly, it was not possible to analyse the setups with Q^2 below $1.3 \cdot 10^{-3}\,(\mathrm{GeV/c})^2$. This was mostly due to the immense systematic uncertainty related to these corrections. Additionally, the incomplete description of the momentum distribution, which is possibly due to the incomplete description of the external radiative corrections, in the vicinity of the elastic peak prevented the inclusion of these setups in the final analysis. In spite of these hindrances, the experiment provided first measurements of the proton electric form factor at Q^2 between $1.3 \cdot 10^{-3}\,(\mathrm{GeV/c})^2$ and $4 \cdot 10^{-3}\,(\mathrm{GeV/c})^2$. The newly obtained data were then fitted with a simple polynomial model and a value for the proton charge radius was extracted:

$$r_E = \left(0.810 \pm 0.035_{\mathrm{stat.}} \pm 0.074_{\mathrm{syst.}} \pm 0.003_{\mathrm{mod.}}\right)\ \mathrm{fm}\,.$$

Due to large uncertainties, related to the huge amount of backgrounds, the obtained result cannot distinguish between previous results of scattering experiments [3] and the results from muon spectroscopy [2].
However, this was only the first experiment of this kind. To fully exploit the potential of the initial state radiation method and improve the present result, a

next generation experiment is already being commissioned at the A1 setup at MAMI. The new experiment will eliminate the shortcomings of this experiment by replacing the metal entrance flange of Spec. B with a balloon filled with helium, and by substituting the traditional cryogenic cell with a windowless gas jet target. The gas jet target is already being developed and tested for the operation in the A1 hall [6]. These measures will remove the backgrounds coming from metal parts of the experimental equipment and cryogenic depositions which limited the reach of the present experiment. Employing a point-like gas jet target will also minimise the external radiative corrections.
After the application of the gas jet target in the A1 hall it is planned to be moved to the future MESA (Mainz Energy recovering Superconducting Accelerator) accelerator facility [6]. There the MAGIX experiment will utilise it together with two high resolution magnetic spectrometers and with an electron beam energy of 105 MeV it will offer further measurements of the proton electric form factor at even smaller values of Q^2 [81].

A

EXPERIMENTAL SETUPS

Setup	Momentum [MeV/c]	Q^2 [$(GeV/c)^2$]
ISR_495_00	486.320	0.01704
ISR_495_01	447.244	0.01540
ISR_495_02	415.999	0.01288
ISR_495_03	386.976	0.01105
ISR_495_04	360.203	0.00952
ISR_495_05	335.094	0.00820
ISR_495_06	311.741	0.00709
ISR_495_07	289.964	0.00613
ISR_495_08	486.371	0.01704
ISR_330_00	326.680	0.00781
ISR_330_01	297.980	0.00694
ISR_330_02	279.811	0.00597
ISR_330_03	260.166	0.00511
ISR_330_04	242.191	0.00441
ISR_330_05	224.725	0.00379
ISR_330_06	209.324	0.00328
ISR_330_07	194.783	0.00283
ISR_330_08	181.240	0.00245
ISR_330_09	168.329	0.00211
ISR_330_10	156.663	0.00183
ISR_330_11	326.364	0.00781

Table 4: Setup name, central momentum of Spec. B and mean measured Q^2 for the experimental settings when measuring with a beam energy of 495 MeV and 330 MeV. The last setting of each beam energy is the repetition of the first one, which was used for the control of systematic effects.

Setup	Momentum [MeV/c]	Q^2 [$(GeV/c)^2$]
ISR_195_00	194.511	0.00273
ISR_195_01	179.025	0.00257
ISR_195_02	166.332	0.00211
ISR_195_03	154.709	0.00181
ISR_195_04	143.868	0.00156
ISR_195_05	133.658	0.00134
ISR_195_06	124.267	0.00116
ISR_195_07	115.382	0.00100
ISR_195_08	107.193	0.00086
ISR_195_09	99.6290	0.00074
ISR_195_10	92.3967	0.00064
ISR_195_11	85.9388	0.00055
ISR_195_12	79.7060	0.00047
ISR_195_13	73.9986	0.00041
ISR_195_14	68.6424	0.00035
ISR_195_15	63.7212	0.00030
ISR_195_16	59.1592	0.00026
ISR_195_17	54.9190	0.00023
ISR_195_18	51.6505	0.00020
ISR_195_19	48.1317	0.00017
ISR_195_20	194.637	0.00273

Table 5: Setup name, central momentum for Spec. B and mean measured Q^2 for the experimental setting when measuring with an electron of 195 MeV. The last setting is the repetition of the first one, which was used for the control of systematic effects.

B

TARGET CLASS

The class `cryo_ewald_2014` takes care of the cryogenic hydrogen target in the `Cola++/Simul++` analysis package. This class calculates the energy losses of electrons along their path from the scattering chamber to the spectrometer. The class has several functions of which different ones are called depending whether `Cola++` or `Simul++` is used.
In order for the class to work correctly with `Simul++` it needs input parameters which are stored in a text file called `run.db` [64]. There the length of the target cell (`Target.Length` in mm), the thickness of the cryogenic depositions (`Target.SnowThickness` in mm), density of the cryogenic depositions (`Target.SnowDensity` in g/cm^3), the thickness of the target wall (`Target.WallThickness` in mm), the density of the target material (`Target.Density` in g/cm^3) and the flags related to radiative corrections (`Target.externalRadiation` and `Target.internalRadiation`) have to be entered. The basic geometry of the target cell is hard coded, but the length of the long side may be varied from the default setting. In the `run.db` the area, where scattering takes place, also has to be stored. It is possible to choose between `Cryo.2014_hydrogen`, `Cryo.2014_wall` and `Cryo.2014_ice`, the reaction then takes place in the liquid hydrogen, the havar foil or the cryogenic depositions respectively. Once the desired part of the target is selected, the energy loss of the electron traversing the target cell is calculated, which is the main purpose of this class, see Fig. 60. After this calculation is done, the model to calculate the cross section for each option has to be chosen.
When `Simul++` is executed the values from the `run.db` are read, for example for the `Cryo.2014_hydrogen` target this is `ElasticProton`. Later a member of the class `cryo_ewald_2014` is initialised. Then the function `setPara` is called and appropriate values from the `run.db` are stored in the class variables. The incoming electron four-vector is defined by the direction and energy of the beam given in the `run.db`. The simulation randomly determines a scattering vertex in a rectangle. This vertex is passed to the function `Generate_Vertex` which checks, if this vertex is inside or outside of the designated reaction area. If it is inside, the event is further processed, otherwise the event is ignored. If it is accepted the function `EnergyLossSimBeam` is called which calls the function `getLength_in_Target`. It calculates the distances in the liquid hydrogen, havar and cryogenic depositions from the point where the electron enters the target to the vertex point. Then the most probable energy loss through this three paths is calculated using the Landau's Theory [82]. Also the energy loss due to external and internal Bremsstrahlung is corrected for. The correction of the

internal Bremsstrahlung is deactivated for this experiment because the generator for the cross section calculation already includes this correction. There is also a correction to the scattering angle due to multiple Coulomb scattering [82]. Then the four-vector of the scattered electron is calculated. After that the function `EnergyLossSim` is called. This basically does the same as the function `EnergyLossSimBeam`, except that it uses the distances from the scattering vertex to the exiting point of the scattered electron for the correction. Then the function `EnergyLossSimChamber` is called which corrects the scattered electron for Coulomb multi scattering and the most probable energy loss through the windows between the scattering chamber and the detectors as well as the air gap between the scattering chamber and the entrance of the spectrometer.
The calculation of the energy loss is different if the analysis of data is done with `Cola++`. When using `Cola++` the trajectories of the incoming electron and the scattered electron are already known because of the information from the detectors. The purpose of the energy loss correction is to determine the energy of the incoming electron and scattered electron at the scattering vertex. Therefore first the function `EnergyLossCorrChamber` is called which applies the Bethe-Bloch formula [82] to calculate the energy losses in the windows between the scattering chamber and the detectors as well as the energy loss in the air gap between the scattering chamber and the entrance of the spectrometer. The scattered electron is corrected for this energy loss. Then the function `EnergyLossCorr` is called. This function calls the function `getLength_in_Target` which calculates the distances of the electron from the scattering vertex to the exiting point of the scattered electron of the target cell through the liquid hydrogen, the havar foil and the cryogenic depositions. The energy losses through these three paths are again calculated with the Bethe-Bloch formula and the energy of the scattered electron is corrected for this value. Then the function `EnergyLossCorrBeam` is called. This function also calls the function `getLength_in_Target` which now calculates the distances of the electron from the scattering vertex to the entrance point of the incoming electron into the target cell through the liquid hydrogen, the havar foil and the cryogenic depositions. The energy losses through these three paths are again calculated with the Bethe-Bloch formula and the energy of the incoming electron is corrected for this value.

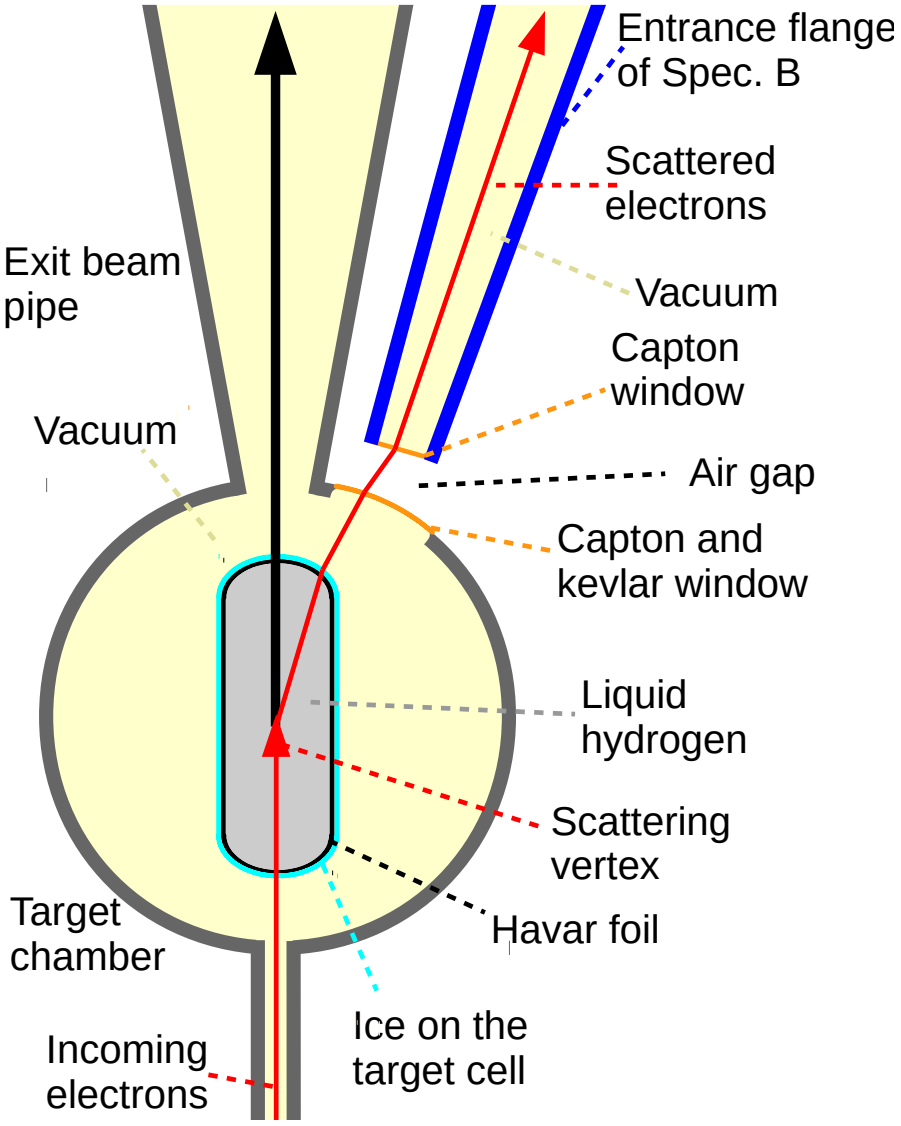

Figure 60: Schematic drawing of the scattering process and the material the incoming and scattered electron has to go through.

C

ANGULAR COORDINATES

In Fig. 61 and Fig. 62 the comparison of the non-dispersive and dispersive angle in the simulation and in the data for the setting ISR_330_10 is shown. For these plots all cuts used during the analysis, which are described above, were applied.

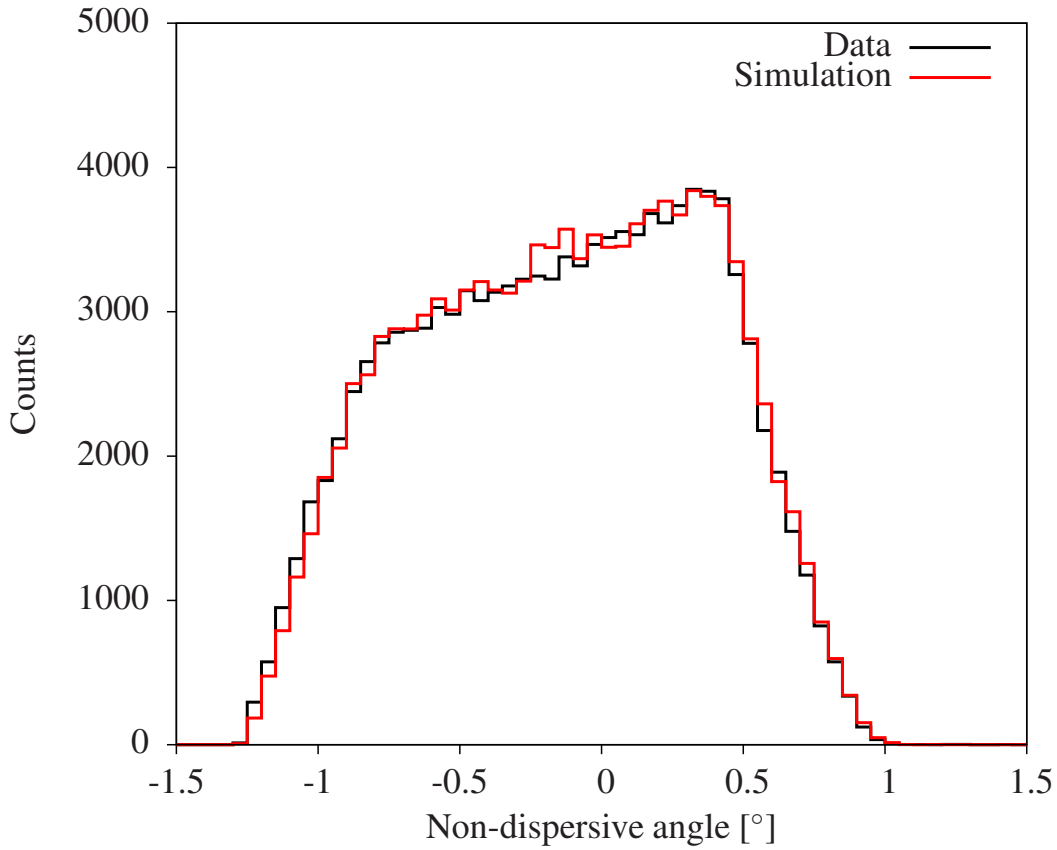

Figure 61: Comparison of the non-dispersive angle obtained with the simulation and reconstructed from the data for the setting ISR_330_10.

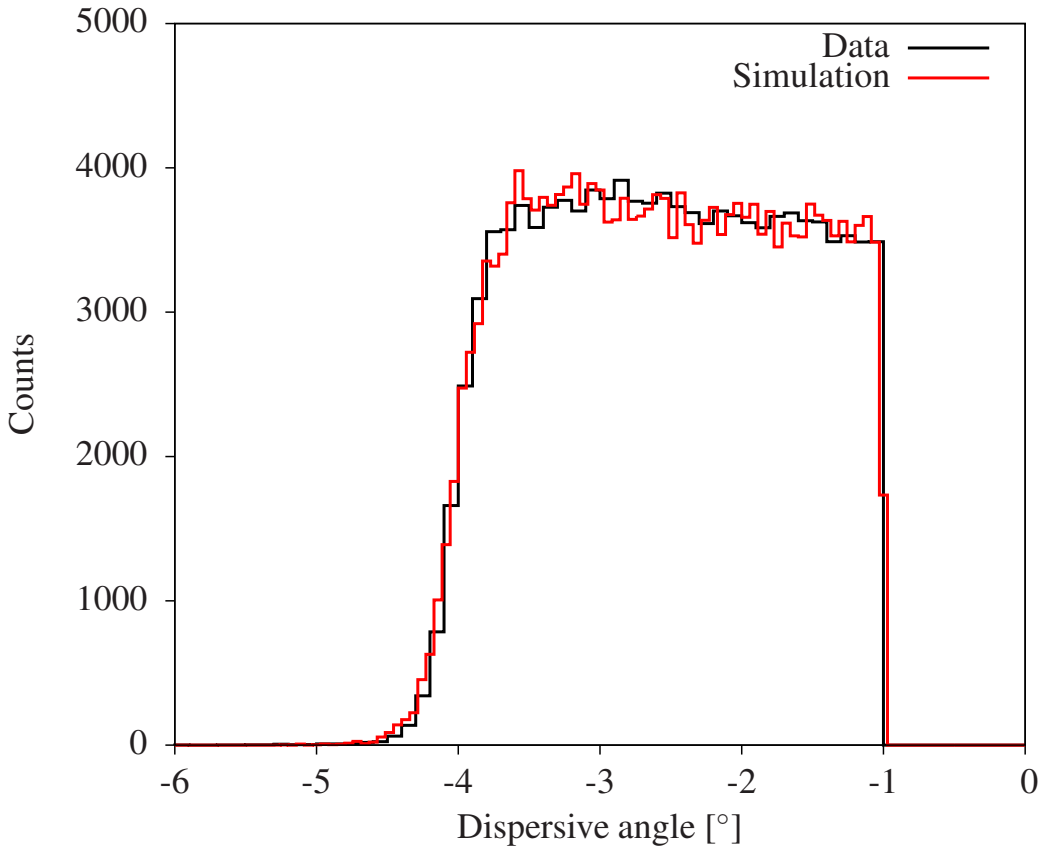

Figure 62: Comparison of the dispersive angle obtained with the simulation and reconstructed from the data for the setting ISR_330_10.

D

TARGET FRAME

During the online analysis of the experimental data, effects caused by the target frame, which are shown in Fig. 38 and 39, were found. It was not instantly apparent where the events causing the effect originated from. At some point during the experiment the frame of the target cell was assumed to be the source for the effect. To verify this, the beam was rastered with high amplitudes of a few millimeters. The result of this test is shown in Fig. 63. On the right side the actual target with the target frame and the havar foil is displayed. In the left plot the contribution of the lower frame is clearly visible as well as the target foils. The barycenter of the beam is in the origin of the coordinate system. The obtained plot indicated that in the vertical direction the beam was not pointing to the center of the target cell but at least a few millimeters too low. Consequently the beam position was raised for two millimeters to reduce electrons scattering at the target frame. This measure did reduce the amount of electrons scattered at the target frame drastically. During the actual experiment the beam was rastered using a much lower amplitude than during this test.

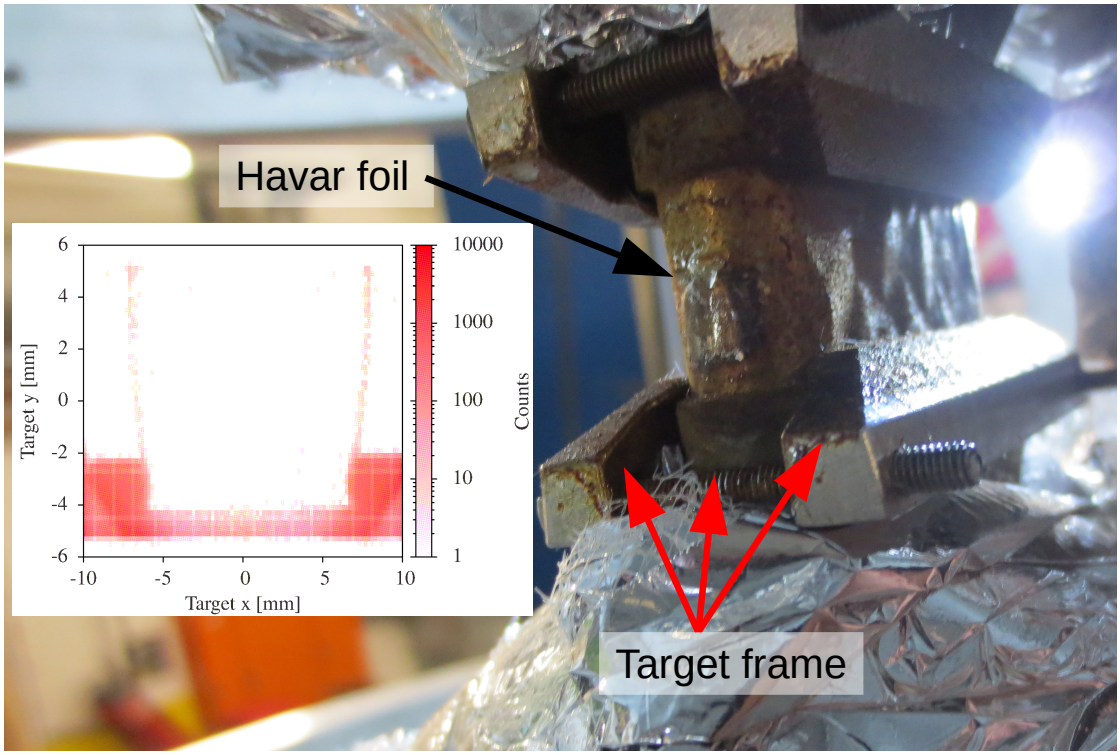

Figure 63: Photo of the target cell including a plot showing the data when the beam was rastered with high amplitudes. The target frame, ranging from $-5\,\text{mm} <$ target y $< 2\,\text{mm}$, is clearly visible in the plot. The havar foils on the sides are also visible in the plot where target y is greater 2 mm.

E

VALUES OF THE FORM FACTOR

The values of the proton electric form factor which were determined in the ISR experiment are listed in Table 6.

Setup	Q^2 $[(GeV/c)^2]$	G_E
ISR_495_01	0.01540	$0.9561 \pm 0.0025 \pm 0.0045$
ISR_495_02	0.01288	$0.9605 \pm 0.0017 \pm 0.0045$
ISR_495_03	0.01105	$0.9694 \pm 0.0018 \pm 0.0045$
ISR_495_04	0.00952	$0.9667 \pm 0.0016 \pm 0.0045$
ISR_495_05	0.00820	$0.9756 \pm 0.0024 \pm 0.0049$
ISR_495_06	0.00709	$0.9748 \pm 0.0020 \pm 0.0065$
ISR_495_07	0.00613	$0.9775 \pm 0.0020 \pm 0.0077$
ISR_330_01	0.00694	$0.9833 \pm 0.0040 \pm 0.0050$
ISR_330_02	0.00597	$0.9733 \pm 0.0030 \pm 0.0048$
ISR_330_03	0.00511	$0.9839 \pm 0.0029 \pm 0.0046$
ISR_330_04	0.00441	$0.9810 \pm 0.0033 \pm 0.0046$
ISR_330_05	0.00379	$0.9904 \pm 0.0031 \pm 0.0046$
ISR_330_06	0.00328	$0.9895 \pm 0.0035 \pm 0.0046$
ISR_330_07	0.00283	$0.9959 \pm 0.0038 \pm 0.0047$
ISR_330_08	0.00245	$0.9987 \pm 0.0030 \pm 0.0050$
ISR_330_09	0.00211	$1.0008 \pm 0.0040 \pm 0.0056$
ISR_330_10	0.00183	$0.9810 \pm 0.0045 \pm 0.0065$
ISR_195_01	0.00257	$0.9986 \pm 0.0047 \pm 0.0058$
ISR_195_02	0.00211	$0.9941 \pm 0.0032 \pm 0.0057$
ISR_195_03	0.00181	$0.9829 \pm 0.0036 \pm 0.0059$
ISR_195_04	0.00156	$0.9948 \pm 0.0033 \pm 0.0065$
ISR_195_05	0.00134	$1.0051 \pm 0.0041 \pm 0.0070$

Table 6: Setup name, central momentum of Spec. B, mean measured Q^2 for all three beam energy settings and determined value of G_E. The given uncertainties are the statistical and the systematic uncertainties respectively.

BIBLIOGRAPHY

[1] Hofstadter, Robert and Robert W. McAllister: *Electron Scattering from the Proton*. Phys. Rev., 98:217–218, Apr. 1955.

[2] Antognini, Aldo et al.: *Proton Structure from the Measurement of 2S-2P Transition Frequencies of Muonic Hydrogen*. Science, 339(6118):417–420, 2013.

[3] Mohr, Peter J., David B. Newell and Barry N. Taylor: *CODATA recommended values of the fundamental physical constants: 2014**. Rev. Mod. Phys., 88:035009, Sep 2016.

[4] Pohl, Randolf, Ronald Gilman, Gerald A. Miller and Krzysztof Pachucki: *Muonic Hydrogen and the Proton Radius Puzzle*. Annual Review of Nuclear and Particle Science, 63(1):175–204, 2013.

[5] Bernauer, J. C., M. O. Distler, J. Friedrich et al.: *The electric and magnetic form factors of the proton*. Phys. Rev. C, 90:015206, Jul. 2014.

[6] Aulenbacher, Stephan: *Design and Simulation of the Internal Gas-Target for MAGIX*. Diploma thesis, Institut für Kernphysik, Johannes Gutenberg-Universität Mainz, 2014.

[7] G., Lerner Rita and Trigg George L.: *ENCYCLOPEDIA OF PHYSICS*. VCH Publishers, Inc., Second edition, 1991. ISBN:3-527-26954-1.

[8] Povh, Bogdan, Klaus Rith, Christoph Scholz, Frank Zetsche and Werner Rodejohann: *Teilchen und Kerne; Eine Einführung in die physikalischen Konzepte*. Springer-Verlag GmbH, Nineth edition, 2014. ISBN: 978-3-642-37821-8.

[9] Frisch, R. and O. Stern: *Über die magnetische Ablenkung von Wasserstoffmolekülen und das magnetische Moment des Protons. I.* Zeitschrift für Physik, 85(1-2):4–16, 1933.

[10] Estermann, I. and O. Stern: *Über die magnetische Ablenkung von Wasserstoffmolekülen und das magnetische Moment des Protons. II*. Zeitschrift für Physik, 85(1-2):17–24, 1933.

[11] Hanneke, D., S. Fogwell and G. Gabrielse: *New Measurement of the Electron Magnetic Moment and the Fine Structure Constant*. Phys. Rev. Lett., 100:120801, Mar. 2008.

[12] Demtröder, Wolfgang: *Experimentalphysik 4, Kern-, Teilchen- und Astrophysik*. Springer-Verlag, fourth edition, 2014. ISBN: 978-3-645-21475-2.

[13] Nishino, H., S. Clark, K. Abe, Y. Hayato et al.: *Search for Proton Decay via* $p \to e^+\pi^0$ *and* $p \to \mu^+\pi^0$ *in a Large Water Cherenkov Detector*. Phys. Rev. Lett., 102:141801, Apr. 2009.

[14] Chambers, E. E. and R. Hofstadter: *Structure of the Proton*. Phys. Rev., 103:1454–1463, Sep. 1956.

[15] Rose, M. E.: *The Charge Distribution in Nuclei and the Scattering of High Energy Electrons*. Phys. Rev., 73:279–284, Feb. 1948.

[16] Halzen, Francis and Alan D. Martin: *QUARKS AND LEPTONS: An Introductory Course in Modern Particle Physics*. John Wiley & Sons, Inc., First edition, 1984. ISBN: 0-471-88741-2.

[17] Griffiths, David: *Introduction to Elementary Particles*. WILEY-VCH Verlag GmbH & Co. KGaA, Second edition, 2008. ISBN: 978-3-527-40601-2.

[18] Greiner, Walter and Joachim Reinhardt: *QUANTUM ELECTRODYNAMICS*. Springer-Verlag Berlin Heidelberg New York, Third edition, 2003. ISBN: 3-540-44029-1.

[19] McAllister, R. W. and R. Hofstadter: *Elastic Scattering of 188-Mev Electrons from the Proton and the Alpha Particle*. Phys. Rev., 102:851–856, May 1956.

[20] Rosenbluth, M. N.: *High Energy Elastic Scattering of Electrons on Protons*. Phys. Rev., 79:615–619, Aug. 1950.

[21] A. Mooser, S. Ulmer, K. Blaum K. Franke H. Kracke C. Leiteritz W. Quint C. C. Rodegheri C. Smorra and J. Walz: *Direct high-precision measurement of the magnetic moment of the proton*. Nature, 509(7502):596–599, May 2014.

[22] Ernst, F. J., R. G. Sachs and K. C. Wali: *Electromagnetic Form Factors of the Nucleon*. Phys. Rev., 119:1105–1114, Aug. 1960.

[23] Vanderhaeghen, Marc and Thomas Walcher: *Long Range Structure of the Nucleon*. Nucl. Phys. News, 21:14–22, 2011.

[24] Carlson, Carl E. and Marc Vanderhaeghen: *Empirical Transverse Charge Densities in the Nucleon and the Nucleon-to-Δ Transition*. Phys. Rev. Lett., 100:032004, Jan. 2008.

[25] Perdrisat, C.F., V. Punjabi and M. Vanderhaeghen: *Nucleon electromagnetic form factors*. Progress in Particle and Nuclear Physics, 59(2):694 – 764, 2007.

[26] Kelly, James J.: *Nucleon charge and magnetization densities from Sachs form factors*. Phys. Rev. C, 66:065203, Dec. 2002.

[27] Bernauer, Jan C.: *Measurement of the elastic electron-proton cross section and separation of the electric and magnetic form factor in the Q^2 range from 0.004 to 1 $(Gev/c)^2$*. PhD thesis, Institut für Kernphysik, Johannes Gutenberg-Universität Mainz, 2010.

[28] Maximon, L. C. and J. A. Tjon: *Radiative corrections to electron-proton scattering*. Phys. Rev. C, 62:054320, Oct. 2000.

[29] Vanderhaeghen, M., J. M. Friedrich, D. Lhuillier, D. Marchand, L. Van Hoorebeke and J. Van de Wiele: *QED radiative corrections to virtual Compton scattering*. Phys. Rev. C, 62:025501, Jul. 2000.

[30] Friedrich, Jan M.: *Messung der Virtuellen Comptonstreuung an MAMI zur Bestimmung Generalisierter Polarisierbarkeiten des Protons*. PhD thesis, Institut für Kernphysik, Johannes Gutenberg-Universität Mainz, 2000.

[31] Tsai, Yung-Su: *Radiative Corrections to Electron-Proton Scattering*. Phys. Rev., 122:1898–1907, Jun. 1961.

[32] McKinley, William A. and Herman Feshbach: *The Coulomb Scattering of Relativistic Electrons by Nuclei*. Phys. Rev., 74:1759–1763, Dec 1948.

[33] McCord, Miles, Hall Crannell, L.W. Fagg, J.T. O'Brien, D.I. Sober, J.W. Lightbody, X.K. Maruyama and P.A. Treado: *Preliminary results of a new determination of the rms charge radius of the proton*. Nuclear Instruments and Methods in Physics Research Section B: Beam Interactions with Materials and Atoms, 56â57, Part 1:496 – 499, 1991.

[34] Simon, G.G., Ch. Schmitt, F. Borkowski and V.H. Walther: *Absolute electron-proton cross sections at low momentum transfer measured with a high pressure gas target system*. Nuclear Physics A, 333(3):381 – 391, 1980.

[35] Bernauer, J. C. et al.: *High-Precision Determination of the Electric and Magnetic Form Factors of the Proton*. Phys. Rev. Lett., 105:242001, Dec. 2010.

[36] Kostoulas, I., A. Entenberg, H. Jöstlein et al.: *Muon-Proton Deep Elastic Scattering*. Phys. Rev. Lett., 32:489–493, Mar. 1974.

[37] R. Gilman, E.J. Downie, G. Ron et al.: *Studying the Proton "Radius" Puzzle with μp Elastic Scattering; The MUon proton Scattering Experiment (MUSE) Collaboration*. http://arxiv.org/pdf/1303.2160v3.pdf, Jul. 2013.

[38] Crawford, C. B., A. Sindile, T. Akdogan, R. Alarcon et al.: *Measurement of the Proton's Electric to Magnetic Form Factor Ratio from* $^1\vec{H}(\vec{e}, e'p)$. Phys. Rev. Lett., 98:052301, Jan. 2007.

[39] Zhan, X., K. Allada, D.S. Armstrong et al.: *High-precision measurement of the proton elastic form factor ratio at low*. Physics Letters B, 705(1–2):59 – 64, 2011.

[40] Chen, Y.-C., A. Afanasev, S. J. Brodsky, C. E. Carlson and M. Vanderhaeghen: *Partonic Calculation of the Two-Photon Exchange Contribution to Elastic Electron-Proton Scattering at Large Momentum Transfer*. Phys. Rev. Lett., 93:122301, Sep. 2004.

[41] Tomalak, O. and M. Vanderhaeghen: *Two-photon exchange correction in elastic unpolarized electron-proton scattering at small momentum transfer*. Phys. Rev. D, 93:013023, Jan 2016.

[42] Melnikov, Kirill and Timo van Ritbergen: *Three-Loop Slope of the Dirac Form Factor and the 1S Lamb Shift in Hydrogen*. Phys. Rev. Lett., 84:1673–1676, Feb. 2000.

[43] Parthey, Christian G., Arthur Matveev, Janis Alnis et al.: *Improved Measurement of the Hydrogen 1S–2S Transition Frequency*. Phys. Rev. Lett., 107:203001, Nov. 2011.

[44] Beauvoir, B. de, F. Nez, L. Julien, B. Cagnac et al.: *Absolute Frequency Measurement of the $2S-8S/D$ Transitions in Hydrogen and Deuterium: New Determination of the Rydberg Constant*. Phys. Rev. Lett., 78:440–443, Jan. 1997.

[45] Bernauer, Jan C. and Randolf Pohl: *The Proton Radius Puzzle*. Scientific American, 310:32–39, 2014.

[46] Pohl, Randolf et al.: *The size of the proton*. Nature, 466(7303):213–216, Jul. 2010.

[47] Patrignani, C. and Particle Data Group: *Review of Particle Physics*. Chinese Physics C, 40(10):100001, 2016.

[48] Olive, K.A. and Particle Data Group: *Review of Particle Physics*. Chinese Physics C, 38(9):090001, 2014.

[49] Aubert, B., R. Barate, D. Boutigny et al.: *J/ψ production via initial state radiation in $e^+e^- \to \mu^+\mu^-\gamma$ at an e^+e^- center-of-mass energy near 10.6 GeV*. Phys. Rev. D, 69:011103, Jan. 2004.

[50] Arbuzov, Andrej B., Eduard A. Kuraev, Nikolay P. Merenkov and Luca Trentadue: *Hadronic cross sections in electron-positron annihilation with tagged photon*. Journal of High Energy Physics, 1998(12):009, 1998.

[51] Mihovilovič, M., H. Merkel, A. Weber et al.: *Initial state radiation experiment at MAMI*. EPJ Web of Conferences, 72(00017), 2014.

[52] Weber, A., M. Mihovilovič and H. Merkel: *Measurement of the proton form factor at very low Q^2*. Proc. Sci, (Bormio2016):001, 2016. To be published.

[53] Schulz, Florian: *Präzisionsmessung der Λ-Separationsenergie von ${}^{4}_{\Lambda}\mathrm{H}$ am Mainzer Mikrotron*. PhD thesis, Institut für Kernphysik, Johannes Gutenberg-Universität Mainz, 2016.

[54] Jankowiak, A.: *The Mainz Microtron MAMI –Past and future*. Eur. Phys. J. A, 28:149–160, 2006.

[55] Kreidel, H.-J., K. Aulenbacher, M. Dehn et al.: *Sustaining the Reliability of the MAMI-C Accelerator*. pages 4023 – 4025, 2012. Proceedings of IPAC2012, New Orleans, Louisiana, USA; ISBN: 978-3-95450-115-1.

[56] Kaiser, K.-H., K. Aulenbacher, O. Chubarov, M. Dehn et al.: *The 1.5 GeV harmonic double-sided microtron at Mainz University*. Nuclear Instruments and Methods in Physics Research Section A: Accelerators, Spectrometers, Detectors and Associated Equipment, 593(3):159 – 170, 2008.

[57] Herminghaus, H., A. Feder, K.H. Kaiser, W. Manz and H.v.d. Schmitt: *The design of a cascaded 800 MeV normal conducting C.W. race track microtron*. Nuclear Instruments and Methods, 138(1):1 – 12, 1976.

[58] Blomqvist, K.I et al.: *The three-spectrometer facility at the Mainz microtron {MAMI}*. Nucl. Instr. and Meth. A, 403(2–3):263 – 301, 1998.

[59] Korn, Manfred: *Entwicklung des Bahnruckverfolgungsverfahrens für die Drei-Spektrometer-Anlage und experimentelle Bestimmung der Abbildungseigenschaften der Spektrometer A und B mit elastischer Elektronenstreuung*. PhD thesis, Institut für Kernphysik, Johannes Gutenberg-Universität Mainz, 1994.

[60] Sauer, Peter: *Entwicklung, Aufbau und Inbetriebnahme der vertikalen Driftkammern der Drei-Spektrometer-Anlage am Mainzer Mikrotron MAMI und Studium der Reaktion* ${}^{12}\mathrm{C}\left(\mathrm{e},\mathrm{e}'\mathrm{p}\right){}^{11}\mathrm{B}$ *für mittlere und hohe Nukleonenimpulse im Kern*. PhD thesis, Institut für Kernphysik, Johannes Gutenberg-Universität Mainz, 1995.

[61] Müller, Ulrich: *Detector discussion*. private communication, 2016.

[62] Böhm, Ralph: *Messung des Wirkungsquerschnitts der Reaktion* $\mathrm{d}\left(\mathrm{e},\mathrm{e}'\mathrm{p}\right)\mathrm{n}$ *für fehlende Impulse bis* 950MeV/c *und Trennung der longitudinalen und transversalen Reaktionsanteile für fehlende Impulse bis* 350MeV/c. PhD thesis, Institut für Kernphysik, Johannes Gutenberg-Universität Mainz, 2001.

[63] Merkel, H. et al.: *Recoil polarization and beam-recoil double polarization measurement of η electroproduction on the proton in the region of the $S_{11}(1530)$ resonance*. Phys. Rev. Lett., 99(13):132301, 2007.

[64] Ewald, Ingo: *Kohärente Elektroproduktion von neutralen Pionen am Deuteron nahe der Schwelle*. PhD thesis, Institut für Kernphysik, Johannes Gutenberg-Universität Mainz, 2000.

[65] Distler, Michael Otto: *pA-meter discussion*. private communication, 2016.

[66] Euteneuer, H. et al.: *Auszug aus dem Jahresbericht 92/93 1.0 Beschleuniger*. Institut für Kernphysik Universität Mainz, Jan. 1994.

[67] Thesing, Tobias: *Magnetfeldsensoren*. Universität Koblenz-Landau, Fachbereich Informatik, Jun. 2009.

[68] Suszcynsky, David M. and Joseph E. Borovsky: *Modified Sternglass theory for the emission of secondary electrons by fast-electron impact*. Phys. Rev. A, 45:6424–6428, May 1992.

[69] Planskoy, B.: *Secondary electron emission from aluminium foils in high energy beam monitors*. Nuclear Instruments and Methods, 24:172 – 180, 1963.

[70] Distler, Michael Otto: *Elektroproduktion von neutralen Pionen am Wasserstoff an der Schwelle*. PhD thesis, Institut für Kernphysik, Johannes Gutenberg-Universität Mainz, 1996.

[71] *NIST, National Institute of Standards and Technology*. http://webbook.nist.gov/chemistry/fluid/, 2013.

[72] Keskinen, Kari I. and Mika M. Aalto: *Parameter collection for saturated and compressed liquid density models based on Hankinson-Thomson model (COSTALD)*. 6th Asian Thermophysical Properties Conference, Oct. 2001.

[73] Lidén, K. and N. Starfelt: *Internal and External Bremsstrahlung Accompanying the Beta Rays of* P^{32}. Phys. Rev., 97:419–427, Jan. 1955.

[74] Press, William, Saul Teukolsky, William Vetterling and Brian Flannery: *Numerical Recipes in C*. Cambridge University Press, Cambridge, UK, 2nd edition, 1992.

[75] *GoodFellow*. http://www.goodfellow.com/catalogue/GFCat4I.php?ewd_token=g3zDoEpnrLMG0NawryhzMBb51lQtLT&n=ODVf5ZCd4c0FWRrrPgUG8Rs3NRpEnj&ewd_urlNo=GFCat4C10&Catite=CO010210&CatSearNum=2, 2015.

[76] Friedrich, J. and N. Voegler: *The salient features of charge density distributions of medium and heavy even-even nuclei determined from a systematic analysis of elastic electron scattering form factors*. Nuclear Physics A, 373(2):192 – 224, 1982.

[77] Dally, E. B., M. G. Croissiaux and B. Schweitz: *Scattering of High-Energy Electrons by Nitrogen-14 and -15*. Phys. Rev. C, 2:2057–2068, Dec. 1970.

[78] Drechsel, D., S.S. Kamalov and L. Tiator: *Unitary isobar model – MAID2007*. The European Physical Journal A, 34(1):69–97, 2007.

[79] Mihovilovič, M. and H. Merkel: *Simulation discussion*. private communication, 2016.

[80] Distler, Michael O., Jan C. Bernauer and Thomas Walcher: *The {RMS} charge radius of the proton and Zemach moments*. Physics Letters B, 696(4):343 – 347, 2011.

[81] Christmann, Mirco: *Konstruktion und Charakterisierung eines GEM-Prototyp-Detektors für MAGIX*. Diploma thesis, Institut für Kernphysik, Johannes Gutenberg-Universität Mainz, 2016.

[82] Leo, William R.: *Techniques for Nuclear and Particle Physics Experiments: A How-to Approach*. Springer-Verlag, second edition, 1994. ISBN: 978-3-540-57280-0.